ABSTRACT

| | |
|---|---|
| Title of Document: | PROCESS INTENSIFICATION BY UTILIZING MULTISTAGE MANIFOLD MICROCHANNEL HEAT AND MASS EXCHANGERS |
| | Ratnesh Tiwari |
| | Doctor of Philosophy, 2015 |
| Directed By: | Professor Michael Ohadi, Department of Mechanical Engineering |

Much of research and development work has been dedicated to implement the heat and mass transfer using microchannel technology; however, it is not yet cost effective and is limited to higher end applications such as electronics cooling and selected applications in automotive and aircraft heat exchangers. The work on mass transfer application of micro channels also has been very limited, despite the very high potential contribution of micro channels for mass transfer enhancement. Scaling up of microchannel equipment presents several manufacturing and process organization challenges such as flow distribution inside microchannels, cost, fouling, high pressure drops etc.

This thesis presents the development of a cost effective and compact tubular manifold microchannel heat and mass exchanger (MMHX) for industrial applications. A novel design for the flow distribution manifolds has been proposed. The proposed manifold helps in the enhancement of heat and mass transfer by creating better flow mixing. The MMHX is designed in such a way that the manifold causes the flow to break into multiple passes of very short flow lengths in the microchannels. These flow lengths are short enough such that the flow in the channels is always into entry zone (developing laminar zone) both hydrodynamically as well as thermally, resulting in higher heat transfer than that in the fully developed laminar flow in conventional microchannel heat exchangers. The pressure drop in the device is low as the fluid flow length into the microchannels is very short.

While the manifold design helps in flow distribution, very short flow length inside the microchannels mitigates the problems of flow instability of two-phase heat transfer applications such as that in evaporators and condensers. The mass transfer in gas liquid reaction applications is enhanced due to the multiple passes where continuous breaking of the gas liquid interface as well as mixing of the bulk liquid occurs.

A multi-pass microchannel heat and mass exchanger prototype was designed, fabricated and was experimentally tested for the performance as liquid-liquid heat exchanger, evaporator, condenser and gas- liquid absorber. Experiments were carried out by changing the liquid and gas flow rates, geometry of the microchannels and the size of the manifold. Flow visualization studies were also performed to study two phase flow distribution and flow pattern in the manifold.

Experimental results have shown that the mass transfer coefficient (using $CO_2$ and DEA-water solution) for the microchannel absorber is 1 to 2 orders of magnitude higher than the conventional absorber. This increase in mass transfer is mainly attributed to high interfacial area to volume ratio of microchannels and good mixing in the manifold. Similarly, heat transfer coefficient for the single phase heat transfer as well as for two phase heat transfer (evaporator and condenser) is about 3 to 8 times higher than the conventional heat exchangers such as shell and tube or plate type heat exchanger. High transfer rates enable us to design compact heat and mass transfer devices for the industrial applications. Industrial processes, such as carbon capture, which are not economically viable due to their high cost, can be feasible with the development of these next generation heat and mass transfer equipment. Due to the simplicity of the component design and the assembly, cost of the industrial scale equipment can be substantially lower as compared other compact heat exchangers.

Current work is the continuation of heat and mass transfer work being carried out at the S2TS lab in University of Maryland. Jha V.(2012) studied the first version of single pass manifold microchannel heat exchanger and Ganapathy H. (2014) studied the absorption of $CO_2$ in DEA solution in single microchannel as well as in parallel microchannels. MMHX studied in this study builds on the previous work by introducing the multipass concept and utilizing commercially available fin tubes as microchannel surfaces.

PROCESS INTENSIFICATION BY UTILIZING MULTISTAGE MANIFOLD

MICROCHANNEL HEAT AND MASS EXCHANGERS


By


Ratnesh Tiwari



Dissertation submitted to the Faculty of the Graduate School of the

University of Maryland, College Park, in partial fulfillment

of the requirements for the degree of

Doctor of Philosophy

2015



Advisory Committee:

Professor Michael Ohadi, Chair

Associate  Professor Ebrahim AlHajri (Co-Advisor and Special Member)

Associate Professor Bao Yang

Assistant Professor Siddhartha Das

Professor Kyu Yong Choi (Dean's Representative Member)

# Dedication

ॐ नमो भगवते वासुदेवाय
जन्माद्यस्य यतोऽन्वयादितरतश्चार्थेष्वभिज्ञः स्वराट्
तेने ब्रह्म हृदा य आदिकवये मुह्यन्ति यत्सूरयः ।
तेजोवारिमृदां यथा विनिमयो यत्र त्रिसर्गोऽमृषा
धाम्ना स्वेन सदा निरस्तकुहकं सत्यं परं धीमहि ॥ १ ॥

O my Lord, Śrī Kṛṣṇa, son of Vasudeva, O all-pervading Personality of Godhead, I offer my respectful obeisances unto You. I meditate upon Lord Śrī Kṛṣṇa because He is the Absolute Truth and the primeval cause of all causes of the creation, sustenance and destruction of the manifested universes. He is directly and indirectly conscious of all manifestations, and He is independent because there is no other cause beyond Him. It is He only who first imparted the Vedic knowledge unto the heart of Brahmājī, the original living being. By Him even the great sages and demigods are placed into illusion, as one is bewildered by the illusory representations of water seen in fire, or land seen on water. Only because of Him do the material universes, temporarily manifested by the reactions of the three modes of nature, appear factual, although they are unreal. I therefore meditate upon Him, Lord Śrī Kṛṣṇa, who is eternally existent in the transcendental abode, which is forever free from the illusory representations of the material world. I meditate upon Him, for He is the Absolute Truth.

# Acknowledgements

I would like to express my sincere gratitude to my advisor Dr. Michael Ohadi for his inspiring guidance, support and patience and providing me an excellent environment for research. I am grateful to Dr. Serguei Dessiatoun who helped me throughout my research as an excellent mentor and a friend. This work would not have been possible without his invaluable inputs and guidance.

I am deeply thankful to my co-advisor and friend Dr. Ebrahim AlHajri for his guidance, help and support during this research. I would like to thank Dr. Amir Shooshtari and Dr. Mohamed AlShehhi for guiding me in my research. I would like to thank my committee members, Dr. Kyu Yong Choi, Bao Yang and Dr. Siddhartha Das for their time and insightful comments.

 I would like to acknowledge Arjun Sharma, Abhishek Singh, Christian Bonk and Bala Natrajan for their assistance in the experimental work. I would also like to thank all my friends at S$^2$TS laboratory, Dr. Edvin Cetegen, Dr. Vibhash Jha, Dr. Harish Ganapathy, Kamal Muthusubramanian, Veena Rao, Raphael Mandal, Rohit Andhere, Stefan Bangerth, Josh Fody, Fabio Battaglia, Martinus Arie and Deniael, for providing a joyful and intellectually stimulating environment. I am also grateful to my friends from IIT Kanpur namely Harikeshwar Kushwaha, Amit Shukla, Pawan Goel and Vipin Agrawal who helped and guided me during this work. I would like to thank H.G. Devaprastha Das and H.G. Padma Malini DD from UMD Bhakti Yoga Club for inspiring me during my stay at UMD.

I express my heartfelt gratitude to my late grandparents, my parents and my siblings Sangita, Mukesh and Neelam for their love, support and innumerable

# Table of Contents

# List of Tables

# List of Figures

# Nomenclature

| | |
|---|---|
| A | Base heat transfer area, $m^2$ |
| C | Concentration, mol/l |
| $C_p$ | Specific heat Capacity, J/K |
| D | Diameter, m |
| f | Friction factor |
| H | Henery's constant |
| h | Enthalpy , heat transfer coefficient, $W/m^2$-K |
| $K_L$ | Liquid side mass transfer coefficient |
| $K_L a$ | Volumetric mass transfer coefficient, $s^{-1}$ |
| L | Length, m |
| LMTD | Log mean temperature difference, °C |
| m | Mass, kg |
| $\dot{m}$ | Mass flow rate, kg/s |
| N | Number of moles |
| Nu | Nusselt Number |
| P | Pressure, Pa |
| Pr | Prandtl Number |
| Q | Cooling capacity, W |
| R | Uncertainty |
| Re | Reynolds number |
| STC | Seider-tate constant |
| T | Temperature at the state point, °C |
| U | Overall heat transfer coefficient, W/m -K |
| W | Work input, W |
| x | Vapor quality |
| $\rho$ | Density |
| $\mu$ | Dynamic Viscosity |

## Subscripts

| | |
|---|---|
| $CO_2$ | Carbon dioxide |
| m | Mean |
| in | inlet |
| out | outlet |
| i | inner |
| o | outer |
| fg | latent |
| h | hydraulic |
| *w* | water |
| *base* | Base of the channel |
| *Sat* | Saturation |
| *Ref* | Refrigerant |

# 1   Introduction

## 1.1   Summary

This chapter will familiarize the reader with the background information about the Process Intensification (PI) and role of the microchannel/micro-fluidic devices in PI. The background of the microchannel heat and mass exchangers has also been described in brief. Scope as well as contribution of the current work has been outlined.

## 1.2   Process intensification

While on one hand the electronics industry seen rapid advancement in past few decades and has been following Moore's law of doubling the circuit density every two years since late 1950s (Moore, 1965), chemical and process industry has not seen significant changes in past several decades. Sizes of the heat exchangers, reactors, columns etc remain more or less same as they were about 100 years ago.

With the current advances in Computation Fluid Dynamics, Microfluidics, Nanotechnology and manufacturing technology a transformative change is being promised under a term called 'process intensification'.
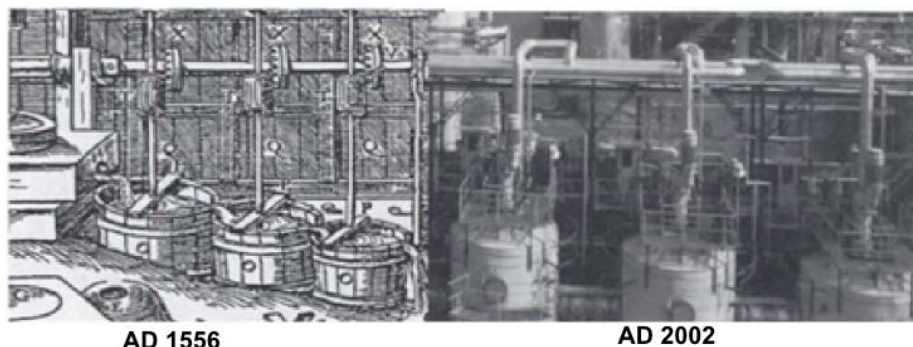


**Figure 1-1:** Similarity between the gold processing plant of AD1556 and AD 2002. (Stankiewicz & Moulijn, 2003)

### 1.2.1 Definition

PI has been defined in various ways by several researchers (Stankiewicz & Moulijn, 2000; Hüther *et al.*, 2005; Charpentier, 2007; Keil, 2007; Reay *et al.*, 2013) however all these definitions center around the following concept:*"Any chemical engineering development that leads to a substantially smaller, cleaner, safer and more energy efficient technology is process intensification"(Reay et al., 2013).*It should be noted that the aim of process intensification is not to achieve few percentages of improvement but to bring the drastic improvements in terms of space, time, energy, cost, materials and environment. *"PI is not a strategy for the faint hearted"*(Ramshaw, 2001) and thus the approach to PI has to be novel and mostly unusual to achieve such demanding improvements. An example of reported process intensification was demonstrated to achieve 99.9% reduction in reaction time, 99% reduction in inventory and reduced the impurity level to 93% by using spinning disc reactors (Oxley *et al.*, 2000).

Process intensification technologies can be categorized mainly by two ways: 1) Novel hardware (implementation of novel hardware such as compact heat exchangers, micro heat exchanger reactors (HEX), micro-reactors, rotating reactor) and 2) Novel methodologies (or implementation of novel process methods such as multifunctional reactors, hybrid separators etc).

### 1.2.2 Advantages of PI:

Process intensification provides multifold benefits. Some of them are listed below:

- *Cost:* Use of the compact equipment leads to size reduction of associated structure and piping. This reduces the land cost, installation cost (civil, piping,

instrumentation etc) as well as the direct cost of the equipment. PI techniques also seek to reduce the inventory and amount of the chemicals use in the equipment.

- *Safety:* Lower inventory of hazardous materials reduces the risk from spillage and leaks. As per the saying " What you don't have cant leak" (Kletz *et al.*, 1991), smaller systems have very low charge and can improve the safety significantly. PI can also be used to simplify the operations to avoid the safety hazards and/or to moderate the hazardous conditions.

- *Energy efficiency:* Microfluidic devices such as heat and mass exchangers can deliver very high heat and mass transfer coefficient, which in turn reduce the driving force of the exchange (such as temperature and concentration difference). This makes them the ideal candidate for the high energy efficient process from thermodynamic point of view.

- *Clean environment:* Tighter waste disposal regulations can be imposed by lowering the cost of waste treatment plants. Also, the new technologies with PI will seek to apply the cleaner processes reducing the impact on the environment. One of the examples for such technologies is Carbon Capture. Post combustion carbon capture and storage enabled by PI technologies can significantly reduce the greenhouse gas emission from the power plants.

- *Time to market:* Due to the compact size of the units and assistance from rapid prototyping, time to market the PI technologies are much lower as compared to the traditional technologies which took several years to go from the lab experiments to the pilot plants and then to full scale plants.
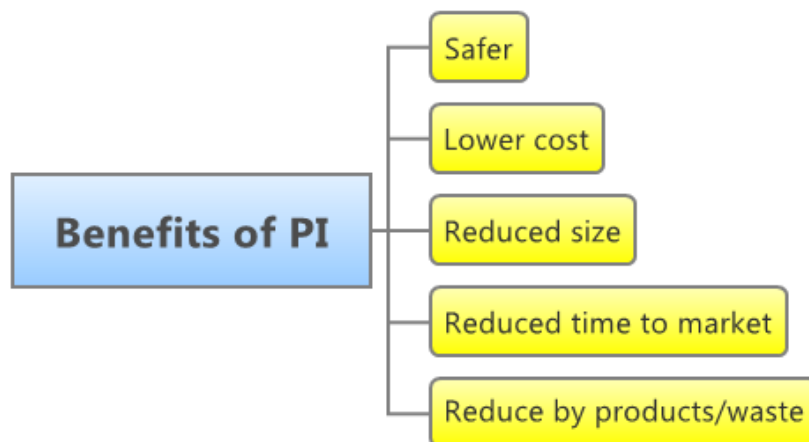
**Figure 1-2:** Benefits of process intensification

## 1.3 Microchannels Heat and Mass Exchangers

Compact heat exchangers and the reactors are one of the most important hardware part of the process intensification. Typical compact heat exchangers use microchannel technology to enhance the surface to volume ratio to improve their heat transfer (Reay *et al.*, 2013). High interfacial area to volume ratio also increases the gas-liquid mass transfer. The gas-liquid interfacial area in such devices is also very high as compared to the typical industrial columns. The combined heat and mass transfer improvement can make the reaction rates 10 to 500 times than the conventional reactors (Brophy, 2005). Similarly, the mass transfer coefficient can also be 1 to 3 orders of magnitude higher.

Substantial amount of research and development in this area has been reported in literature in the past couple of decades. As of now, several micro-reactors have been developed and some are already in the phase of commercialization (Johnston & Haynes, 2002; Freemantle & LONDON, 2004; Freemantle & London, 2004; Mazanec *et al.*, 2008)
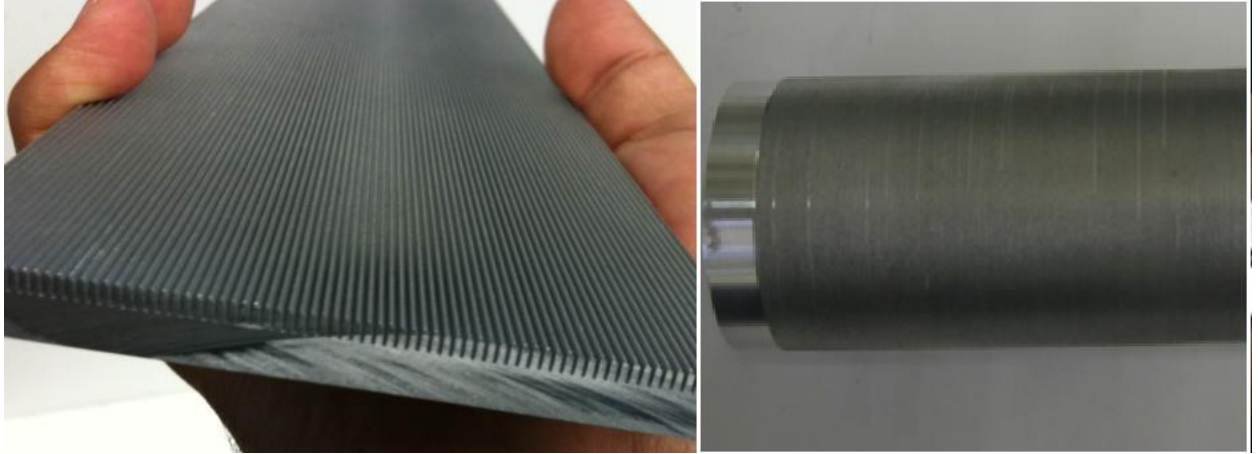
**Figure 1-3:** (a) Microchannels (fin width=300µm, fin height =500µm) on the flat Aluminum surface. (b) Microchannals on aluminum tube (fin width=80µm, height =350µm)

Although the microchannel technology looks fascinating, it has its own challenges in the industrial scale commercialization. Some of those are listed below:

1. Fouling of the channels

2. Limitation of the heat and mass transfer in the parallel microchannels due to the laminar nature of the flow

3. Higher pressure drop in the channels

4. Lower throughput of the flow

5. Issues related to the flow distribution into the channels (especially for two phase flow)

6. Flow instability during two phase flows

7. Expensive manufacturing of the microchannels and

8. Expensive assembly methods such as diffusion bonding etc.

Current work aims to address majority of the issues related to microchannel reactors/heat exchangers by proposing a design which uses low cost manufacturing.

The design provides better flow mixing, distribution as well as higher heat transfer coeffcients as compared to the conventional parallel microchannel reactor/HX. The design facilitates the flow distribution; enhances the heat transfer and helps reduce the pressure drop. The manifold is designed in such a way that the flow length in the microchannel per pass is kept very short. Short channel length for single phase heat transfer makes sure that the flow is in developing laminar zone both hydrodynamically as well as thermally, resulting in higher Nusselt numbers. While shorter flow length mitigates the problems of flow instability in two-phase heat transfer, especially designed manifold helps achieving the good two phase flow distribution.

## 1.4 Scope of thesis

The thesis focuses on the design and development of the high performance and cost effective microchannel reactor which uses fin tubes as microchannel surface and 3-D printed manifold for flow distribution. The flow visualization for a two phase flow has been presented. Experiments on the $CO_2$ –DEA absorber, single phase as well as two phase heat exchangers are presented.

- Development of the finned tube microchannel reactor
- Two phase flow visualization
- Experiments single phase heat exchanger
- Experiments evaporator and condenser
- Experiments with the absorber using $CO_2$-DEA fluid pair

## 1.5    Roadmap for the thesis

Thesis has been divided into 9 chapters. After the introduction of the subject, second chapter describes the relevant literature review. Geometry and the working principle of the reactor and heat exchanger is discussed in chapter 3 while  chapter 4 presents the flow visualization results for the two phase flow in the absorber. The pressure drop in single and two phase flows are also presented for various cases.

Chapter 5 focuses on the experimental study of single phase heat transfer in the device using water as the working fluid in both sides. Chapters 6 and 7 describe two phase heat transfer during the evaporation and condensation processes, respectively, using R134a as the refrigerant and water as the heat transfer fluid in both cases. $CO_2$-DEA absorption experimental results are presented in chapter 8. Chapter 9 presents the conclusions and the future work.

# 2 Literature review and background

Background theory and the literature review related to the heat and mass transfer in manifold microchannel heat exchangers has been discussed in the current chapter. Process intensification and manifold microchannel heat exchanger concept is discussed at the beginning of the chapter. Apart from the relevant literature review for the gas-liquid absorption, single phase and two phase heat transfer in microchannels, fundamental theory related to the heat transfer in short microchannels is also discussed.

## 2.1 Microchannel heat exchangers

Microchannel heat sink was proposed by (Tuckerman & Pease, 1981) for the first time for cooling of integrated circuits using water as coolant.
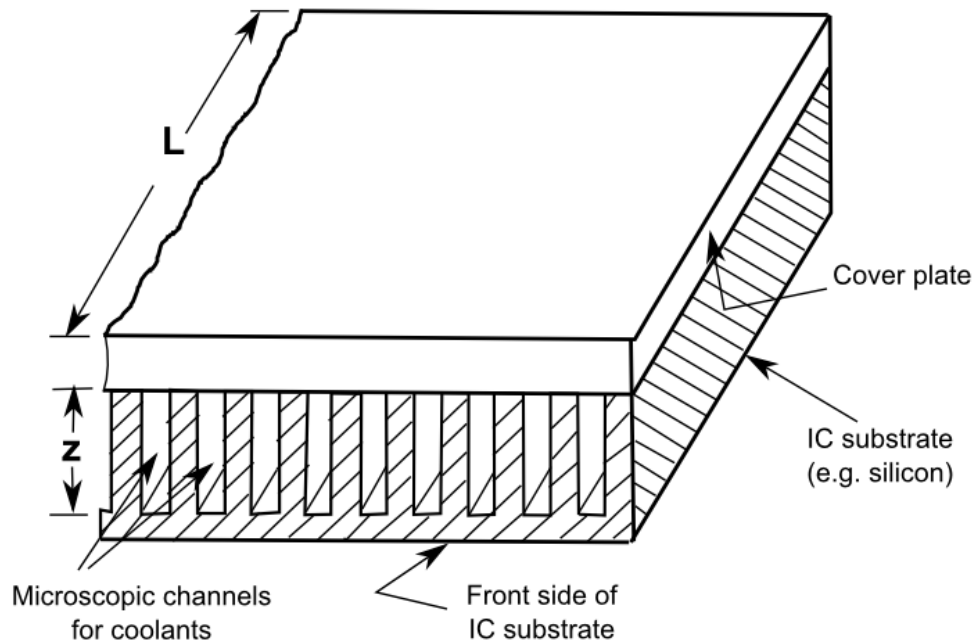


**Figure 2-1:** Schematic view of microchannel heat exchanger proposed by Tuckerman and Pease, 1981

The device was made of parallel microchannels and was capable of high heat flux cooling. However, such parallel microchannel heat exchangers have several shortcomings as discussed below:

1) *High pressure drop:* The conventional parallel microchannels have very high pressure drops which can easily go up to the order of two bars for small electronic cooling heat sinks (Copeland *et al.*, 1997).

2) *Temperature variation across the device:* Since the parallel microchannel heat exchangers can handle only low flows, there is a large temperature difference the heat exchanger between its inlet and outlet. This causes inhomogeneous heat removal from the electronics surface.

3) To increase the capacity of heat removal and to reduce the pressure drop, two phase boiling heat transfer can be used instead of single phase. However, parallel microchannel heat sinks are not very much suitable for the two phase boiling due to the severe instabilities encountered during the two phase boiling (Kandlikar *et al.*, 2005).

4) Flow maldistribution is another challenge for the microchannel heat exchangers. The maldistribution is more severe for two phase applications such as evaporator, condensers and gas-liquid reactors.

## 2.2   Manifold microchannel heat exchanger (MMHX)

Manifold microchannel heat exchanger design (MMHX) design concept is utilized to avoid the shortcomings of the parallel microchannel heat exchangers. MMHX design concept is shown in the Figure 2-2. MMHX is designed in such a way that the fluid is guided into the microchannels with the help of manifold which acts as

flow distributor. Although the length of MMHX may be large, the inlet fluid into the MMHX flows in axial direction mainly in the manifold and passes through the microchannels only for a very short distance before coming out. This helps in significant reduction in pressure drop inside the heat exchanger.
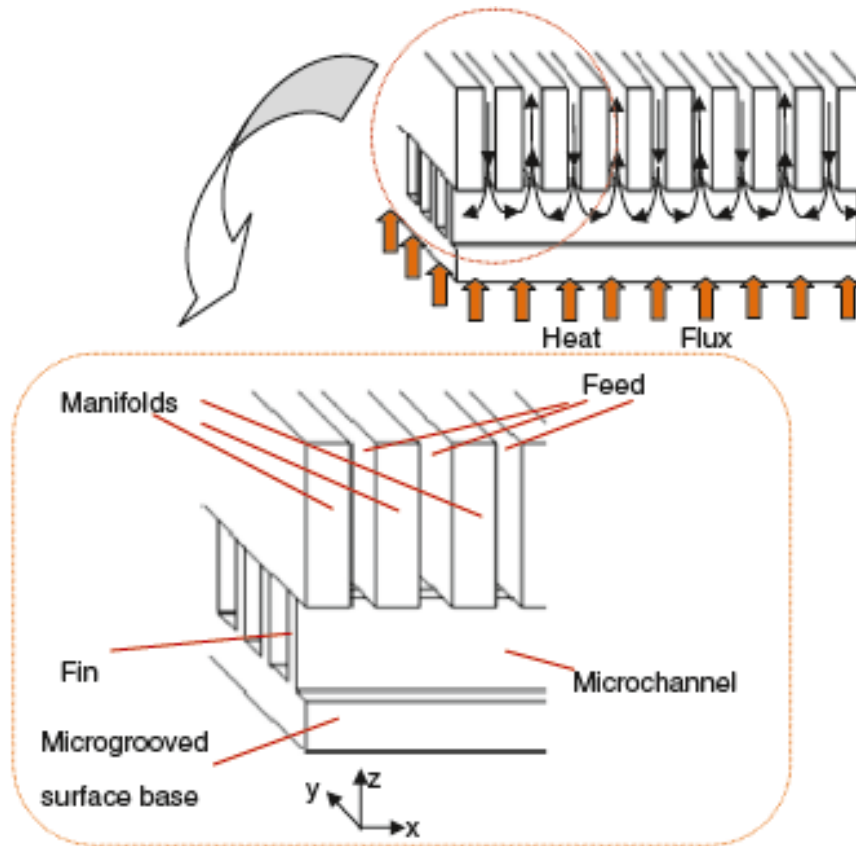


**Figure** 2-2**:** Schematic of the forced fed manifold microchannel working concept (Ohadi *et al.*, 2013)

### 2.2.1 Unique features of manifold microchannel device

The key points that make the MMHX device unique are the following:

- *High heat transfer coefficient:* Flow in the MMHX is hydrodynamically and thermally developing. This results in higher heat transfer as compared to that in fully developed flow in conventional long microchannels. Heat transfer is

further enhanced in multipass microchannel heat exchangers due to the mixing of fluid inside the manifold as discussed in the later sections in this chapter.

- *Lower pressure drop:* Any flow stream travelling into the MMHX flows through microchannel for a very short length, resulting in low pressure drop in the device.

- *Flow distribution:* Manifold microchannel heat exchangers show good flow distribution for single phase (Arie *et al.*, 2015) as well as for two phase applications (Edvin, 2010).

- *Flow instability:* Carefully designed manifold microchannel heat exchangers do not face problems of two phase flow instability as encountered in the conventional microchannels (Ohadi *et al.*, 2013).

- *Handling of varying vapor quality across the exchanger:* Manifold can be designed in such a way that the stage length of the manifold is variable across the length of the device. Variable manifold stage length can be used to optimize the heat transfer and pressure drop for applications such as evaporator, condensers and gas liquid absorbers which encounter varying vapor quality along the device.

- *Low cost:* Tubular design of the MMHX uses the mass produced fin tubes as microchannels. It's simple geometry and easy assembly makes it cost effective.

### 2.2.2 Literature review MMHX

Forced fed concept was first studied by (Copeland, 1995; Copeland *et al.*, 1995; Copeland *et al.*, 1997) in late 90s. Both the numerical and experimental study

of single phase heat transfer was performed using microchannel width of 57 and 1136 µm and fluorocarbon as working fluid. Similar experiments with MMHX using air as working fluid showed 35% improvement in heat transfer as compared to the conventional microchannels heat exchangers (Kim *et al.*, 1998). Detailed single phase and two phase heat transfer work has been carried out at S$^2$TS lab at the University of Maryland (Cetegen *et al.*, 2007; Baummer *et al.*, 2008; Cetegen, 2008; Kermani *et al.*, 2009; Jha *et al.*, 2011; Boyea *et al.*, 2013). Heat dissipation up to 1 kW/cm$^2$ was achieved in the manifold heat sink with using R245a refrigerant in evaporation mode (Baummer *et al.*, 2008). The experiments carried out with high heat flux evaporators by (Cetegen *et al.*, 2007) showed that the manifold microchannel heat sinks did not have flow instability problems. These studies also confirm that MMHX provides very high heat transfer for low pumping power as compared to the single phase heat transfer.

### 2.2.3 Heat transfer and pressure drop in manifold microchannels

Cetegen, 2010, compared pumping power requirement for two different circular tubes one with length L with single inlet and outlet while the other configuration was made by dividing the same tube into 'n' different sections of L/n length as shown in the Figure 2-3. Each of these small tube sections had separate inlet and outlet. Simple comparison of pumping power for same inlet temperature and heat transfer and overall heat transfer coefficient was done. Split tube configuration had pumping power equal to 1/n$^2$ times of the single large tube. It was concluded therefore that by using small channel lengths, pumping power can be reduced significantly. Heat transfer enhancement in the developing region was neglected in

this analysis. This assumption does not hold true if the length L/n is considerably small. If the flow in the tube is in the developing zone, heat transfer as well as pressure drops are higher. For hydrodynamically developing circular tubes, the following correlation is proposed by Shah and London, 1978:
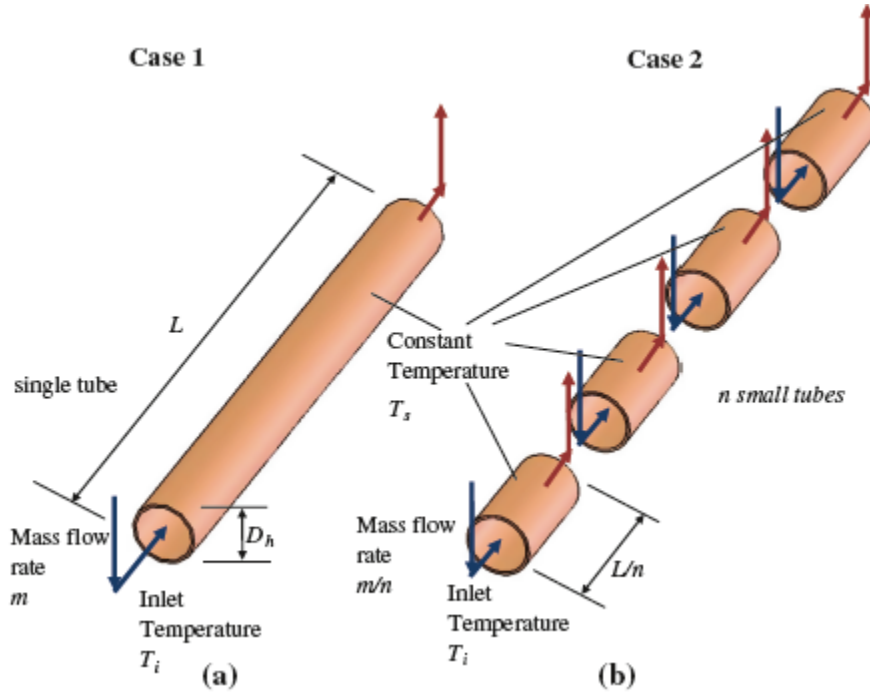


**Figure 2-3:** Schematic of flow in a single long channel and b multiple short channels (Edvin, 2010)

$$f_{app}Re = 344(x^+)^{-0.5} + \frac{\frac{1.25}{x^+} + (fRe)_{fd} - 344(x^+)^{-0.5}}{1 + 2.12 \times 10^{-4}(x^+)^{-0.2}} \quad (1)$$

Where $f_{app}$ is aaparent friction factor, subscript 'fd' represent fully developed flow and $x^+$ is non dimension channel length defined as $x+= L/Re.D$ and

$$(fRe)_{fd} = 64 \quad (2)$$

Hydrodynamic entry length is defined as

$$\left(\frac{L_{fd,h}}{D}\right)_{lam} \approx 0.05 \, Re \quad (3)$$

Thermal entry length is proposed by Kays and Crawford, 1980 as following:

$$\left(\frac{L_{fd,t}}{D}\right)_{lam} \approx 0.05 Re\ Pr \tag{4}$$

Simultaneous developing average Nusselt number Nu for laminar flow in a circular

tube is given by Seider Tate, 1936

$$\overline{Nu} = 1.86 \left(\frac{Re\ Pr}{L/D}\right)^{1/3} \left(\frac{\mu}{\mu_s}\right)^{0.14} \tag{5}$$

Figure 2-4 shows that the Nusselt number in the entry length can be considerably

higher depending upon the entry length for a given flow rate.
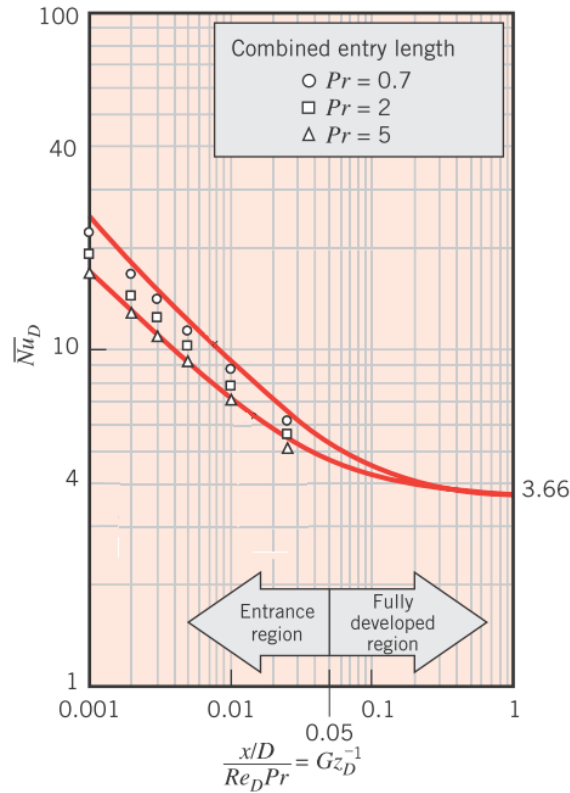
**Figure 2-4:** Average Nusselt number for the entry length (developing flow) solutions for laminar flow in a circular pipe (Incropera, 2011)

## 2.3 Mixing of flow

Several passive techniques for the heat transfer enhancement have been

developed (Webb & Kim, 1994). In order to enhance the heat transfer, it is imperative

to promote the mixing of the boundary layer with the bulk fluid. Several studies have been carried out to design various non-continuous microchannels (Xu *et al.*, 2005; Cheng, 2007; Yan *et al.*, 2007; Xu *et al.*, 2008a, b; Xia *et al.*, 2011; Chai *et al.*, 2013)

(Chai *et al.*, 2013) studied the microchannel heat sink with the thermally redeveloping boundary layer by breaking the boundary layer after short distances. The longitudinal and transverse microchannels were used to achieve this design which showed improved performance in terms of the heat transfer as compared to the conventional microchannel heat sink. (Chai *et al.*, 2013) did optimization study of such microchannel heat sink with the interruption presented in the form of ribs. The rib length, width, its distance from the parallel microchannels and the distance between the two microchambers has been used as variables to study their effect on the heat transfer and pressure drop. It was found that with the introduction of proper mixing introduced by the ribs, heat transfer improvement was up to 1.63 times higher as compared to the conventional microchannel.

Thermal boundary layer disruption and the mixing of the fluid are two main important factors affecting the heat transfer(Chai *et al.*, 2013). In some of the microchannel devices, the thermal boundary layer breaking is achieved; however, the mixing part is often missed. Thus even if we get lots of penalty on the pressure drop, heat transfer does not seem to improve in the similar proportion.

Manifold microchannel heat exchanger promotes the mixing of the boundary layer periodically. A repeated formation and destruction of boundary layer enhances

the heat transfer significantly as compared to the conventional microchannels where it is difficult to break the boundary layer due to the laminar flow in the channels.
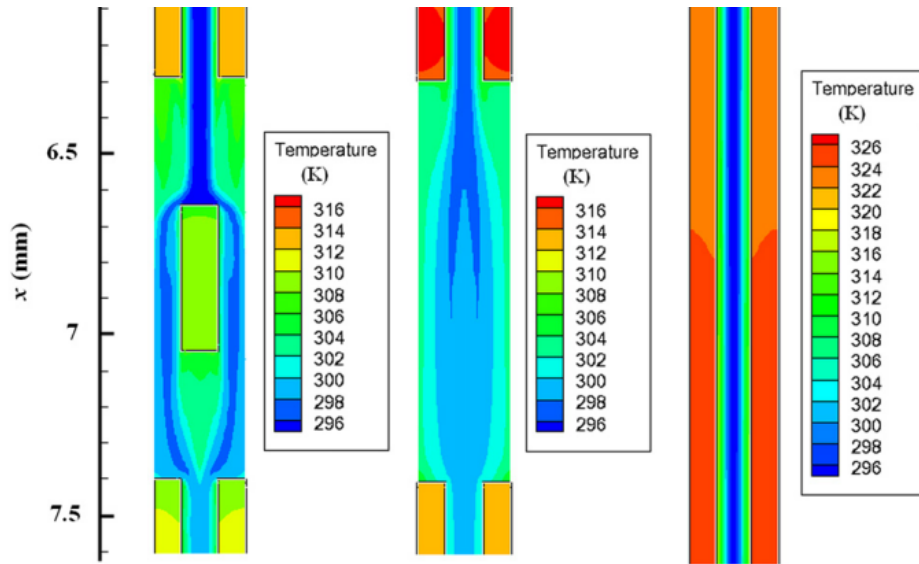


**Figure 2-5:** Temperature field in the plane of z-0.25 mm at Re - 442.65

## 2.4   Boiling

Due to the high interest in electronics cooling and refrigeration systems, flow boiling heat transfer inside the mini and microchannels has been investigated by several authors (Cetegen *et al.*; Kandlikar, 1990; Zhao *et al.*, 2000; Kandlikar, 2002b, a; Warrier *et al.*, 2002; Kandlikar & Steinke, 2003; Kandlikar, 2003; Qu & Mudawar, 2003; Yen *et al.*, 2003; Steinke & Kandlikar, 2004; Agostini *et al.*, 2008; Bertsch *et al.*, 2008; Grzybowski & Mosdorf, 2014). Although microchannel heat sinks promise high heat transfer coefficients with lower pumping power, flow instability during the flow boiling was a major hindrance for achieving higher cooling.

### 2.4.1   Flow boiling instability in microchannels

Typically there are two types of inlet conditions in the microchannel devices resulting in two different flow behaviors. Hard inlet conditions are those which are

equipped with the devices such throttle valve or orifice in the upstream of the channel. Soft inlet conditions are those where the inlet and outlet of the microchannels are common. Although the soft inlet conditions are more common for lab scale devices, later arrangement is more common for parallel microchannel devices used in the electronic cooling applications. Soft inlets are susceptible to the changing pressure drop in the device and hence the variation of inlet flows.

Parallel microchannels with soft inlet conditions show two types of flow instabilities: Severe pressure drop instability or upstream compressible flow instability or periodic instability, which is more disruptive (Qu & Mudawar, 2002; Wu & Cheng, 2003; Qu & Mudawar, 2004; Wu & Cheng, 2004; Koşar *et al.*, 2006). Instability results in the pressure oscillation in a periodic fashion which results in the oscillation of the flow rate. When the liquid flowing in the channel starts boiling, the bubble creates extra resistance to the flow. Thus the flow is reduced in the channel. This reduced flow causes the reduction in pressure drop which further leads to the higher flow in the channel. The instability increases with the heat flux. A second less severe instability is called the parallel channel instability which is marked by the flow fluctuation from channel-to-channel (Qu & Mudawar, 2002, 2004).

Several researchers have worked to mitigate the flow instability in the microchannels using different techniques such as inlet restrictors (Koşar *et al.*, 2006), reentrant cavities (Kuo & Peles, 2008), or diverging cross section design (Lu & Pan, 2008). These schemes, however, were either complex for fabrication (such as cavities inside the microchannels) or result in higher pressure drops (due to inlet restrictions).

### 2.4.2    Flow pattern and boiling heat transfer in microchannels

Boiling heat transfer mechanism in microchannels has been subject of debate among the researchers due to the contradictory observations during the experiments. However there has been agreement that the basic mechanism of the flow boiling in the microchannels is similar to that of the larger channels as long as the microchannel surface has defects smaller than the channel hydraulic diameter (Kendall *et al.*, 2001; Zhang *et al.*, 2005). Bubbles nucleate from the crevices and are released into the stream. However, since the channel size is small, the confinement of the bubbles affects the flow dynamics (Kandlikar, 2002b). Confined bubble flow pattern looks more like a plug flow which changes to annular-slug flow further downstream. The typical flow regime in a microchannel passage is shown in the Figure 2-6.

Boiling mechanism in the microchannels can be one of the following four types: Nucleate boiling, confined bubble boiling, convective boiling and partial dryout (Kew & Cornwell, 1997). Typical experiments for the mini-channels ($D_h$~3mm) have shown that parametric dependency of the flow boiling can be deduces from the larger channels.
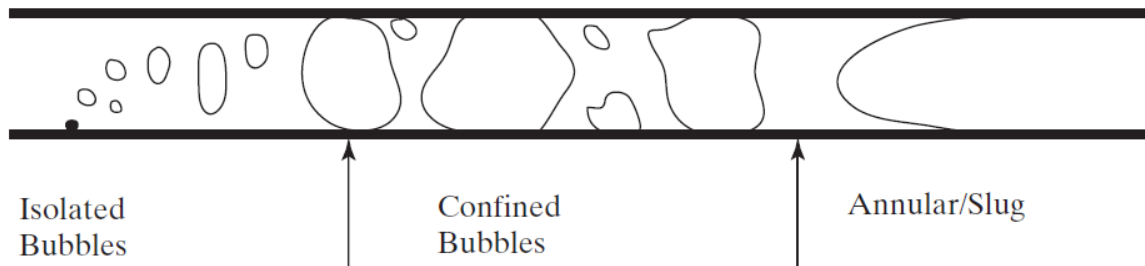


**Figure 2-6:** The major flow boiling regimes in small passages according to Cornwell and Kew (1992)

In the partial boiling zone the heat transfer coefficient (HTC) increases with the mass flux (G) but is independent of G and vapor quality in the fully developed bubble flow region. HTC, however, increases rapidly with the increase in wall heat flux.

Contrary to this observation, experimental data on microchannels ($D_h$ 0.5mm and 1.0 mm with R113 refrigerant) has shown that the HTC increases with G and quality (Lee & Lee, 2001). Predominant mechanism of heat transfer in such channels is force convective evaporation in annular-dispersed flow regime.

Analysis of (Kandlikar, 2003) using 0.2 mm hydraulic diameter channels and water as refrigerant showed that with the increasing vapor quality and/or increasing heat flux, the thin film covering the vapor core starts evaporating, creating a periodic dryout condition which occurs at every passing of the vapor slug. This reduces the HTC significantly and with the further increase of heat flux, it eventually leads to critical heat flux (CHF) condition. It was argued that channel size has considerable effect on the flow regime due to dominant intermolecular forces which changes with the fluid properties.

For moderate to high heat flux boiling in the microchannels, however, an abrupt change to annular flow at the zero equilibrium quality has been observed and convective heat transfer mode is dominating as opposed to the nucleate boiling mode at low heat flux conditions (Qu & Mudawar, 2003). HTC has been reported to be decreasing with the increasing vapor quality.

### 2.4.3 MMHX

Flow boiling mechanism in the MMHX is expected to be similar to that in conventional microchannels, however, due to their short flow length, MMHX do not

have severe problems of flow instability. Similar to single phase heat transfer MMHX has several advantages over traditional TMHX in two phase boiling applications. High pressure drop in long microchannel results in a pressure profile across the device and hence the varying saturation temperature (Ohadi *et al.*, 2013). Pressure drop and hence the temperature difference across the device is much lower in MMHX. (Cetegen, 2010) conducted experiment on two phase boiling using microchannel surfaces 48µm high, 84 µm wide and a gap of 42 µm. They used R245fa as refrigerant and varied mass flux from 200 to 1400 kg/m$^2$. Their experimental result is shown in Figure 2-7. It was found that the HTC based on the wet channel base area was maximum at quality of 0.15. There was a steep increase in HTC as the quality increased for values less than 0.15. Beyond this quality, HTC starts to decrease. This decrease for higher vapor quality was attributed to the dry out zone in the microchannel.

(Ohadi *et al.*, 2013) compared the performance of MMHX with other cooling technologies proposed by (Koşar *et al.*, 2006; Agostini *et al.*, 2008; Visaria & Mudawar, 2008; Sung & Mudawar, 2009)as shown in the Figure 2-7. It can be seen that the two phase MMHX can deliver high heat transfer with minimal pumping power per kW of heat removal.

Heat transfer in MMHX for industrial applications was studied by Jha, 2012. Figure 2-9 shows a 5kW tubular evaporator which uses a high fin density fin tube as enhanced surfaces. Outer of the fin tube had fin density of 200 fin/inch.  As high as 22000 W/m$^2$-K overall heat transfer coefficient was reported using R134a. The weight of heat exchanger was lower than the conventional HX due to the use of all

Aluminum materials however the volume of the HX was significant. This was due the fact that the much of the volume of the HX was void and was not utilized.

## 2.5 Condensation in microchannels

### 2.5.1 Condensation

#### *2.5.1.1 Two phase flow regimes and Heat transfer*

Heat transfer industry is moving towards the compact heat exchangers. Microchannel condensers have been used in automotive industry for the air-conditioning application for several years now, even before the emergence of the fundamental phase change understanding in this scale of the channels. The rectangular microchannels with hydraulic diameters ranging between 0.4 -0.7 mm have been used in these condensers (Kandlikar *et al.*, 2005). Several researchers have been working to understand the heat transfer during the condensation in microchannels (Webb & Ermis, 2001; Zhang *et al.*, 2001; Coleman & Garimella, 2003; Garimella, 2004; Chen & Cheng, 2005; Bandhauer *et al.*, 2006; Agarwal *et al.*, 2010; Chen *et al.*, 2014).  (Garimella & Wicht, 1995) demonstrated that the size of the condenser can be significantly reduced with the use of microchannels as compared to the conventional air-cooled condensers. This reduction was possible due to higher airside heat transfer coefficient, higher surface to volume ratio and higher condensation heat transfer coefficients.
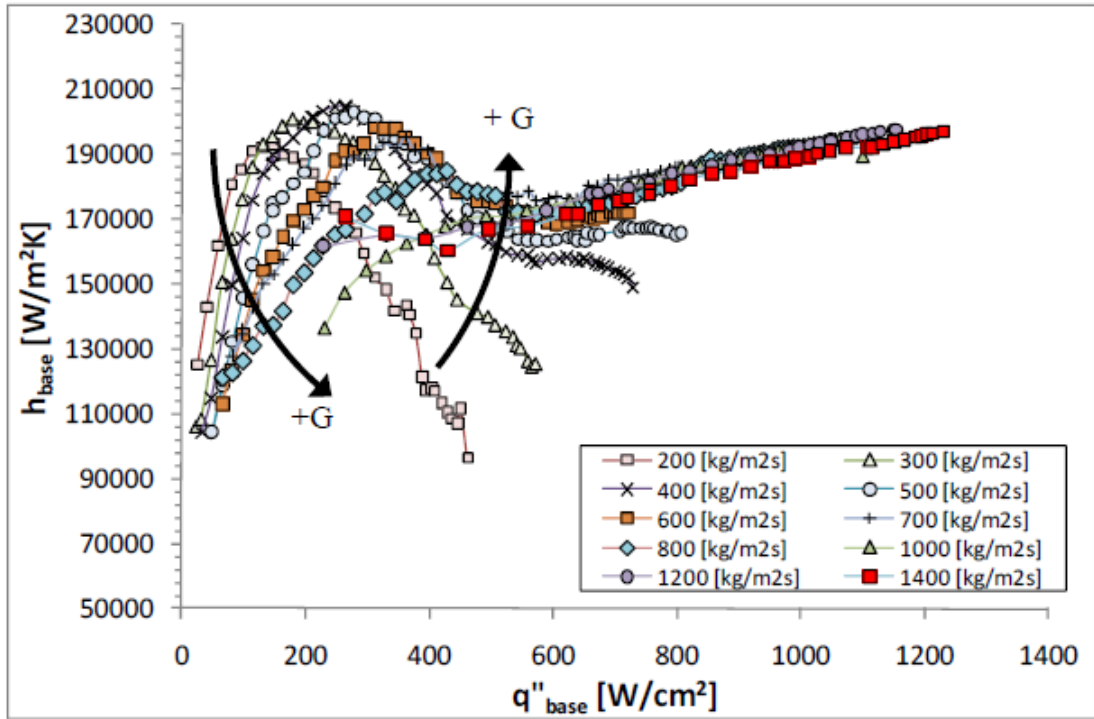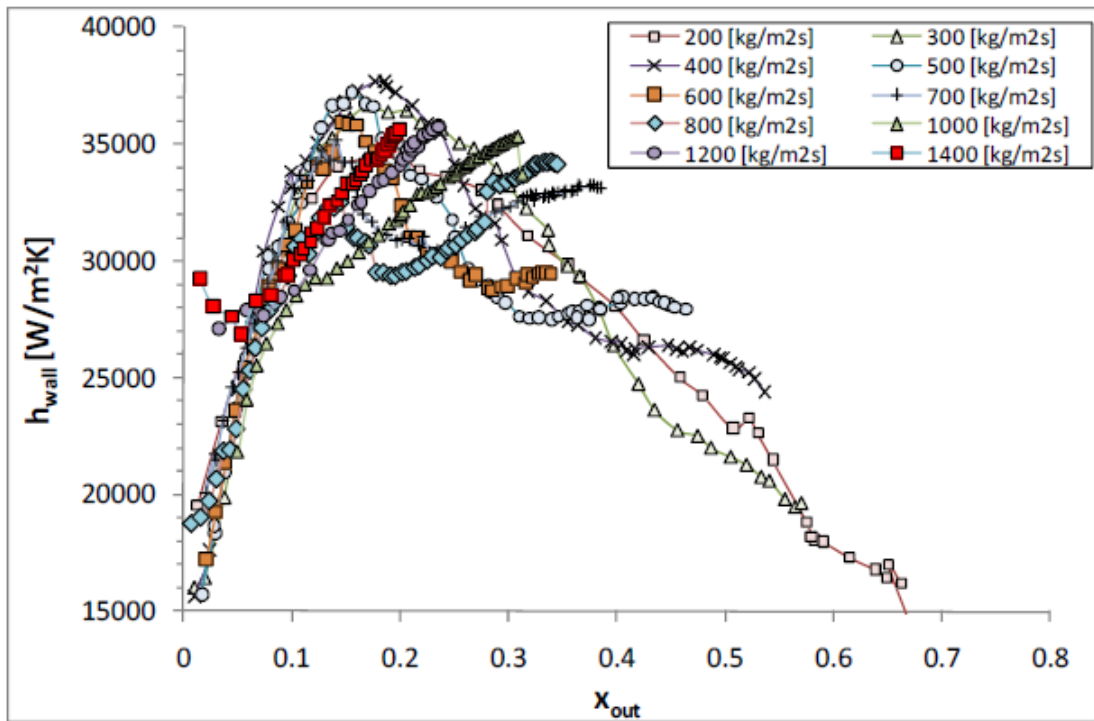
**Figure 2-7:** (a) Heat transfer coefficient based on base area versus base heat flux and (b) heat transfer coefficient based in wetted area versus outlet quantity for FFMHS Surface
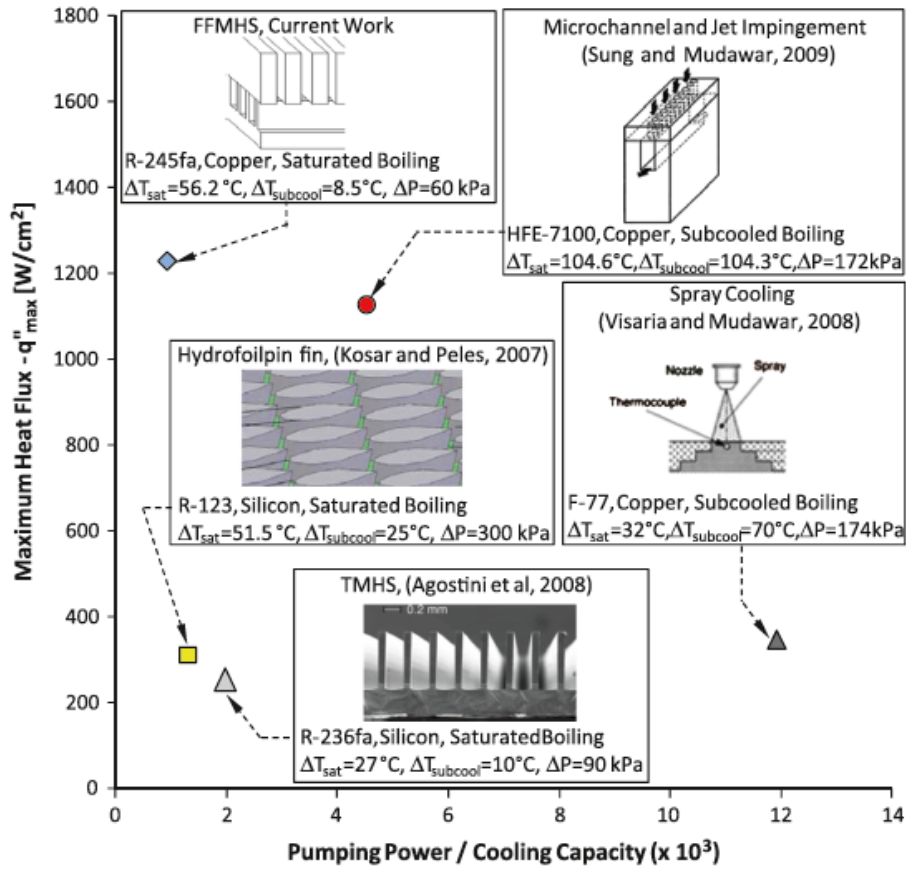
**Figure 2-8:** Thermal performance comparison of different high heat flux cooling technologies (Edvin, 2010)
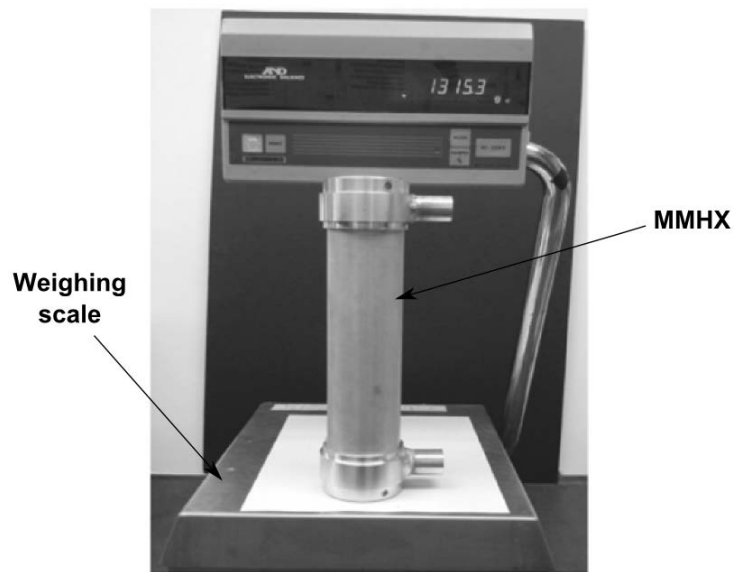


**Figure 2-9:** MMHX developed by Jha V. (2012)

### 2.5.1.2 Heat transfer

Experimental results with the condensation heat transfer in microchannels have typically shown the trends of increasing HTC with increasing mass flux and the vapor quality (Yang & Webb, 1996a, b; Yan & Lin, 1999; William Wang *et al.*, 2002; Baird *et al.*, 2003). In many cases the correlations for conventional channels such as those of (Akars W. W., 1959; Shah, 1979) more of less predicted the experimental data within reasonable accuracy.

### 2.5.1.3 Pressure drop

Two phase pressure drop for condensation of smaller channels has been investigated by many researchers (Yan & Lin, 1999; Garimella, 2004; Garimella *et al.*, 2005; Agarwal & Garimella, 2009; Sakamatapan & Wongwises, 2014). It has been agreed by some investigators that two phase pressure drop in smaller channels is well predicted by the conventional two-phase pressure drop methods at low pressure conditions(Zhang & Webb, 2001; Zhang *et al.*, 2001; Baird *et al.*, 2003; Cavallini *et al.*, 2005).

### 2.5.2 Previous work on microchannel condensation for refrigeration applications

- (Vardan & Dunn, 1997) studied the heat transfer and pressure drop in circular and non-circulate microchannel geometries for Reynolds numbers varying from 3000 to 17000 in liquid phase. (Coleman & Garimella, 2003) studied the flow pattern during the condensation of R134a for six different microchannels. The flow pattern was not strongly dependent on the microchannel shape or the aspect ratio for same hydraulic diameter channels.

- (Yang & Webb, 1996a; Kim *et al.*, 2003) investigated the condensation of R12 in the rectangular extruded aluminum microchannel with fins and without fins. (Kim *et al.*, 2003) performed a similar study but used refrigerants R410 and R22 and compared the results with the existing heat transfer correlations. It was found that the two refrigerants behaved differently in smooth and finned channels. This was attributed to difference in Weber number of the two refrigerants. (Yang & Webb, 1996b) also studied the friction pressure drop for single phase and two phase for the microchannels of 2.64 and 1.56 mm with and without fins. The single phase pressure drop for plain microchannel and finned microchannel was 14% and 36% higher, respectively. They noticed a steep change in the heat transfer as well as pressure drop at higher vapor quality and lower mass fluxes. This was attributed to the surface tension drainage as well as vapor shear.



(a) micro fin tube $D_h$=1.56mm

(b) smooth tube $D_h$=1.41mm
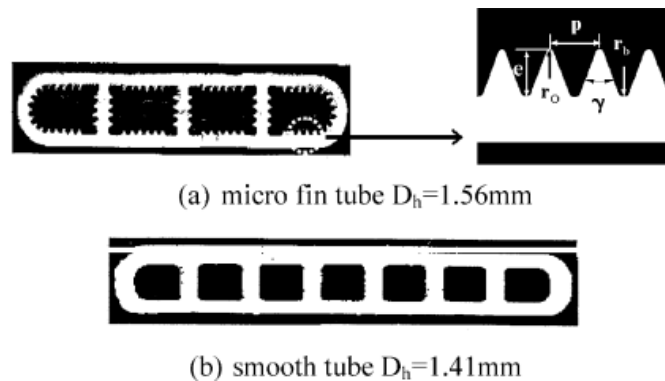
**Figure 2-10:** Enhanced extruded Aluminum microchannels (Kim *et al.*, 2003)

- (Webb & Ermis, 2001) studied the condensation of the R134a refrigerant in the extruded aluminum microchannels of hydraulic diameters varying from 0.4mm to 1.56mm. Condensation heat transfer coefficient as well as the pressure drop increased with the decreasing diameter of the channels. Flow

visualization of the microchannels of hydraulic diameters with 1 to 5 mm was carried out by (Garimella, 2004). (Garimella *et al.*, 2005) studied the pressure drop in the circular microchannels of the similar diameters for a range of flow rates and vapor quality for R134a refrigerant (Figure 2-11).

- (Agarwal *et al.*, 2010) measured the heat transfer coefficient of six different microchannel shapes during the condensation of the refrigerant R134a. Various flow regime models were used to predict the data and mist flow based model was found to be the best fit. Investigation of a new refrigerant R1234ze was performed in extruded aluminum microchannel and was compared with R134a and R236fa  by (Park *et al.*, 2011). (Park *et al.*, 2011; Mohseni *et al.*, 2013) studied the effect of tube inclination on the condensation heat transfer. Their experimental study coupled with visualization showed that there was significant difference in the heat transfer in different inclinations of the tube, especially at lower mass fluxes and lower vapor qualities.

### 2.5.3    Manifold microchannel condensers

Although the heat transfer performance of the microchannel condensers are promising due to their high heat transfer area, issues related to the conventional microchannels such as high pressure drop, maldistribution etc. remain to be resolved. MMHX can help in resolving these issues for the similar reasons as discussed previously.
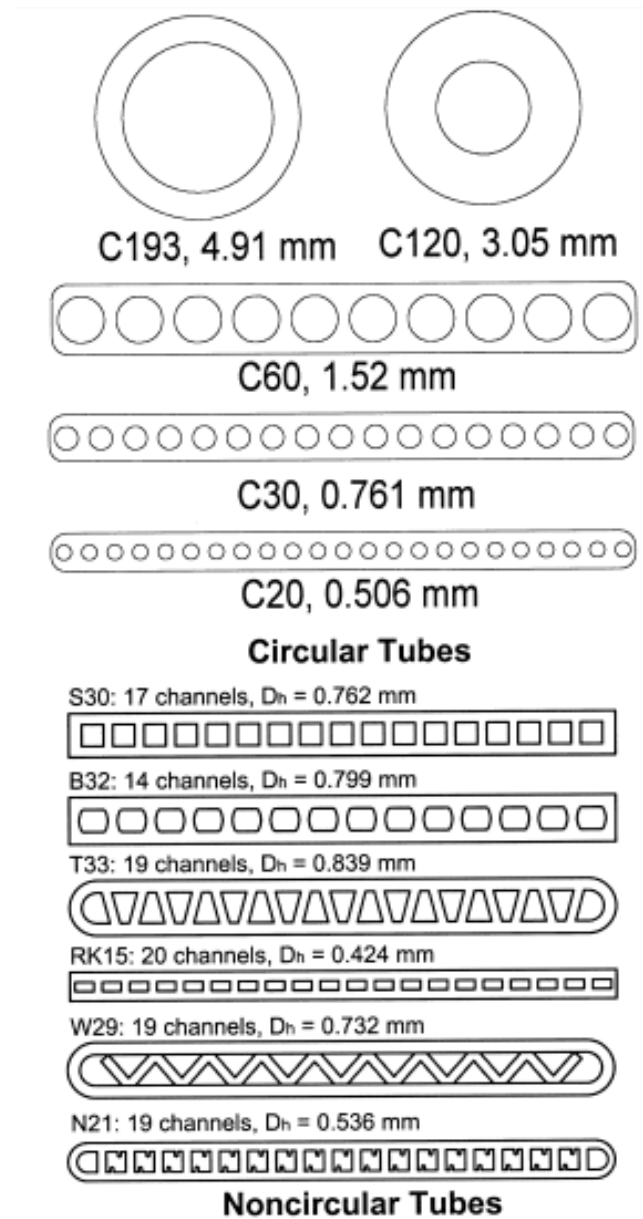
**Figure 2-11:** (Garimella, 2004; Garimella *et al.*, 2005)

(Boyea, 2013) used MMHX geometry for condensation using R134a as refrigerant. He used the similar fin tube geometry as used by (Jha *et al.*, 2011) having fin density of 200 f/inch. The results showed base heat transfer coefficient as high as 90,000 W/m$^2$-K. However, his MMHX was a single pass device and was bulky due to unutilized volume in the heat exchanger.
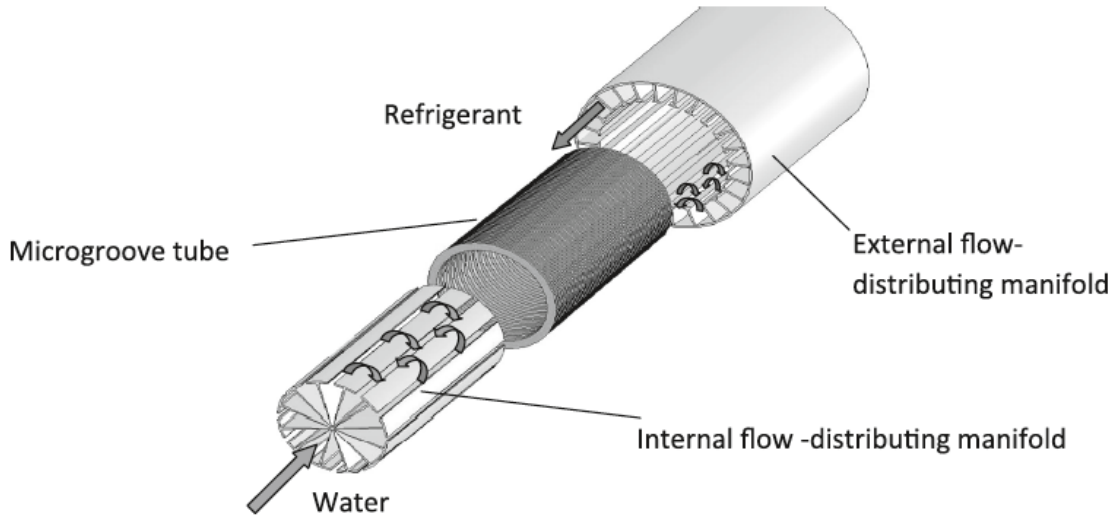
**Figure 2-12:** Schematic diagram of the tubular condenser (Boyea *et al.*, 2013)

## 2.6 Two-phase mass transfer-CO₂-DEA

$CO_2$ absorption process has several industrial applications such as coal gasification, oil refining, hydrogen synthesis, syn-gas production and gas sweetening. One of the another major emerging candidate for the $CO_2$ absorption is carbon capture and carbon sequestration from the power plants which have high amount of $CO_2$ in their exhaust. Due to their high interfacial area to volume ratio, microchannel reactors can achieve very high mass transfer and thus are ideal for such applications. Typical interfacial area in packed towers is about 10 to 350 and spray towers is about 10-100 $m^2/m^3$ (Sanchez *et al.*, 2007) whereas interfacial area in the microchannel reactors ranges between 1000 to 40000 $m^2/m^3$.

Gas-liquid absorption in microchannels has been studied extensively by (Yue *et al.*, 2007; Keshavarz *et al.*, 2008; Constantinou & Gavriilidis, 2009; Lin *et al.*, 2009; Niu *et al.*, 2009; Shao *et al.*, 2010; Cheng & Tan, 2011; Constantinou *et al.*, 2012; Tan *et al.*, 2012; Ganapathy *et al.*, 2013; Tan *et al.*, 2013; Ye *et al.*, 2013; Pan *et al.*, 2014).

Mass transfer as high as $21s^{-1}$ and interfacial area to volume ratio of 9000 $m^2/m^3$ has been achieved experimentally (Yue *et al.*, 2008). These enhancements are two to three orders of magnitude higher than conventional reactors. Only limited work has been published on multichannel or higher throughput absorption devices (Zanfir *et al.*, 2005; Constantinou & Gavriilidis, 2009; Yue *et al.*, 2010; Chen *et al.*, 2011; Gao *et al.*, 2011; Constantinou *et al.*, 2012; Kundu *et al.*, 2012; ganapathy, 2014). The parallel microchannel designs suggested so far are not cost effective due to higher cost of microchannel fabrication as well as expensive processes such as diffusion bonding. Thus a low cost microchannel absorber is very much necessary for the technology to be implemented in the industrial systems.

Multipass MMHX geometry can be utilized for the micro-reactors with the modifications, since the flow length and pressure drop is low per pass, flow distribution problem can be minimized in such geometries while taking the advantage of high interfacial area to volume ratios of microchannels. A multipass MMHX design can also be helpful for the reactors such as $CO_2$ absorbers since the mixing process can be enhanced in the multipass configuration as shall be discussed in later chapters.

## 2.7 Current work

It is clear from the literature review that single phase and two phase heat transfer as well as gas liquid reactions can greatly benefit from the MMHX. MMHX concept has been mainly studies in context of high heat flux cooling applications. The design of the MMHX studied so far is mainly single pass. Current work proposes a multipass MMHX design for industrial applications. A novel multipass manifold

design is proposed to be used in MMHX especially for two phase applications. Proposed MMHX uses low cost fin tube microchannels to keep the cost of the device low.  Heat transfer, and mass transfer was studied in this multipass MMHX for single phase, two phase boiling and condensation and gas liquid absorption processes. The visualization study was conducted to observe the flow pattern in the device for various flows and the manifold designs.

# 3 Design and Working principles of Manifold Microchannel Heat Exchanger

This chapter describes the design and the working principle of Manifold Microchannel Heat Exchanger (MMHX) developed in this study. Working principle of both single and two phase processes are discussed. Assembly and the fabrication processes are discussed in detail.

## 3.1 Introduction

Due to their small channel sizes, fluid flow inside the microchannels is mostly laminar. Parallel microchannel heat exchangers and reactors are being commercialized by the companies such as Velocys, Heatric, etc. Flow regime in microchannel geometries is typically laminar due to the small hydraulic diameter. Convective heat transfer in a fully developed laminar flow regime is low with a constant Nusselt number. This is due to the fact that the convective mixing process in the laminar flow regime is slow as compared to vigorous mixing in a turbulent flow regime. Thus the heat transfer in conventional parallel microchannels is limited by convection. Various techniques such as increasing the surface roughness, use of microchannel geometries such as wavy fins, wired mesh, metallic foams as shown in the Figure 3-1 or other geometries using printed circuit heat exchangers (PCHEs) are suggested to improve the heat transfer. These methods however, result in higher pressure drop and some in lower flow throughput.
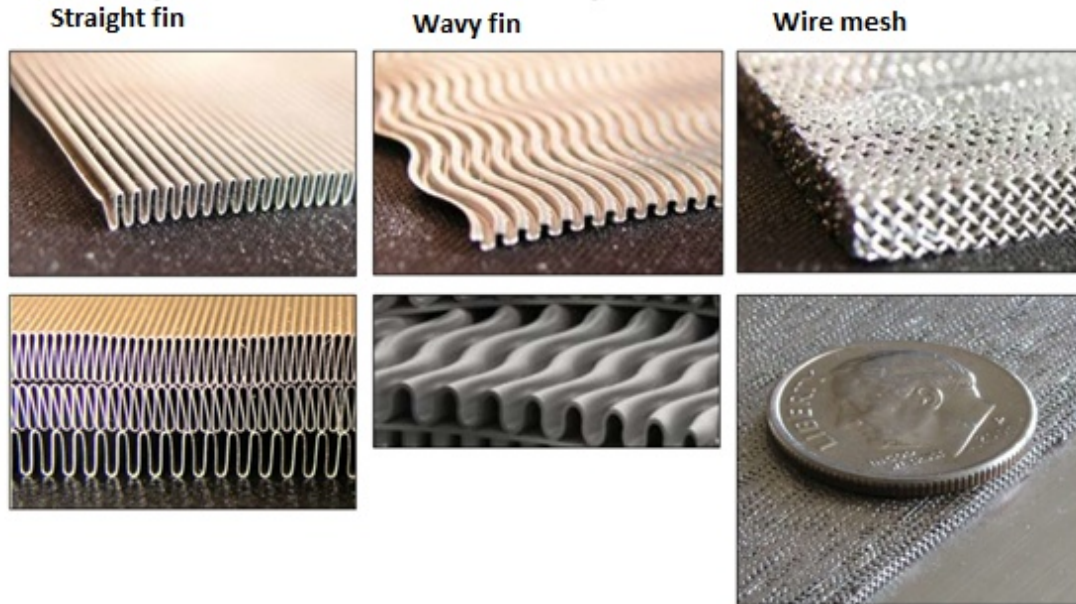
**Figure 3-1:** Various area enhancement methods and geometries

One of the ways to improve the heat transfer in the small hydraulic diameter channels is to operate the heat exchanger in the entrance (developing) region. As shown in Figure 2-4, the average Nusselt number in the entrance region can be much higher than that in fully developed flow. Keeping this in mind, one of the design objectives of the heat exchanger developed in this work was to create multi-pass flow with very short flow length of the microchannels in each pass so that the flow in the device remains in the entrance region throughout the device and higher Nusselt numbers are achieved. Apart from achieving higher heat transfer in the entrance region, design incorporates a mixing zone after each pass. This helps further mixing of the fluid coming out of each microchannel pass.

Figure 3-2 shows a simple concept schematic of the MMHX device. The device is designed in such a way that it contains several passes of microchannels. Each pass contains a number of parallel microchannels and in between each pass a mixing zone is created. The fluid passes through one pass of parallel microchannels

and enters into the mixing zone. From the mixing zone, it then enters into the second pass and second mixing zone and so on.
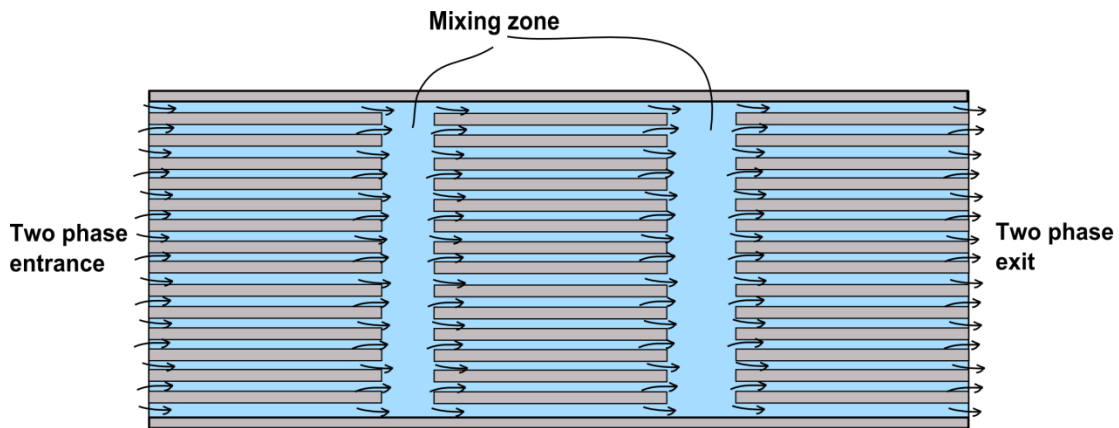


**Figure 3-2:** Concept schematic of multipass HX

## 3.2 Fin tube Microchannel Geometry

As discussed in the previous chapter, the MMHX uses fin tubes as the microchannel geometry. The finned microchannel tube is selected for the following reasons:

- *Low cost:* Technologies used to fabricate microchannel geometries such as photo-chemical etching, laser cutting are expensive. However, making finned tube microchannels is well established technology. This results in lower cost of the microchannels.

- *Easy assembly*: Typical microchannel heat exchangers require extensive brazing or the diffusion bonding which is expensive. Also, the clogging of the channels during the brazing is quite common. MMHX uses manifolds which are slip fit and assembly is more like a shell and tube heat exchanger geometry. It does not require extensive brazing or bolting. Thus the assembly of the heat and mass exchanger becomes easier in case of tubular geometry.

### 3.2.1   Fabrication of the finned tubes

The circular fins (microchannels) on the tubes are made in a way very similar to the thread forming on a metal rod. Several methods are available to create the fined
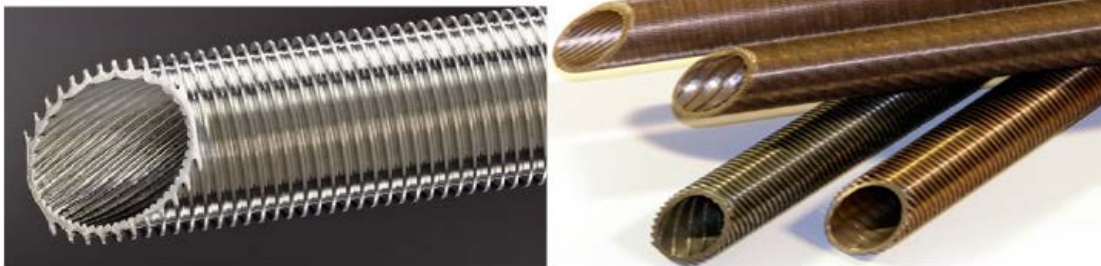


**Figure 3-3:** Fin tubes commercially available in the market (High performance Tube Inc)

geometries (Cunningham & Campbell, 1977; Zohler, 1993; Rieger, 1997b, a, 1999). As shown in the Figure 3-4 a roller is used to make channels on the outer surface. The inner surface of the fin tube has ribs as shown in the Figure 3-3. These ribs are helical in shape and have higher pitch than the fins at the outer side of the tube. Since it is difficult to cut microchannels in the interior of the tube, the helical geometry (rifling) is preferred.  The typical flow on shell side of a shell and tube heat exchanger is cross flow to the tubes. This prevents the dead zone formation inside the fins. However, the flow inside the tube is in axial direction. Hence the rib geometry with higher helical angle is preferred as it helps in the heat transfer enhancement.

### 3.2.1   Fin Tube selection

#### *3.2.1.1   Tube material*

Aluminum and copper were used as tube materials for MMHX. The aluminum material used was copper free Aluminum grade 6061. The material selection was based on the thermal conductivity as well as the chemical compatibility of the material with the working fluids. Intended fluids for the MMHX experiments

34

included water, R134a refrigerant, $CO_2$-DEA mixture and Ammonia water solution. Aluminum has high thermal conductivity as well and works well with the above fluids. The copper tube was used only for the single phase heat transfer experiments
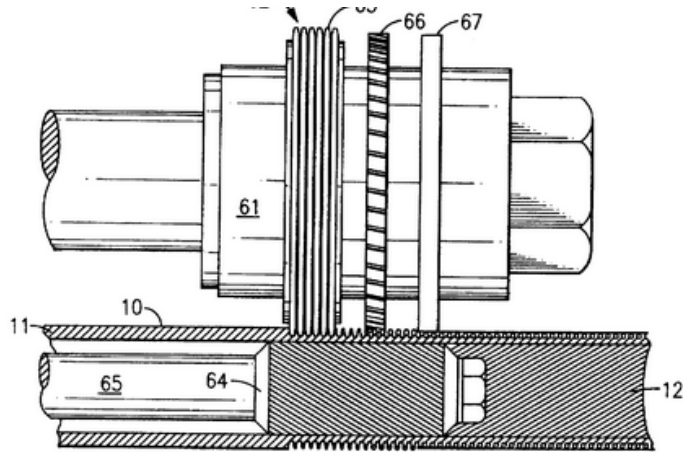


**Figure 3-4:** Example fabrication method of the commercial fin tubes (Rieger, 1997b) with water as working fluid as it is not compatible with the DEA as well as Ammonia solution. As shows in the Table 3-1, the copper tube was a low fin density tube which was used only for the heat transfer comparison purposes and was readily available in the market.

### 3.2.1.2   Tube size

Figure 3-5 shows the typical dimensions of fin tube geometry. The tube used in the MMHX was ¾″ nominal diameter which is common industrial size for the heat transfer application. With the given flow rate for the experiments, the velocity of 2-2.5 m/s was achieved for this size tubes on the tube side. Three different tubes were used in the heat and mass transfer experiments with the dimensional details given in Table 3-1.

| | | |
|---|---|---|
| D | = | Outside Diameter of Plain End |
| $d_i$ | = | Inside Diameter of Plain End |
| $d_r$ | = | Root Diameter |
| $d_o$ | = | Diameter Over Fins |
| $d_i$ | = | Inside Diameter of Fin Section |
| W | = | Wall Thickness of Plain End |
| $W_f$ | = | Wall Thickness Under Fin |
| $F_h$ | = | Height of Fin |
| $F_m$ | = | Mean Fin Thickness |
| P | = | Mean Rib Pitch |
| $R_h$ | = | Height of Rib |
| $H_a$ | = | Helix Angle |
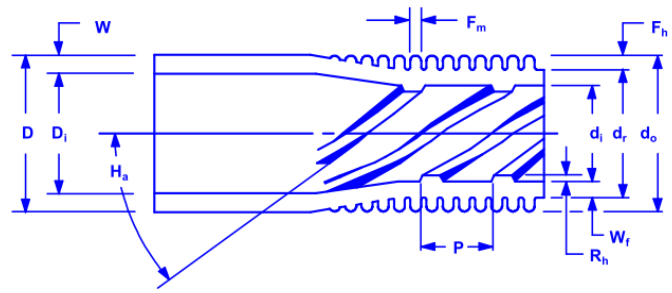
**Figure 3-5:** Feature details of the fin tube (Tube)

**Table 3-1:** Details of the fin tubes used in the current work

| Tube | Material | Fin per inch | Finished fin OD | Nominal root diameter | Tube ID | Ridge height | Outside area enhancement | Inside area enhancement |
|---|---|---|---|---|---|---|---|---|
| | | | (mm) | (mm) | (mm) | (mm) | $(m^2/m^2)$ | $(m^2/m^2)$ |
| A | Al | 60 | 18.8 | 17.63 | 16.21 | 0.483 | 2.95 | 1.64 |
| B | Al | 43 | 18.8 | 17.63 | 15.85 | 0.406 | -* | 1.54 |
| C | Cu | 19 | 18.92 | 15.88 | 14.83 | - | - | - |

* The area enhancement was unclear due to the crosscut of the fins

### 3.2.2 Fin size selection

Fin size of the tubes was selected based on the commercially available technology for microchannel fabrication. Table 3-2 shows the fin geometries of three different tubes used in this study. Similar fin geometry was used by Andhare R. (2013) with the satisfactory heat transfer results. It is also important to note that for the MMHX the fin efficiency plays an important role. For the high thermal conductivity materials such as Aluminum and Copper, the fin efficiencies are typically higher. However, for low thermal conductivity materials the efficiency may decrease rapidly with the increase in fin height and decrease with the fin thickness.

36

**Table 3-2:** Fin geometry of the fin tubes

| Tube type | Fin | | | channel size |
|---|---|---|---|---|
| | pitch | Height | Width | mm |
| | mm | Mm | mm | |
| Plain fin (tube A) | 0.417 | 0.92 | 0.085 | 0.3384 |
| Enhanced fin (tube B) | 0.595 | -* | -* | -* |

* The dimension could not be measured due to the partial crosscut of the fins

## 3.3  Manifold design

Manifold in MMHX is designed to achieve the following functions:

### 3.3.1  Flow distribution

Manifold creates multi-pass flow in MMHX. It distributes the fluid into the microchannels in such a way that the fluid enters into one pass of microchannels and comes into the mixing zone before moving to the next pass. Thus the fluid in the device is forced to move into the microchannels which are oriented radially on the tube. Design of the manifold also helps the fluid to distribute in each microchannel automatically as will be clear in the flow visualization chapter (chapter 4).

### 3.3.2  Throughput control

Size of the manifold enables to change the throughput of the flow into the device. The throughput in a typical microchannel device without manifold with similar microchannel surface area is constant and typically low. With the design of the right manifold, throughput of the MMHX can be varied for a particular fin tube. A part of the fluid can be bypassed from entering the microchannels which ensures the low pressure drop.

### 3.3.3    Pressure drop control

MMHX manifold can be designed to achieve different pass length of the flow into the microchannel as well as varying number of microchannels in each pass. Since the flow length in the microchannel is very short, the pressure drop in the MMHX is lower than the conventional parallel microchannel geometry. This pressure drop can be further reduced by increasing the stage length of the manifold and thus reducing the mass flux into the microchannels at a given mass flow rate. Variable stage length manifolds can also be used to reduce the pressure drop for the applications where the vapor quality changed with the length of the device. E.g. the quality in an evaporator increases with the evaporator length, with the zero quality at the inlet and almost 100% quality at the outlet. This variation of the quality causes higher pressure drops in the heat exchangers with constant flow area tubes due to the changing vapor quality. Variable stage length manifold addresses this issue by distributing the flow in the MMHX microchannels in proportion to the vapor quality. The number of microchannels per pass can be adjusted to minimize the pressure drop in the reactor while maximizing heat/mass transfer.

### 3.3.4    Manifold geometry

As shown in the Figure 3-6, manifold has a tubular geometry with its inner most diameter equal to that of the microchannel tube's finished outer diameter and manifold's outer diameter equal to the inner diameter of the outer shell. Manifold is designed in two geometries: straight ribs and diamond shape ribs. The rib geometry in the manifold is to guide the flow into the microchannels and to create a mixing and axial flow zone in the manifold itself. There are several slots in the axial direction in

the manifold which serve two purposes: 1) to provide inlet into the microchannels, and 2) to act at the outlet for the fluid coming out of the manifold. Depending upon the selection of the microchannel pass length of the device, number of the slot cuts in the manifold may vary. It should be noted that number of inlet ports into the manifold are half of the number of slots. Total number of slots used in all the manifolds in this studyis12.



**Figure 3-6:** A) Diamond rib manifold. B) Rectangular rib manifold

**Table 3-3:** Manifolds geometries used in this study

| Manifold | Mixing plenum shape | Stage length (inch) | Manifold length (inch) | Applications |
|---|---|---|---|---|
| A | diamond | 1.2 | 26.5 | single phase, evaporator, condenser, absorber |
| B | diamond | 2 | 27 | single phase |
| C | diamond | 3 | 27 | single phase, absorber |
| D | rectangular | 1.2 | 26.5 | visualization |

### 3.3.5 Fabrication and materials of manifolds

The manifolds used in this study were 3D printed using polyjet and SLS process. Materials used in 3D printing were ABS plastic and Nylon12. Selection of the materials in this study was based on the chemical compatibility of the manifold

material with the fluids and the operating temperature during the experiments. It was found that Nylon 12 was a preferred material because of its flexibility and less brittle nature than ABS. Injection molding (for polymer materials) or sheet metal forming (for metals) may be used for the mass manufacturing of the manifolds to reduce the cost. Fabrication of the manifold in sheet metal may have several advantages such as high temperature resistance, the smooth surface as compared to the 3D printed plastics to reduce the scale formation.

## 3.4 Outer shell

Function of the outer shell is to hold the pressure on the shell side in the MMHX. Two different types of the outer shells are used in the experiments. For the flow visualization experiments the outer tube is transparent plastic made of PET material. However, a high precision SS304 tube (outer diameter of 1 inch and wall thickness 0.5 mm) was used for all the heat and mass exchange experiments. This particular thickness was chosen only to make sure that the inlet and outlet adopters could fit on this tube.

## 3.5 Assembly

Assembly of the overall absorber/heat exchanger is shown in Figure 3-7. During the assembly process, first of all, the manifold is fitted over the microchannel tube by sliding the manifold over the tube. It is desirable to make sure that the manifold ID matches closely with the OD of the tube. In case the manifold ID is larger, there will be a gap between the manifold ID and tube OD, causing the leakage. On the other hand, if the manifold ID is smaller than that of the tube, either the fitting will not be possible, or the manifold plastic will expand. If the material of the

manifold is flexible (such as Nylon), a tolerance of +/- 0.2mm is typically acceptable. Opposite to this, ABS plastic (stiffer material) starts to crack during the fitting if the tolerance was not appropriate. It should also be noted that the method of 3D printing (with the currently available printing machines) also affects the tolerances. SLS process tends to produce better accuracy than the polyjet printing.
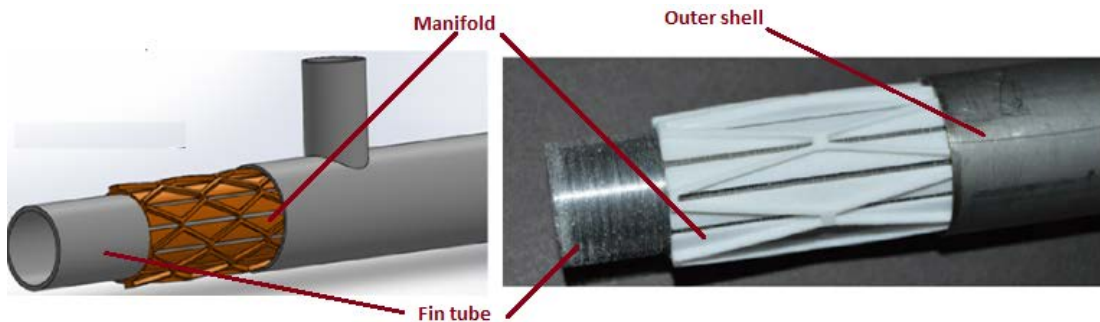


**Figure 3-7:** Assembly of the MMHX showing the microchannel tube, manifold and the shell

After assembling the tube and the manifold, this sub assembly is inserted into the outer shell as shown in Figure 3-7. Length of the outer shell is kept two inches longer than the manifold length to extend 1 inch on both sides of the manifold and the length of the fin tube was 6 inches longer, extending 3 inches on both ends. This extension on the shell at the two ends was to accommodate the inlet and outlet for the shell side fluid and the extension of the fin tube was to accommodate the connections for the tube side fluid. The fins on the extended ends were carefully filled with the epoxy to avoid any leakage of shell side fluid. The epoxy filling process was done inside a vacuum chamber to make sure that no air is trapped inside the fins. Alternatively, the finned tube can be directly ordered with smooth portion at the both ends to ensure a leak proof connection.

The fluid inlet and outlet connections were made using a 1″ to ¾″ tube compression coupling as shown in the Figure 3-8. One additional port was welded to each of these couplings for inlet and outlet of the shell side fluid. For the absorber experiments however, two extra ports were added on the inlet coupling for gas and liquid inlet. A single inlet port was used for all the heat exchangers (liquid-liquid HX, evaporator and condenser) while the two inlet ports were used for the experiments involving the liquid-gas absorption. Instead of metal ferrules, EPDM O-rings were used to seal the couplings. This helped in the replacement of the manifold and the fin tube during different experiments.
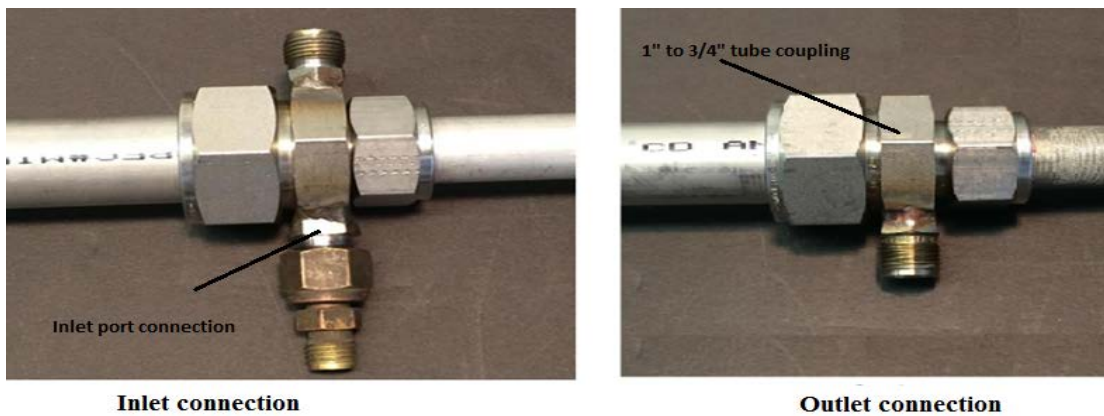


**Figure 3-8:** Inlet and outlet end connection of the MMHX



**Figure 3-9:** Complete assembly of the MMHX used in the experiments

## 3.6   Test sections used in the study

Several test sections have been used in the current work with varying fin tube, manifold type and manifold stage length. A list of different test section geometries has been listed in Table 3-4. The nomenclature presented in this section shall be used throughout this thesis.

**Table 3-4:** List of the MMHX devices used in this study

| Test section | Manifold stage length (inch) | Fin tube type | Outer shell | Application* |
|---|---|---|---|---|
| MMHX 1 | 1.2 | Plain fin (Tube A) | SS | SHX, Evap,Cond, Abs |
| MMHX 2 | 1.2 | Enhanced fin (Tube B) | SS | SHX, Evap |
| MMHX 3 | 2 | Plain fin (Tube A) | SS | SHX, Evap |
| MMHX 4 | 3 | Plain fin (Tube A) | SS | SHX, Evap, Abs |
| MMHX 5 | 1.2 | Plain fin/Tube C | SS | SHX |
| MMHX 6 | 2 | Plain fin (Tube A) | transparent | SHX, Evap, Abs |
| MMHX 7 | None | Plain fin (Tube A) | SS | SHX |
| MMHX 8 | None | Smooth tube | SS | SHX, Abs |

* SHX=single phase Heat exchanger, Evap= evaporator, Cond=condenser, Abs=absorber

## 3.7   Working principle

Figure 3-11 explains the working principle of MMHX. Shell side fluid enters into the MMHX inlet plenum from where it travels axially and enters into the manifold's mixing zone from its all six opening channels in the manifold. As explained in the manifold section, the fluid travels axially into the manifold mixing channel and is eventually forced into the microchannels to flow in radial direction (perpendicular to the axial direction) because the mixing zone channel is closed after one stage. Typical flow stream into the device is represented in the Figure 3-11. Fluid
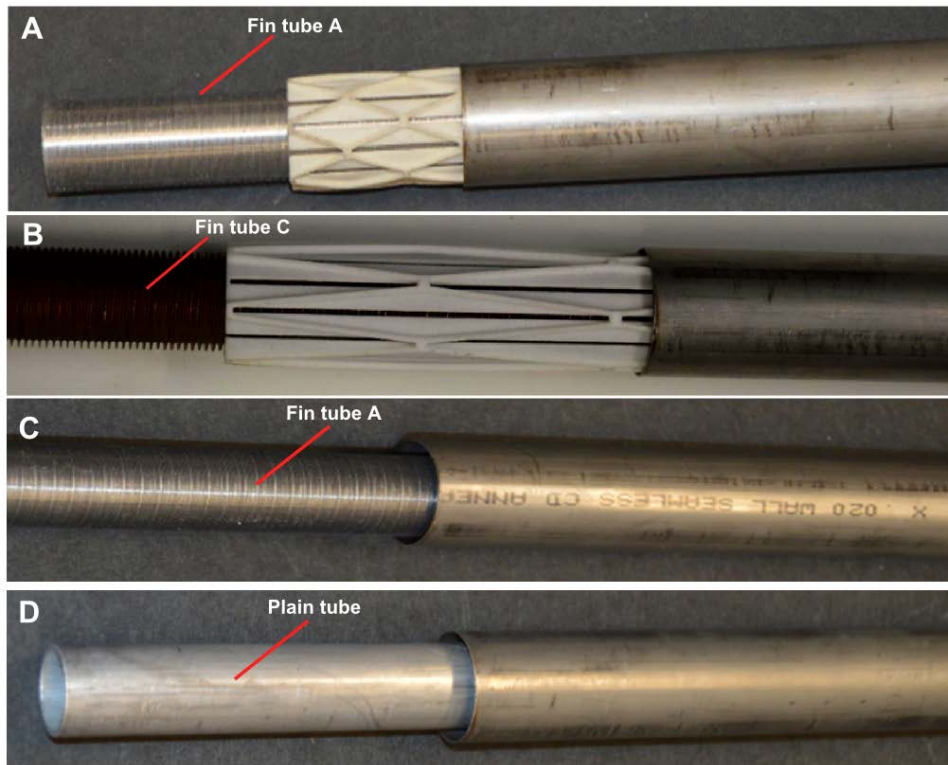
**Figure 3-10:** A) MMHX 1: Fin tube A with manifold.  B) MMHX 5: Fin tube C with manifold. C) MMHX 7: fin tube without manifold and D) MMHX 8: plain tube without manifold

which thus entered into the microchannel gets divided into two streams, moving in the two directions opposite to each other. These fluid streams flowing into the microchannel fins make $90^0$ turn and exit into the two neighboring mixing zones where they make another $90^0$ turn to flow in tube's axial direction inside the mixing zone. They are again forced to enter the next set of microchannels (next pass) due to the blockage of the flow at the end of the stage. This phenomenon is similar in all the six inlet openings of the manifold and continues until the fluid reaches the exit of the device where it comes out of the six outlet channels which are similar to the inlet. Travel length of the fluid into the microchannels per pass (pass length) is approximately ¼ inch. As illustrated in the Figure 3-13, depending upon the ratio of

stage length and the pass length, the fluid flow into the microchannels is only small fraction of the tube length. E.g. for a manifold stage length of 3 inch, the flow into the microchannel per stage is only $1/6^{th}$ of the total device length. This helps in keeping the low pressure drop in the device.

In case of the two phase flow such in a gas-liquid absorber, two separate inlet ports are provided for gas and the liquid which connect to the inlet plenum. The flow process is similar to the above described single phase flow except that the gas and liquid flow together into the microchannels.
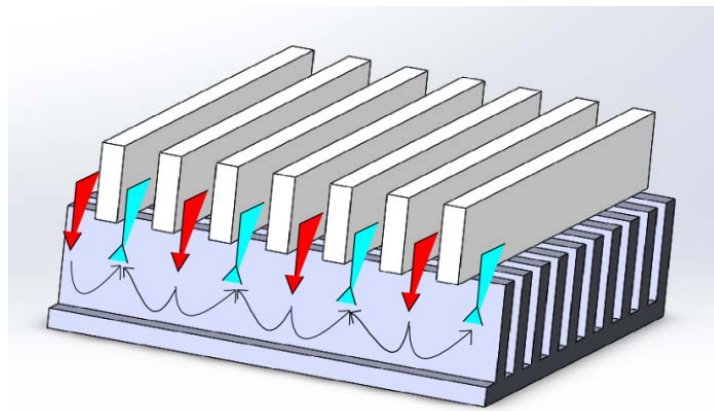


**Figure 3-11:** schematic showing the flow path in the forced fed microchannel
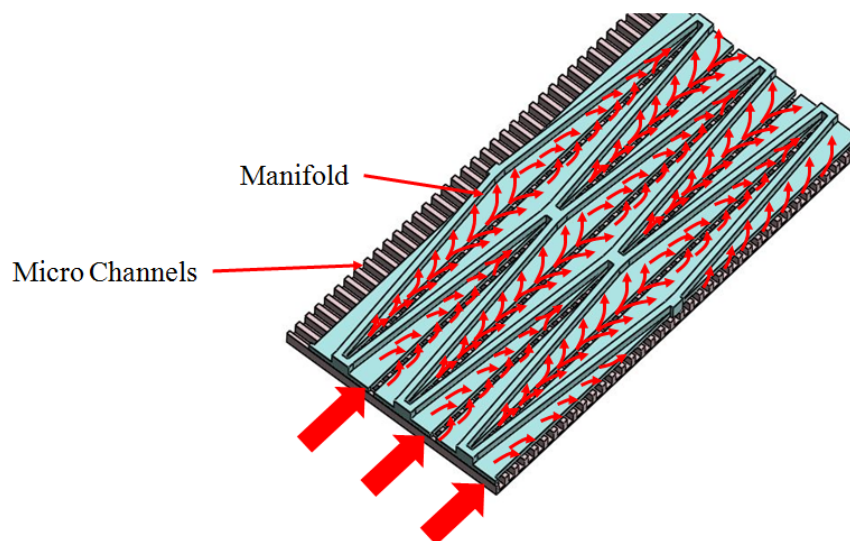


**Figure 3-12:** manifold schematic
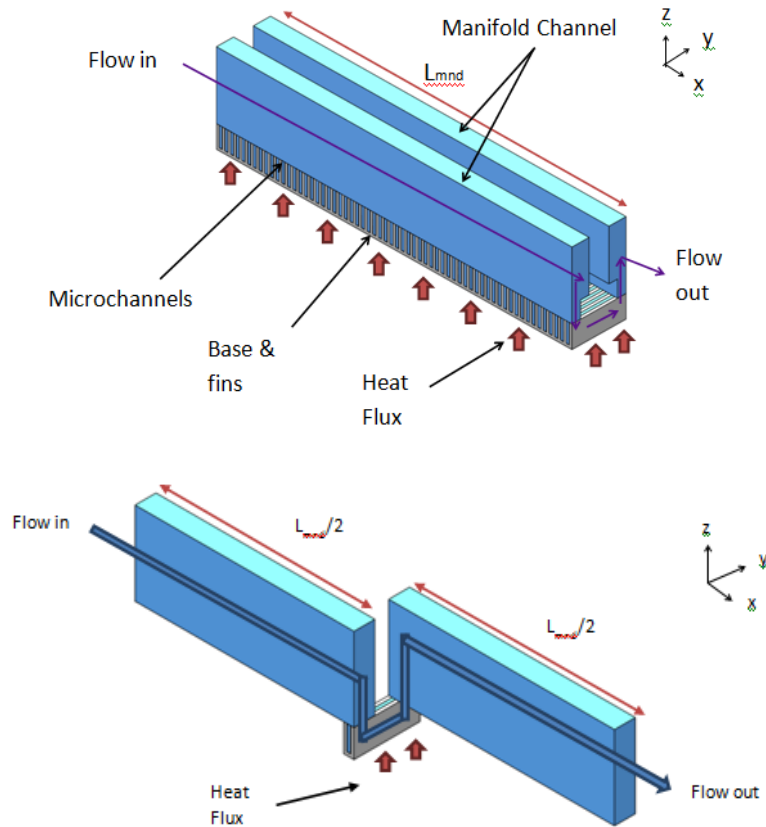
**Figure 3-13:** schematic showing the flow path in the forced fed microchannel

## 3.8 Chapter conclusion

Design and working principle of multipass manifold microchannel heat exchanger has been discussed in this chapter. Design of MMHX is tubular which uses a fin tube as enhanced surface and 3D printed manifolds. Manifold design has multiple stages which help distribution of the flow into the fin microchannels in such a way that the fluid passes through the channel through a very short length in a single pass. The fluid is then mixed in to the mixing plenum of manifold before entering into the next pass. The multiple passes and mixing of the fluid enhance heat and mass transfer in the device while keeping the pressure drop low.

# 4   Flow vizualization study

Visualization study for the MMHX was performed using water and Nitrogen gas to investigate the two phase flow patterns and the flow distribution inside the device. The flow pattern in the device, effect of the leakage and manifold's flow distribution ability was studied.  Test results qualitatively showed that the manifold helped in the flow distribution by breaking the large bubbles into smaller bubbles and thus increasing the interfacial area. Substantial amount of the flow leakage (flow bypassing the microchannels) was noticed for the cases where the finned tube, manifold and outer shell assembly were not tightly fit.

## 4.1   Experimental set-up and procedure

Construction of the test section for the visualization study was similar to the one explained in the previous chapter as MMHX 7 (Figure 4-1).
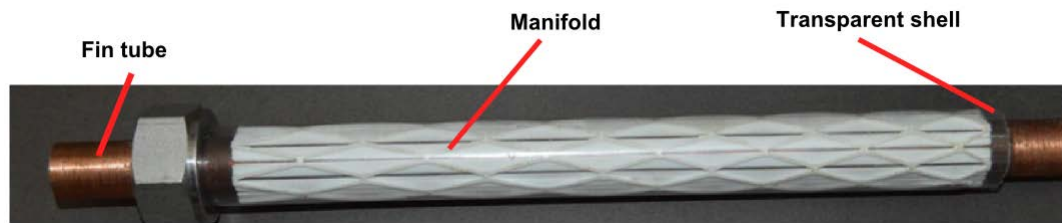


**Figure 4-1:** Test section used for the visualization experiment (MMHX 6)

Experimental setup for the visualization study is shown in Figure 4-2. Water is circulated into the test section by a variable speed pump (Idec GD-M35). Liquid flow is measured with the help of a coriolis flow meter (E+H 83F15). Gas is fed to the test section by a Nitrogen gas cylinder which is regulated by the flow regulators and is measured by the coriolis flow meter (E+H 83A02). The two phase flow is recorded

by a high speed camera (Phantom Miro4) with the help of proper lighting. The video data from the camera is logged directly to the computer. Differential pressure transducer was used to measure the pressure drop across the device. All the instruments data was logged to the computer using data acquisition system (model: Agilent 3970A).
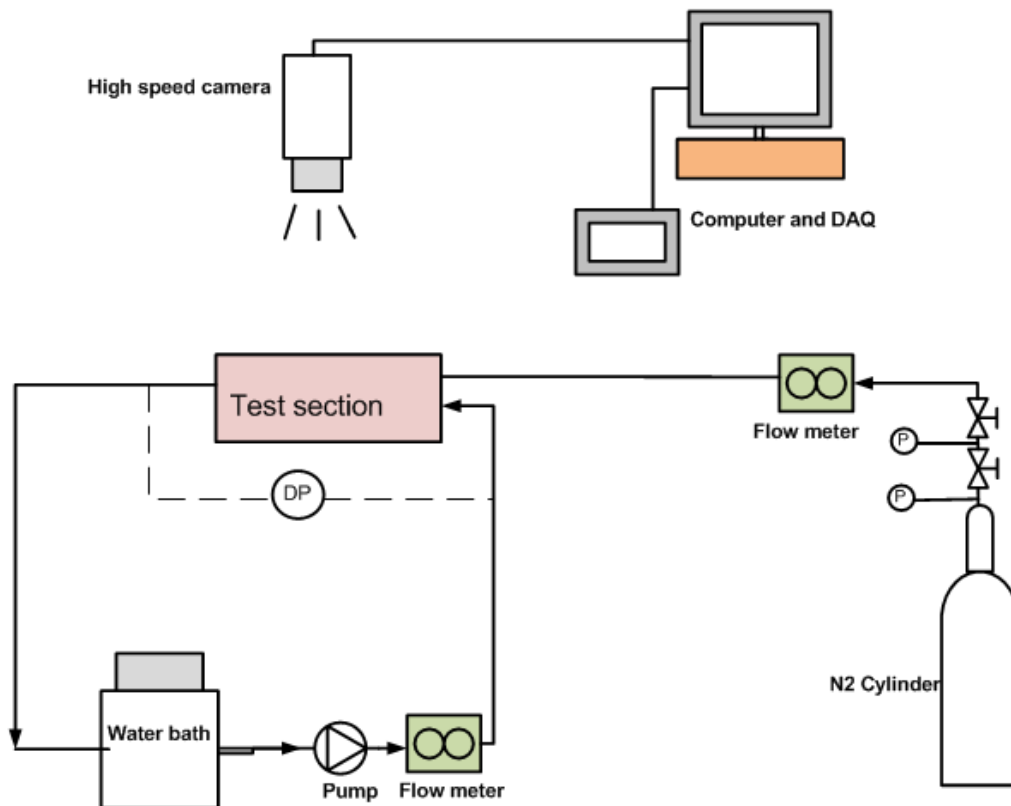


**Figure 4-2:** Schematic of the experimental set-up for flow visualization experiment

Experiments were conducted using water and $N_2$ gas as fluids. Two different manifolds were used for the study: straight rib and diamond shaped ribs. Experiments were performed at room temperature and pressure. Flow rate of the liquid was varied between 5 g/s to 80 g/s while the gas flow was varied from 1 l/min to 75 l/min.

## 4.2 Results and discussion

Two different geometries, diamond shaped ribs and rectangular shaped ribs were compared. The MMHX used the similar fin tube and the manifolds stage length for the two manifolds.

### 4.2.1 Flow distribution

It was observed that manifold in MMHX was able to distribute gas and liquid into the microchannels by breaking the inlet gas stream into the smaller bubbles. In order to visualize the breakup process of a single bubble, very low gas flow rate was used along with 1 l/min of liquid flow rate such that only a single bubble enters the MMHX at a time. It was observed that the gas bubble entered the device from one of the six entrance openings. However, after the first stage length the single bubble broke into several smaller bubbles and covered two mixing zones. In next pass it covered 4 mixing zones and by the third pass, the gas bubbles were distributed into almost all the microchannels in form of small bubbles as shown in Figure 4-3 . Figure 4-3 shows two photographs, one taken at the inlet of MMHX and other after four stages illustrating the single bubble breaking into several smaller bubbles. Similarly Figure 4-4 shows the bubble breakup process for higher gas and liquid flow rates. It is clearly visible that the MMHX geometry helps in gas liquid distribution in the microchannels.
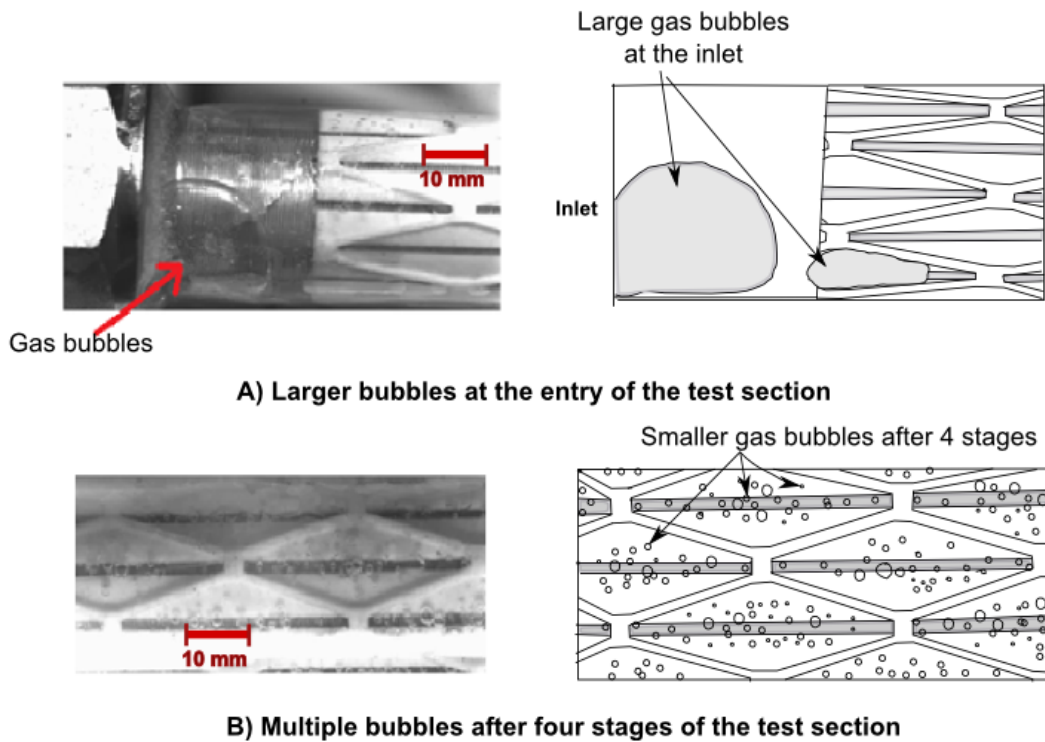
**Figure 4-3:** Bubble breakup illustration inside the MMHX for liquid flow rate of 1 l/m and almost zero (extremely low) gas flow rate (flow visualization and illustration). A) Larger gas bubbles at the entry of the MMHX and B) The larger bubbles at the entry are broken into smaller bubbles after the four manifold stages

### 4.2.2    Effect of liquid and gas flow rate

Experiments were carried out to observe the flow distribution in the microchannels by varying the liquid and gas flow rates. Although the flow inside the microchannels was not visible and it is assumed that it follows similar flow pattern as in typical microchannels as suggested by various researchers such as (Triplett *et al.*, 1999; Chung & Kawaji, 2004). Following observations were made:

1.  At very low liquid flow rates, the bubbles sizes were significantly large.

2.  As the liquid flow rate was increased, size of the bubbles coming out of the microchannels reduced.
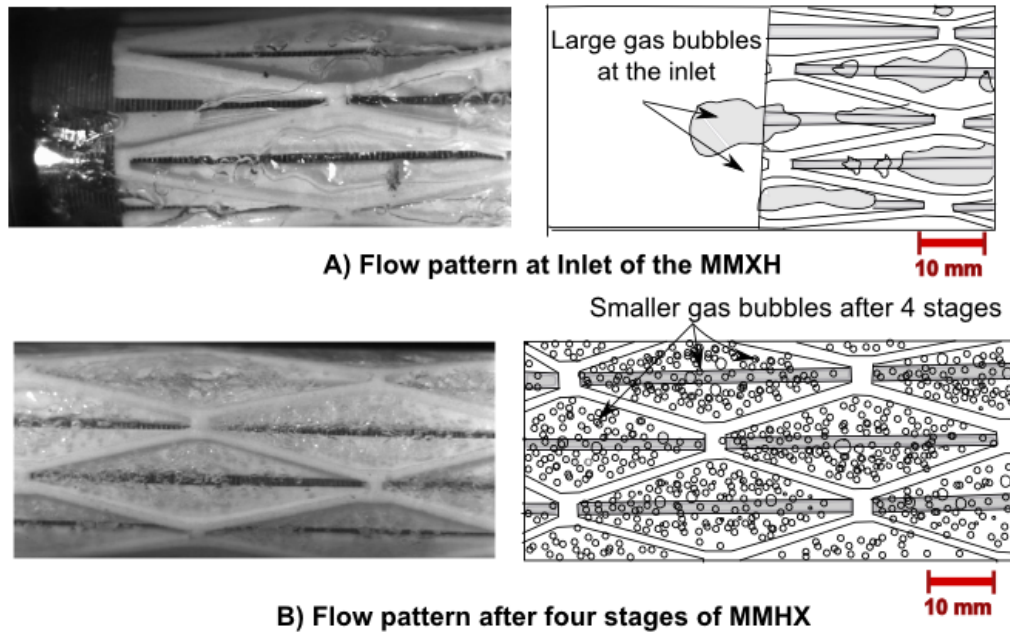
**Figure 4-4:** Flow pattern at the inlet and middle section of the MMHX showing breaking of larger bubbles at inlet of MMHX into smaller bubbles (after 4 stages of manifold) for liquid flow of 4 l/m and gas flow 6 l/m

3. Increasing the gas flow rate for a fixed liquid flow rate reduced the bubble size however this effect of gas flow rate was not significant compared to the effect of the liquid flow rate.

4. For a fixed liquid to gas flow ratio, bubble sizes reduced with the increase in overall volume flow rate of gas and liquid.

Figure 4-5 and Figure 4-6 show the flow pattern observed for various gas and liquid flow rates during the experiments. When the liquid flow rate was increased beyond 4 l/min, flow pattern became bubbly with small bubbles in large number. At higher liquid flow rates, the effect of the gas flow rate on the bubble size was not significant. Entry of the two phase flow into the microchannels from the manifold can be considered similar to the concurrent entry of the two phase flow into a microchannel. The bubble formation process in the microchannel is known as Taylor bubble

formation and since the gas and liquid enter into the microchannels in a similar fashion in the MMHX, the formation/breakup mechanism in the MMHX is expected to be similar to the Taylor bubble formation inside the microchannels. The above results are in line with the Taylor bubble formation mechanism explained in terms of liquid superficial velocity, $j_L$, gas superficial velocity, $j_G$, and two phase mixture velocity, $j_{TP}$ (defined as $j_{TP} = j_G + j_L$) respectively. Superficial velocity is a hypothetical flow velocity calculated as if the given phase or the fluid were the only one flowing in a given cross sectional area.
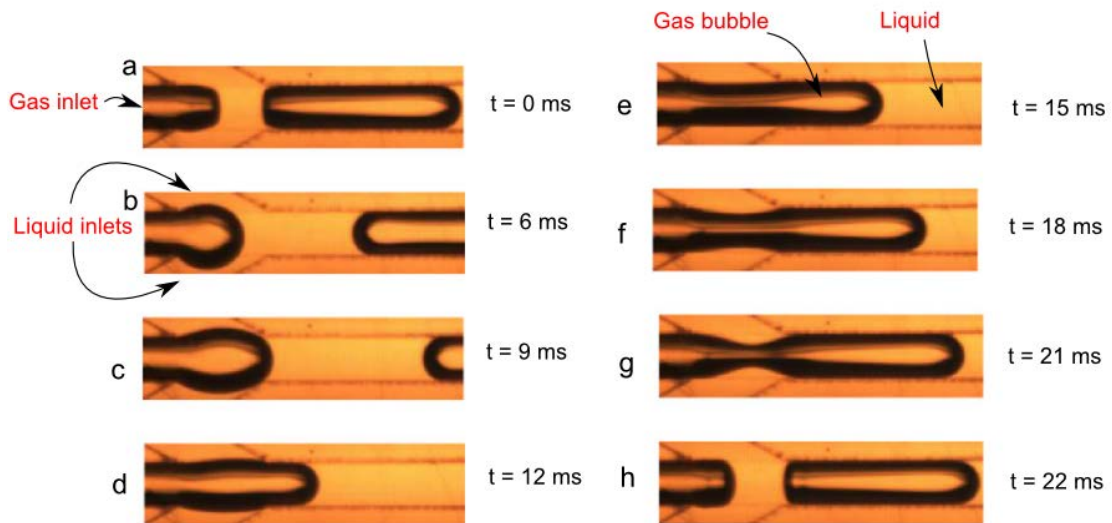


**Figure 4-4:** Taylor bubble formation process inside a microchannel with two liquid and one gas inlet during one period. Gas phase: air; liquid phase: water, $j_G = 0.112$ m/s, $j_L = 0.018$ m/s and channel hydraulic diameter $d_h = 600$ μm (adopted from (Dang et al., 2013))

Figure 4-4 shows the bubble formation process for a single Taylor bubble. Taylor bubble formation in the microchannels is a two step process. First step is the expansion step where the emerging bubble expands both axially and radially until it touches the channel walls and blocks the channel. The time elapsed during this step is

52

called expansion time, $t_e$. Next, the liquid coming out of the inlet starts to put pressure on this gas bubble. The pressure difference across the gas-liquid interface squeezes the emerging the bubble to form a neck at the inlet junction and eventually rupturing the neck. This step is called the rupture step and time taken during this process is called rupture time, $t_r$. Bubble size is reduced with the decreasing $t_e$ and $t_r$. These two steps are related to the competition of various forces acting on the emerging bubble such as surface tension, shear stress and dynamic pressures of liquid and gas. Surface tension tends to suppress both the expansion and rupture steps whereas the shear stress is expected to accelerate both processes. Gas dynamic pressure accelerates the expansion and rupture processes whereas the liquid dynamic pressure accelerates the rupture process. Following conclusions have been drawn during the studies on the bubble breakup phenomena in the literature (Dang *et al.*, 2013):

1. $t_e$ decreases with the increase in gas superficial velocity as the bubble tip blocks the channel quickly. Effect of $j_L$ on $t_e$ is non-monotonic; it increases and then decreases as the liquid superficial velocity is increased.

2. $t_r$ decreases with increasing $j_G$ and $j_L$ as the increase in the dynamic pressures of liquid and gas speed up the rupture process of the neck, however $j_G$ has more dominant effect on $t_e$ than $t_r$ due to the dominant promotional effect of gas on the bubble expansion.

3. $j_L$ has more pronounced effect on the $t_r$ than $j_G$ because the rupture of neck is mainly controlled by the pressure exerted by the liquid at the neck.

4. Reduction in the total bubble breakup time ($t_e + t_r$) results in the smaller size bubbles. Effect of the liquid superficial velocity on the bubble size is significantly higher than the effect of gas superficial velocity. Also, for a given $j_G/j_L$, $t_r$ decrease with increasing $j_{TP}$.

Thus it is clear that with the increase in the liquid and gas velocities, bubble volume reduces. Also, for a given gas to liquid volume flow ratio, the bubble volume reduces with the increase in the two phase mixture velocity.

### 4.2.3    Flow fluctuation

A periodic flow fluctuation in the flow velocity was observed for the cases with higher liquid and gas flow rates. Although it was not visible from naked eyes, the phenomenon was noted in the slow motion visuals recorded from the high speed camera. The frequency of the fluctuation varied with the flow rate. For the higher flow rates, the frequency was higher. It was concluded that the flow fluctuation was caused by entry of liquid and gas flow into MMHX. When the gas pressure in the gas side inlet of MMHX builds up, it forces the gas to enter into the MMHX. After the gas thus enters into the MMHX, pressure in the gas inlet reduces. Liquid inside the MMHX exerts pressure on the incoming gas bubble, causing it to break and restricts the further gas flow. When the gas flow is thus restricted, pressure in the gas inlet starts to increase again forcing the gas flow into the MMHX. This intermittent entry and stoppage of the gas bubbles into the MMHX causes the flow fluctuation observed during the flow visualization. Frequency of the flow fluctuation is related to total bubble breakup time in the manifold inlet. The phenomena is similar to the effect of liquid and gas flow rates on the Taylor bubble breakup process explained in the

previous section where the bubble breakup frequency increases with the increase in gas and liquid flow rates.
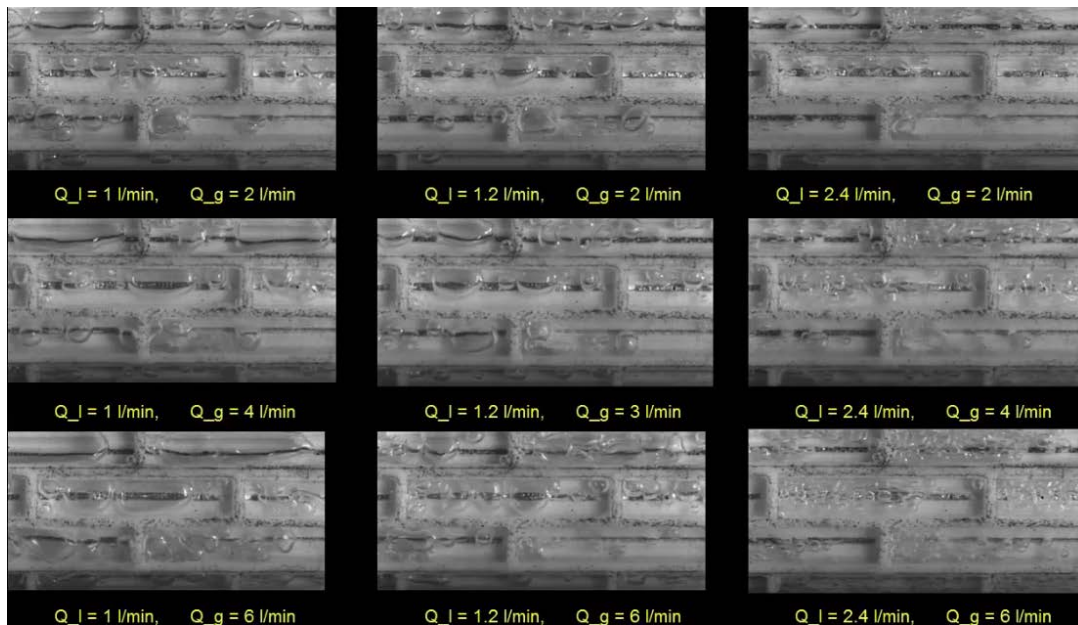


**Figure 4-5:** Flow pattern in the rectangular manifold for varying liquid and gas flow rates

### 4.2.4  Vertical vs. horizontal position of the channel

Visualization experiments were done for both horizontal and vertical orientation of the absorber. It was seen that at lower liquid flow rates, the gas and liquid tended to pass from the inlet side of the horizontally oriented absorber as shown in Figure 4-7 and the back side got very low gas and liquid flows. This was due to the fact that the fluid took the path of least resistance. Keeping the absorber in the vertical position changed the situation with improved flow distribution at low flow conditions. Flow

**A) Flow pattern at liquid flow rate of 2 l/m and gas flow of 6 l/m**

**B) Flow pattern at liquid flow rate of 4 l/m and gas flow of 6 l/m**
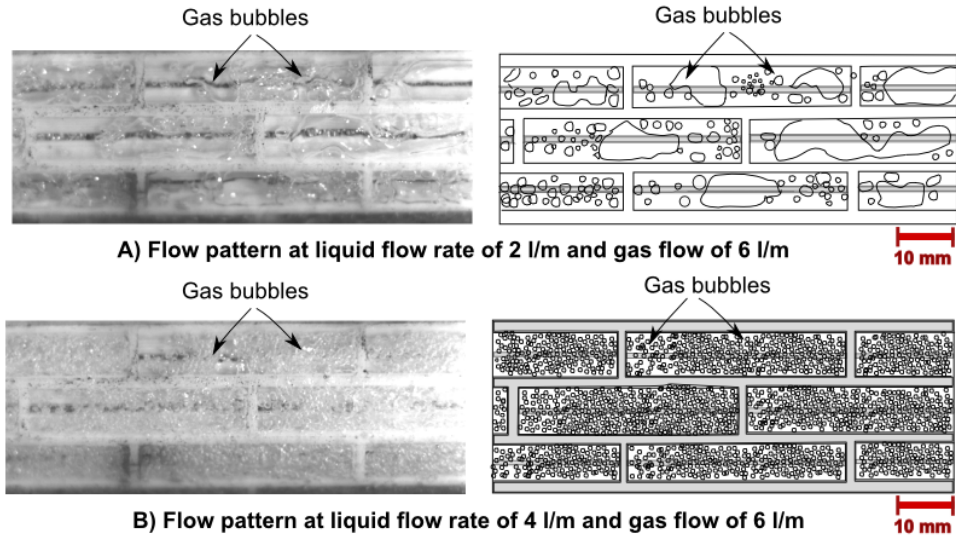
**Figure 4-6:** Effect of liquid flow rate on the flow pattern for a fix gas flow rate

rates in MMHX, however, are much higher and hence no such bypass of the fluid was

visually observed in the device in the horizontal position. Also, proper orientation of

the inlet and outlet may change the flow distribution for low flow condition.
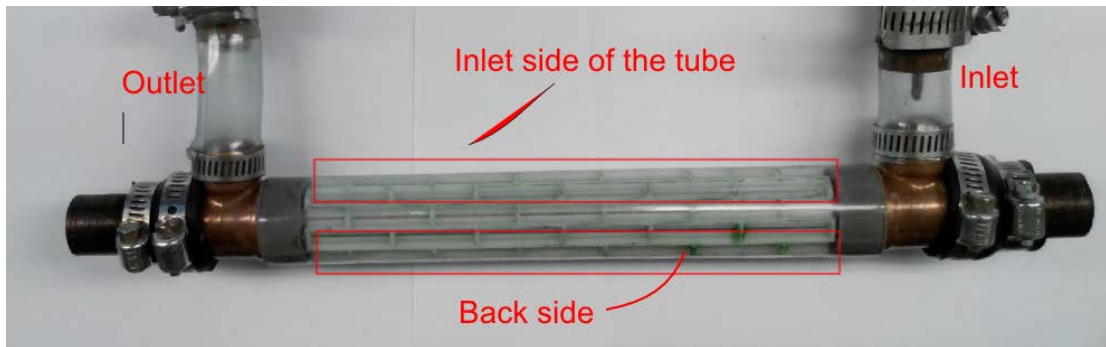


**Figure 4-7:** Test section used for the rectangular microchannel

### 4.2.5    Flow leakage

Several 3D printed manifolds and fin tubes were used during the heat and mass

transfer experiments. Due to the larger tolerance of low cost 3D printing process,

inner and outer diameter of each manifold varied within 0.2mm. Thus some of the

manifolds were tight fit on the fin tubes and inside the outer shell and others were

loose fit. It was observed that if the manifold was not tight fit into the MMHX, part of the fluid leaked through the gap between the manifold and outer shell and gap between the manifold and fin tube instead of being forced through the microchannels. To avoid the leak problems, future manifolds were fabricated with much softer Nylon 12 material. SLS technology was used which uses laser sintering instead of UV curing to retain the properties of the nylon plastic. The dimensional accuracy in this case was much better. The superior strength and the flexibility of nylon enabled us to stretch and tight fit the manifold on the fin tube. Width of transverse rib of the manifold was increased from 1 mm to 2 mm for all future manifolds to make sure that the ribs did not crack during the fitting of the manifold on the fin tube.

To ensure almost 0% leakage, the loose fit manifold was tightly wrapped with a plastic sheet (to form a sleeve) on the outer of the manifold as shown in Figure 4-9. To test the effect of leakage on flow distribution, the visualization experiments were done using both the loose fit manifold and plastic sheet wrapped manifold. No leakage was observed in the MMHX with sleeve. Results of the flow visualization in the loosed fit manifold are shown in Figure 4-8 while the same after putting the sleeves are shown in Figure 4-10. Increased number of bubbles in Figure 4-10 as compared to Figure 4-8 are clearly evident. Experiments on the MMHX absorber have shown that the interfacial area in the manifolds with sleeves is almost double as compared to the loose fit manifold.

### 4.2.6    Pressure drop

Two phase pressure drop was recorded during all visualization experiments. Figure 4-11 shows the variation of pressure drop with the changing liquid and gas flow rates.

As expected, the results show that the pressure drop increases with the increase in liquid and gas flow. However, the effect of liquid flow rate on pressure drop is more dominant.
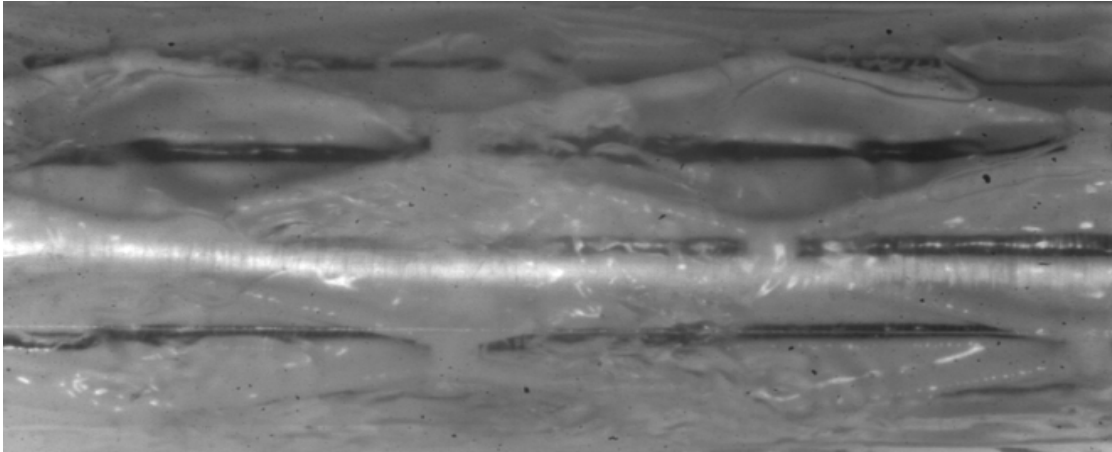


**Figure 4-8:** Two phase flow in the loose fit manifold showing the leakage of the gas through the gap between the outer shell and manifold ribs. (liquid 2 l/min, gas 6 l/m)



**Figure 4-9:** Transparent plastic sheet is wrapped around the manifold to stop the leakage
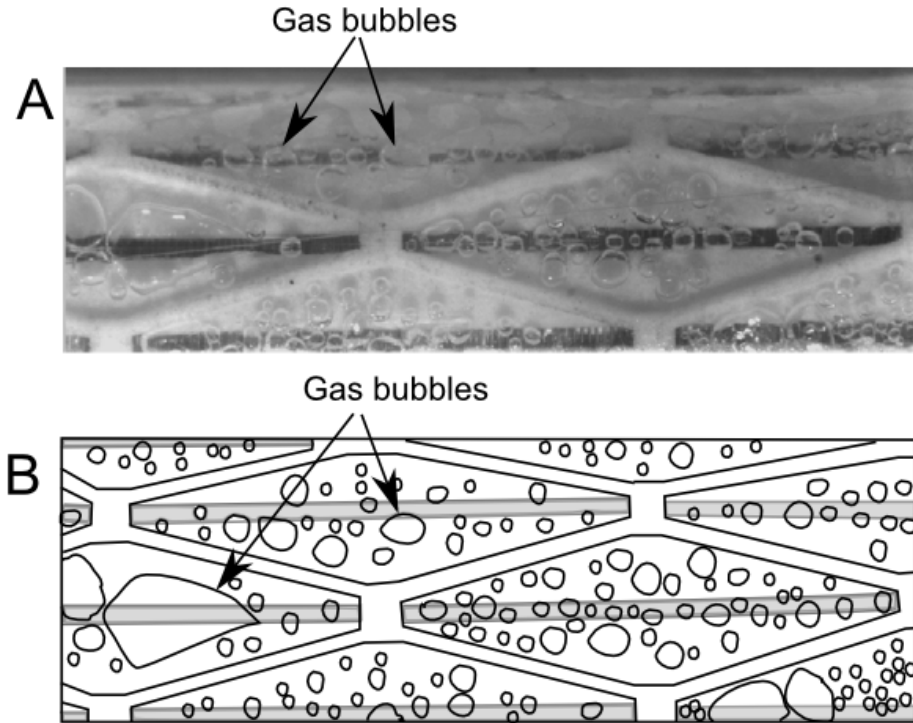
**Figure 4-10:** Flow pattern for the similar flow conditions as in **Figure 4-8** but with tight fit manifold (with the sleeves) showing bubbly flow (liquid 2 l/min, gas 6 l/m)
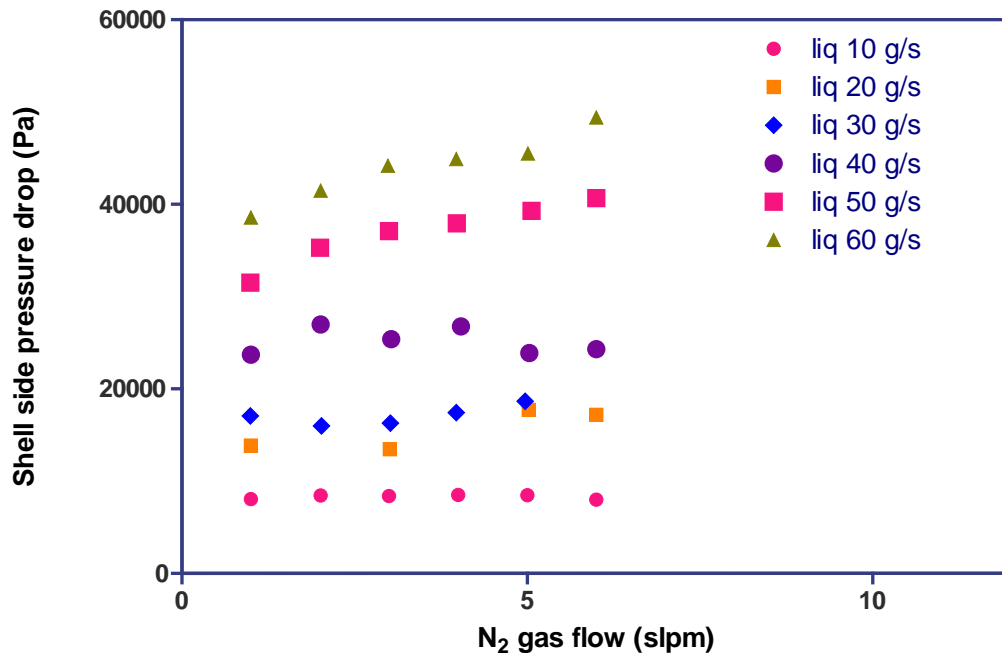


**Figure 4-11:** Variation of two phase pressure drop with the liquid and gas flow
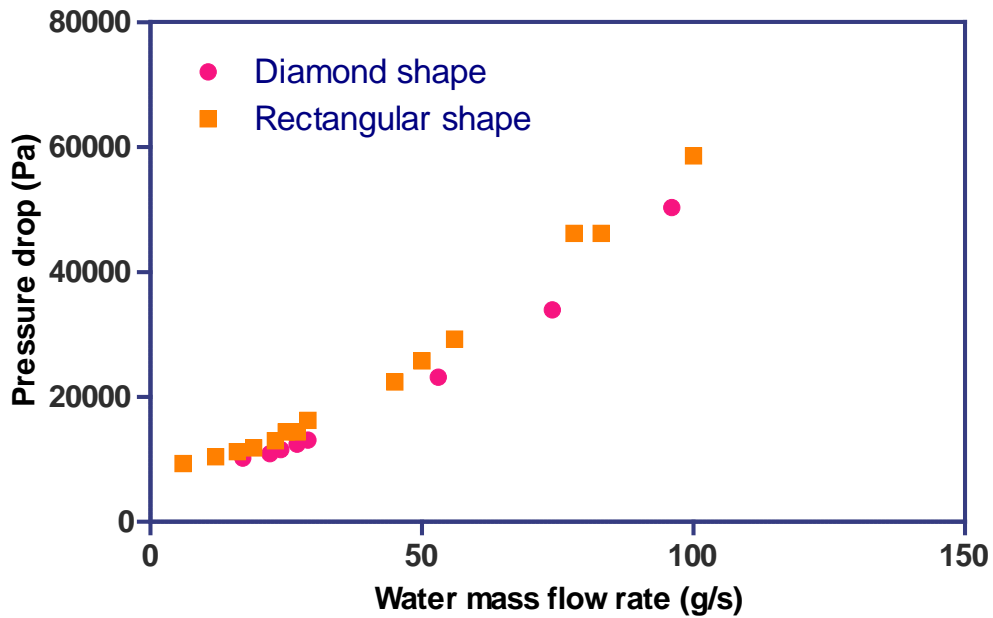
**Figure 4-12:** Comparison of the pressure drop of diamond shape and rectangular shape microchannel

Figure 4-12 shows the comparison of the pressure drop in rectangular rib and diamond shape manifold. Pressure drop in the diamond shape manifold absorber is slightly lower than in rectangular rib manifold. This effect is attributed to the velocity distribution of liquid flow in the manifold plenum. Since the liquid enters into the plenum from series of microchannels, starting from one end up to its center and then starts to exit from the plenum starting from the center until the other end, the mass flow of the liquid is lowest at the two ends of the manifold plenum and is highest at the center. In a rectangular shape plenum the flow velocity component (parallel to the fin tube axis) is higher at the center and is lower at the two ends. However, the diamond shape manifold's flow area is lowest at the ends and increases towards the center in proportion to the flow rate. Thus the flow velocity in the diamond shape manifold is almost constant throughout the plenum. As the pressure drop is

proportion to second power of velocity, the pressure drop in the uniform velocity profile is lower as compared to the linearly changing velocity profile.

The current design is an improved version of the manifold design used by (Andhare, 2013) for single phase experiments. These improvements included the changing the manifold pass length and the shape of the manifold for better distribution of two phase flow and reduced pressure drop. Manifold stage length and microgroove pass width selection is an important parameter which decides the pressure drop, heat and mass transfer inside the tubes. As the velocity in the channels and manifold plenum increases, heat transfer and pressure drop increase.

In order to get a good design, optimization of pressure drop and heat transfer is required. Current manifold stage length selection was based on the single phase heat transfer optimization using fluent and MATLAB models by Arie *et al.* (2014).

### 4.2.7    Uneven velocity distribution in the absorber

As discussed earlier, vapor quality or gas fraction in the MMHX for two phase applications keeps changing as the along the length of the device. This creates the uneven velocity distribution along the length with the higher velocity at the location of higher vapor quality. Two methods can be used to create the even pressure drop along the length of MMHX: 1) using multiple vapor inlets along the length (for condenser and absorber applications) and 2) design the variable stage length manifold to accommodate the change in vapor quality. The first method is cumbersome as it requires the additional connections along the length of MMHX. Controlling of the pressure drop in these inlet lines poses another difficulty. Also, at different operating conditions this would require the adjustments in the valves which are not practical.

Thus the second option is chosen where the length of each manifold stage varies with the quality of two phase flow. E.g. The length of the manifold reduces with the length of the absorber.

## 4.3 Chapter conclusions

Flow visualization experiments with multipass MMHX were performed to analyze the flow distribution in the device. The following are the conclusions from the visualization studies:

1. Visual comparison of two phase flow in diamond shape and the rectangular shape manifold geometries indicated that the flow distribution is qualitatively better in the diamond shape manifolds where the bubbles were coming out of the majority of microchannels. The pressure drops in the diamond shape manifolds were slightly lower than that in the rectangular manifolds.

2. Lower liquid flow rates in the MMHX resulted in the coalesced bubbles flow in the manifold. As the liquid flow rate increased, the bubble size in the MMHX became smaller. Similar trend was noticed for the increase in the gas flow rate, however, the effect of gas flow rate on the bubble size was not as significant.

3. Significant amount of the leakage was noticed when the manifold was not tight fit with the fin tube or outer shell in MMHX. Comparison of flows in the tight fit and loose fit manifolds showed that more amount of bubbles were formed in the tight fit MMHX indicating that the gas was forced into the microchannels in case of the tight fit manifold where as for the loose fit

MMHX, gas mostly bypassed the microchannels and leaked through the gap between the manifold and outer shell.

4. Flow in the horizontal orientation MMHX showed the flow bypass in the MMHX for very low liquid flow cases. Fluid took the least resistance path instead of being distributed uniformly in the device. Vertical orientation of MMHX showed better flow distribution for very low liquid flows. However, it should be noted that in almost all the applications, these low flow rates are not encountered and hence the orientation of the MMHX is not an issue.

5. MMHX showed the capability to distribute the uneven flow due to its multipass design. Such flow distribution can greatly benefit the two phase applications such as evaporator, condenser and gas-liquid reactors.

# 5 Single phase heat transfer experiments

Experimental investigation of single phase heat transfer and pressure drop inside the MMHX are reported in this chapter. Experiments were carried out with water as working fluid on both shell and tube sides. Different fin tubes were used in combination with different manifold sizes. The experiments were also performed to compare the effect of manifold on the heat transfer by using the double pipe geometry without a manifold.

## 5.1 Introduction

Manifolds have been used in microchannel heat exchangers as early as 1990s (Harpole & Eninger, 1991). Several researchers have studied the manifold design since then (Copeland, 1995; Copeland *et al.*, 1997; Kim *et al.*, 1998; Poh & Ng, 1998; Ryu *et al.*, 2003; Jang & Kim, 2005; Jankowski *et al.*, 2007; Wang *et al.*, 2007; Wang & Ding, 2008; Xia *et al.*, 2008; Haller *et al.*, 2009; Kermani *et al.*, 2009; Escher *et al.*, 2010; Sharar *et al.*, 2010). Thermal resistance inside the microchannel depends upon various factors such as microchannel geometry, the geometry of the manifold and the pumping power. As discussed in the previous chapter, use of manifold microchannel heat exchanger typically causes the flow to be in the hydrodynamically as well as thermally developing regions and hence has typically higher heat transfer and pressure drop performance. Kim *et al.* (1998) showed that during forced air heat transfer experiments the heat transfer and the pressure drop performance was improved as high as 35% compared to that in traditional microchannels.

Majority of these studies were focused on microchannel heat sinks for the electronic cooling application rather than the industrial scale heat exchanger. Microchannel manifold heat exchanger study for industrial application is scarce in the literature. This work is an attempt to study the effect of novel microchannel manifold heat exchanger design on single phase heat transfer for industrial applications.

## 5.2   Experimental setup

### 5.2.1   Test section

Experimental setup schematic is shown in the Figure 5-1. The details of the equipment and instruments used are given in the Appendix A. Cooling water was fed to the tube side of the finned tube while the hot water was fed on the shell side (manifold side) of the tube. In order to minimize the heat losses to the ambient and the error due to that, the temperature of the hot water was maintained close to the atmospheric temperature and the test section was properly insulated with Poly Urethane Foam.

Cooling water was fed to the device with the help of a Neslab chiller (HX500) while the hot fluid was fed to the MMHX by a variable speed screw pump (Idec GD-M35).   The temperature of the shell side water was maintained at constant temperature by using a 3.0 kW electric heater and a 3.0 kW chiller (Neslab M72) as shown in Figure 5-1. Flow rates for both shell and tube water streams were measured with the help of high accuracy coriolis flow meters (Endress Hausser 83A02 and 83F15 respectively). Pressure drops across the hot side and cold side fluid were measured using diaphragm type differential pressure transducers (Validyne P55D).

Inlet and outlet temperatures of shell side were measured using thermocouples (three thermocouples at each point). Since the flow rate of the cold (tube) side was much higher (10-20 times) than that on the hot (shell) side, the change in temperature was relatively lower on cold side (typically 1 $^{\circ}$C - 2 $^{\circ}$C). This range of temperature difference cannot be measured accurately using the standard thermocouples with the accuracy of (±0.2 $^{\circ}$C to ±0.5 $^{\circ}$C). Thus a differential thermocouple technique was used to achieve the higher accuracy. Similar differential was also used to measure the temperature difference on shell side. The concept of differential thermocouple is discussed in the following subsection.

The experimental data from different instruments was recorded using an Agilent data Acquisition system every two seconds. However, only steady state data was taken for the data reduction purposes.
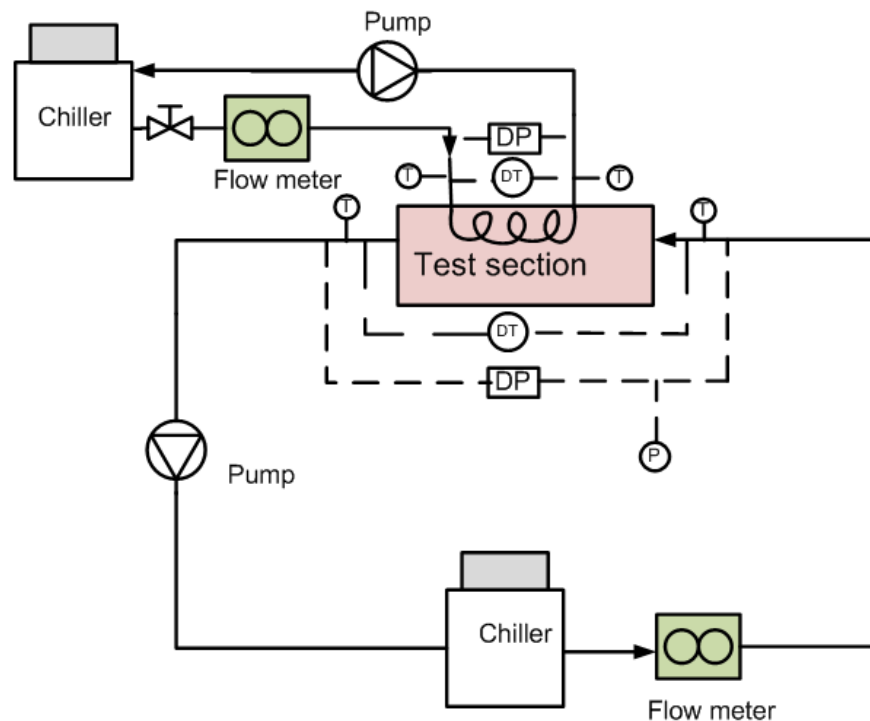


**Figure 5-1:** Schematic of the experimental setup for single phase heat transfer experiments

### 5.2.1.1 Differential thermocouple

As discussed in the previous section, the temperature difference of the tube side fluid is low (0.7 $^\circ$C to 2 $^\circ$C). Thus the measurement of this temperature difference using the thermocouples shall result in the errors as high as 50% as the accuracy of the typical thermocouples are close to ±0.5 $^\circ$C. By using the carefully calibrated thermocouples or using multiple thermocouples this error can be somewhat reduced but will still be not accurate enough for the energy balance purposes. Thermocouple system has several factors contributing to its inaccuracy such as inaccuracies related to the reference point cancellation, the voltmeter inaccuracy and noise. For example, EMF of thermocouples is very low (about 40 µV per $^\circ$C), an accuracy of 0.1 $^\circ$C requires the voltmeter to read 4 µV accurately which requires highly accurate voltmeters.

It should be noted that for the data reduction purposes, the temperature difference between the inlet and outlet of the cooling water and of the refrigerant was needed rather than the absolute temperatures of the inlets and the outlets. Thus, it was decided to use differential thermocouple using 4 junction thermopile as shown in the Figure 5-2. Accuracy of the differential temperature measurement using this method was ±0.07 $^\circ$C.

The thermopile used in the study had four junctions as shown. The voltage generated by each of these junctions was proportional to temperature difference between the hot and cold temperatures to be measured. These junctions were insulated using thin epoxy coating to make sure that the ends of thermocouples do not short circuit either by direct contact or when they are in contact with water. The end

junctions were connected to the data acquisition system and are measured as voltage signal rather than the thermocouple signal. Differential temperature measurement using thermopiles improves the accuracy in two ways. First of all, since it directly measures the temperature difference, it's not needed to combine the inaccuracies of two thermocouples at the inlet and outlet. Secondly, the voltage change in the thermopile is proportional to the temperature difference between the inlet and the outlet. As shown in the Figure 5-2 the thermocouple junctions are connected in series. Hence the voltages generated between the hot and cold junction is the addition of the voltages generated between each pair of hot and cold junctions. If the 'n' junctions are used in the thermopile, the voltage generated in the thermopile shall be 'n' times the voltage generated for a single pair of junction. This results in improving the accuracy of the measurement to a significant amount.
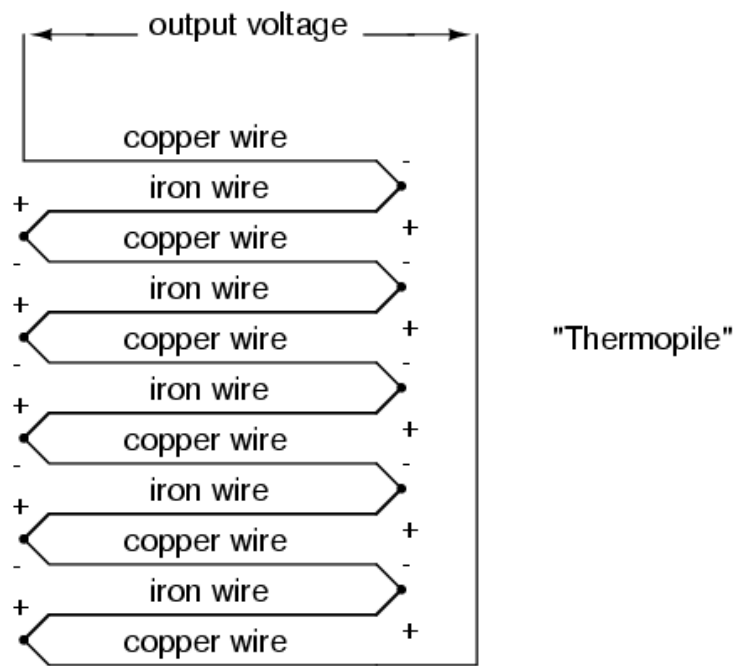


**Figure 5-2:** Schematic of a typical differential thermocouple.

### 5.2.2 Procedure

Experiments were performed to investigate the heat transfer and pressure drop in MMHX. Various parameters such as liquid flow rates, microchannel geometry and manifold geometry were varied in this study. Details of these parameters are the following:

- Water flow rate on shell side was varied from 7 g/s to 80 g/s

- Size of manifold: Three different manifold sizes were used where the stage lengths were 1.2 inch, 2 inch and 3 inch

- Four different fin tubes used during the experiments

Experiments were performed by keeping the flow rate on the cold side to maximum possible (limited by the chiller pump) in order to minimize the resistance on the tube side. Temperature of the inlet cold water flow was typically kept constant at 7 $^{\circ}$C. Hot water was fed counter current while the inlet temperature was maintained at room temperature (~ 26 $^{\circ}$C). Depending upon the hot water flow rate, temperature difference between inlet and outlet of the cold side was varied between 5 $^{\circ}$C to 15 $^{\circ}$C. Shell side flow rate was varied and temperature and pressure drop across both the liquid streams were recorded for each case.

## 5.3 Data reduction

### 5.3.1 Flow inside the fin tube (cold side)

Average velocity and Reynolds number inside the tube can be obtained using following equations:

$$\dot{m} = \rho A_{flow} v \tag{6}$$

$$A_{flow} = \pi D_i^2 / 4 \tag{7}$$

$$Re = \frac{\rho v D_i}{\mu} \tag{8}$$

Where ṁ is mass flow rate, $\rho$ is the density of fluid, $A_{flow}$ is the cross sectional area normal to the flow direction, v is the average flow velocity, $D_i$ is the tube internal diameter, Re is Reynolds number and $\mu$ is the dynamic viscosity. Pressure drop and heat transfer coefficient inside the enhanced fin tube can be calculated using the correlations provided by the tube manufacturer as following:

**Table 5-1:** Correlation coefficients

| Parameter | Tube A | Tube B |
|---|---|---|
| Tube model no. | 95-4350028 | 95-4350035 |
| STC | 0.078 | 0.078 |
| C | 1.773 | 1.773 |
| D | 0.331 | 0.331 |

$$f_{darcy} = CRe^{-D} \tag{9}$$

$$DP = \frac{f_{darcy} l \rho v^2}{2D_i} \tag{10}$$

Where, $f_{darcy}$ is Darcy friction factor, DP is the pressure drop, $l$ is the length of the tube and C and D are the coefficients. Heat transfer coefficient inside the tube is calculated using the following correlation using thermal conductivity $k$, Prandtl number Pr and dynamic viscosities at close to the tube wall, $\mu_{wall}$:

$$h_i = \left(\frac{k}{D_i}\right)(STC)Re^{0.8}Pr^{(1/3)}\left[\frac{\mu}{\mu_{wall}}\right]^{0.14} \tag{11}$$

### 5.3.2 Manifold side calculations

As shown in Figure 3-13, flow on the shell side passes through the manifold plenum and through the microchannels alternatively. Length of the flow into the microchannel is termed as pass length, whereas, length of one manifold plenum is

called as stage length. Considering the flow in a single stage length; fluid enters into manifold plenum from microchannels from two sides in first half length of plenum and divides into two streams in the second half to enter into the microchannels. Thus the fluid effectively moves within four microchannel passes in one stage length. Thus there are four numbers of passes in a single stage for a single fluid entry into the manifold. As can be seen from the manifold drawing, there are total six fluid entries into the manifold.

Hence number of passes within the device can be calculated as the following:

$$n_{pass,total} = 4 \cdot n_{stage} n_{entry}$$

(12)

Number of manifold stages $n_{stage}$ in a length $L$ of the device can be given in terms of the stage length $l_{stage}$ as

$$n_{stage} = \frac{L}{l_{stage}}$$

(13)

Number of microchannels per pass can be calculated from the following equation

$$n_{channel/pass} = \frac{(l_{stage}/2)}{pitch_{channel}}$$

(14)

The mass flux, flow velocity and Reynolds number inside the microchannel can be calculated as

$$\dot{m}_{flux} = \frac{\dot{m}}{2A_{cross,channel} n_{channel/pass}}$$

(15)

$$V_{channel} = \frac{\dot{m}_{flux}}{\rho}$$

(16)

$$Re = \frac{\rho V_{channel} D_h}{\mu}$$

(17)

Since the fluid flows through the multiple passes, the pressure drop is calculated by finding the average friction factor in a single pass and then multiplying it by the number of passes. Pressure drop into the manifold and the entry and exit into the microchannels has been numerically calculated by (Arie *et al.*, 2015) for different types of manifolds. It was reported that the pressure drop in the microchannel is typically more than 80-90% of overall pressure drop for a well optimized manifold. Heat transfer in the heat exchanger is given by the following equation

$$Q_{manifold} = \dot{m} C_p \left( T_{cold_{out}} - T_{cold_{in}} \right) \tag{18}$$

Overall heat transfer coefficient can be calculated as

$$U = \frac{Q}{A \cdot LMTD} \tag{19}$$

Where logarithmic mean temperature difference, LMTD, is defined as:

$$LMTD = \frac{\left( T_{hot_{in}} - T_{cold_{out}} \right) - \left( T_{hot_{out}} - T_{cold_{in}} \right)}{ln \frac{\left( T_{hot_{in}} - T_{cold_{out}} \right)}{\left( T_{hot_{out}} - T_{cold_{in}} \right)}} \tag{20}$$

Where, $T_{hot_{in}}$, $T_{hot_{out}}$, $T_{cold_{in}}$, $T_{cold_{out}}$ are the hot side and cold side inlet and outlet temperatures respectively. Heat transfer coefficients are calculated based on the base area of the microchannel tube. Water side heat transfer coefficient $h_i$ is calculated by the correlation provided by the fin tube manufacturer. Manifold side heat transfer coefficient $h_o$ can be obtained by the following equation

$$\frac{1}{UA} = \frac{1}{h_i A_i} + \frac{ln \left( \frac{D_o}{D_i} \right)}{2 \pi k l} + \frac{1}{h_o A_o} \tag{21}$$

Where $D_o$ is the outside diameter of the fin tube as shown in Figure 3-5. Heat transfer surface area for the inner and outer surfaces is calculated as follows:

$$A_i = \pi D_i L \tag{22}$$

$$A_o = \pi D_o L \tag{23}$$

### 5.3.3 Uncertainty analysis

Uncertainty analysis was performed using law of propagation of uncertainty as:

$$\delta R = \sqrt{\sum_{i=1}^{N} \left( \frac{\delta R}{\delta X_i} dX_i \right)^2} \tag{24}$$

**Table 5-2:** Parameters and estimated uncertainties

| Parameters | Uncertainty (max) |
| --- | --- |
| Temperature ($^\circ$C) | $\pm$0.50 $^\circ$C |
| Temperature difference ($^\circ$C) | $\pm$0.05 $^\circ$C |
| Water mass flow rate | 0.1% |
| Refrigerant mass flow rate | 0.1% |
| Log mean temperature difference | 3.3% |
| Heat duty | 2.8% |
| Overall heat transfer coefficient | 4.5% |
| Refrigerant side heat transfer coefficient | 5.2% |
| Pressure drop (Pa) | 0.25% |
| Absolute pressure | 0.2% |

Where

$$R = R(X_1, X_2, X_3, X_4, \dots \dots X_N) \tag{25}$$

Different parameters and the estimated uncertainties are presented in Table 5-2.

## 5.4  Results and discussions

### 5.4.1  Effect of shell side liquid mass flux and manifold stage length

Shell side heat transfer coefficient vs. liquid Reynolds number inside the manifold is shown in

Figure **5-3**. Shell side heat transfer coefficient increases with the increase in the liquid velocity. This increase in the heat transfer can be attributed to the hydrodynamically developing flow inside the microchannels. As discussed in chapter 2, increase in the flow velocity results in the higher ratio of developing length to the microchannel flow length per pass. When the fluid enters the channel, a boundary layer starts to develop with the increasing channel length due to the viscous effects. This development occurs until the boundary layer merges with the centerline of the channel. Since the boundary layer closer to the entrance of the channel is thinner, the heat transfer is higher near the entrance. Similarly, when the uniform temperature fluid enters the channel, the thermal boundary layer starts to develop due to the convection heat transfer and the heat transfer at the entrance region is higher due to lower boundary layer thickness.

It was found that the shell side heat transfer coefficient increases with the decreasing manifold size. This can be understood as following: Reducing the stage length also increases the number of passes in the device and hence number of microchannels in each pass. This causes the increase in liquid mass flux inside the microchannel for the same liquid flow rate. Since flow inside the microchannels is in developing zone, the Nusselt number and hence the heat transfer coefficient with are higher. The similar trend is shown for overall heat transfer coefficient (Figure 5-6).

Pressure drop variation for different liquid Reynolds numbers is shown in the Figure 5-5. As expected, pressure drop increases monotonically with the increase in liquid flow rate due to the increase in friction factor with flow velocity. It is also evident from the graph that the pressure drop in the MMHX depends upon the stage length of the manifold. E.g. the pressure drop in a 2 inch manifold is lower than that in 3 inch manifold. This can be understood as following: Manifold stage length governs the mass flux into the microchannels for a given liquid flow rate into the device. Smaller stage length manifolds have lower number of microchannels per pass and hence higher mass flux for a constant flow rate. Also, total number of flow passes in MMHX increase with decreasing stage length of manifold. Thus the total length fluid travels inside the microchannels increases with decrease in stage length. These two factors cause higher pressure drop for smaller stage length manifold MMHX.

From the heat exchanger design point of view, the best configuration should yield the highest heat transfer coefficient with the minimum pumping power requirement. Pumping power is defined as the product of volumetric flow rate and pressure drop. Since both the pressure drop and the heat transfer coefficients are higher for the lower manifold stage length manifolds, a comparison of the shell side heat transfer coefficient with the shell side pumping has been presented in Figure 5-7. For any given pumping power the heat transfer coefficient was found to be maximum for 1.2 inch manifold stage length.
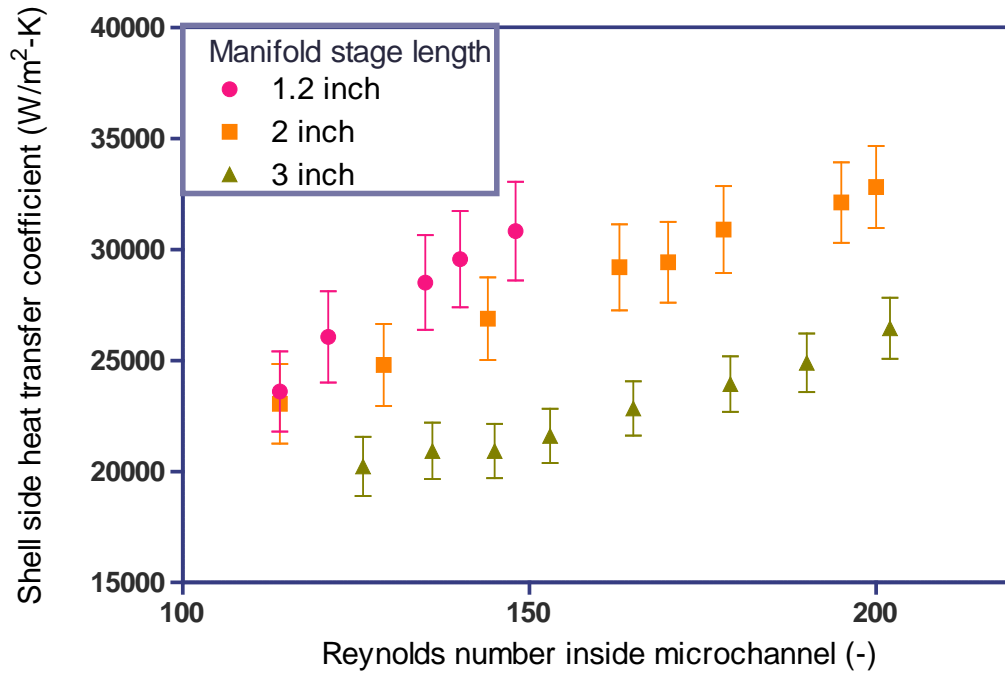
**Figure 5-3:** Variation of shell side heat transfer coefficient with liquid Reynolds number inside the microchannels for three different manifold stage lengths
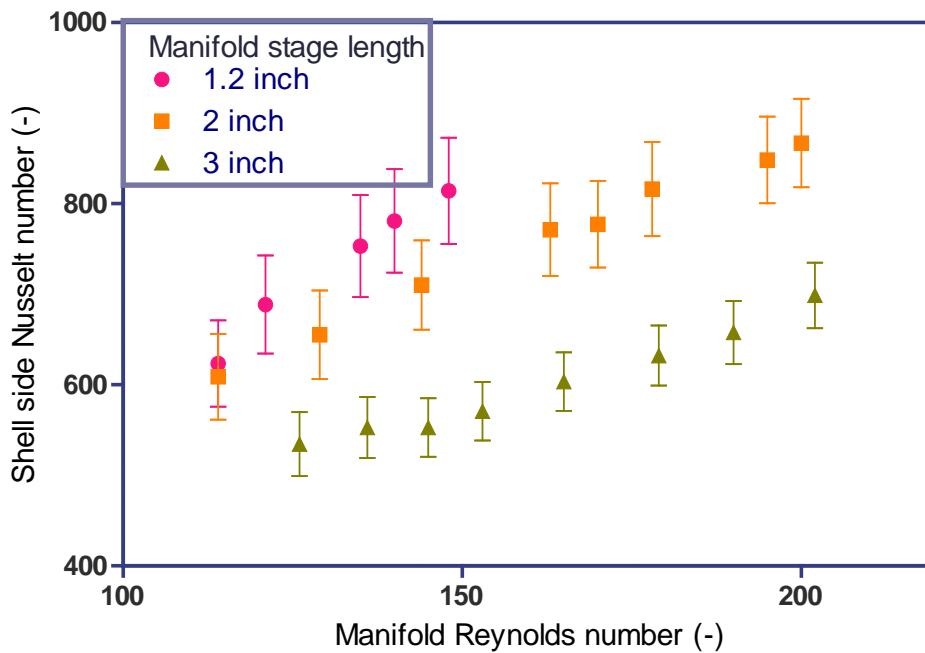


**Figure 5-4:** Variation of shell side Nusselt number (based on the OD of fin tube) with liquid Re inside the microchannels for three different manifold stage lengths

76
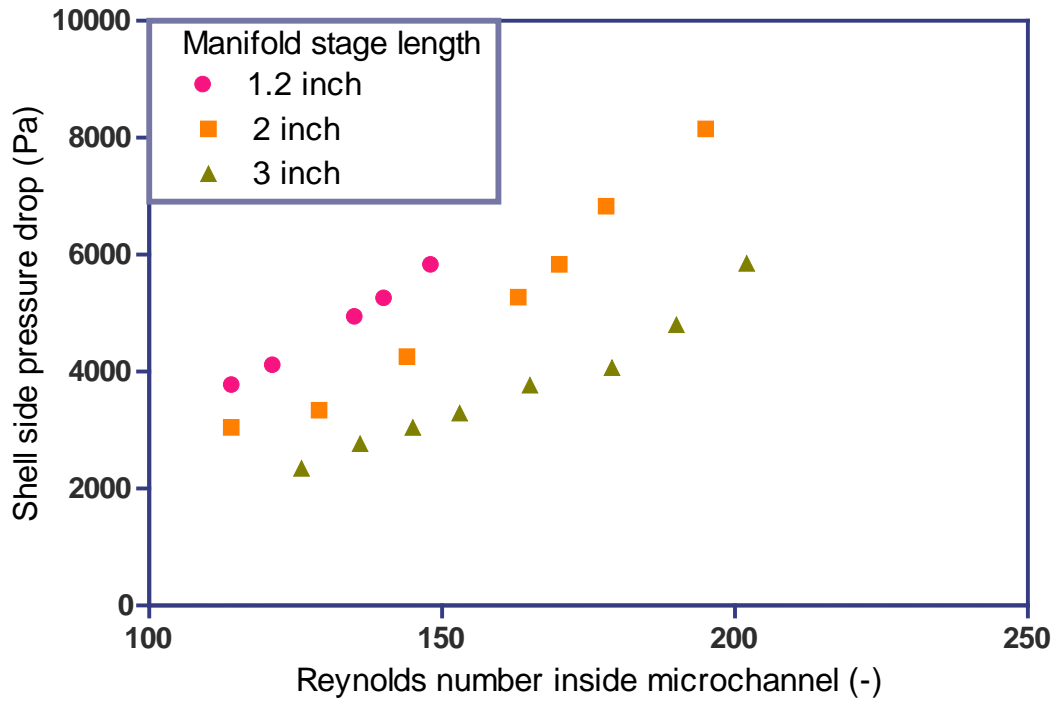
**Figure 5-5:** Comparison of shell side pressure drop for different manifold stage length
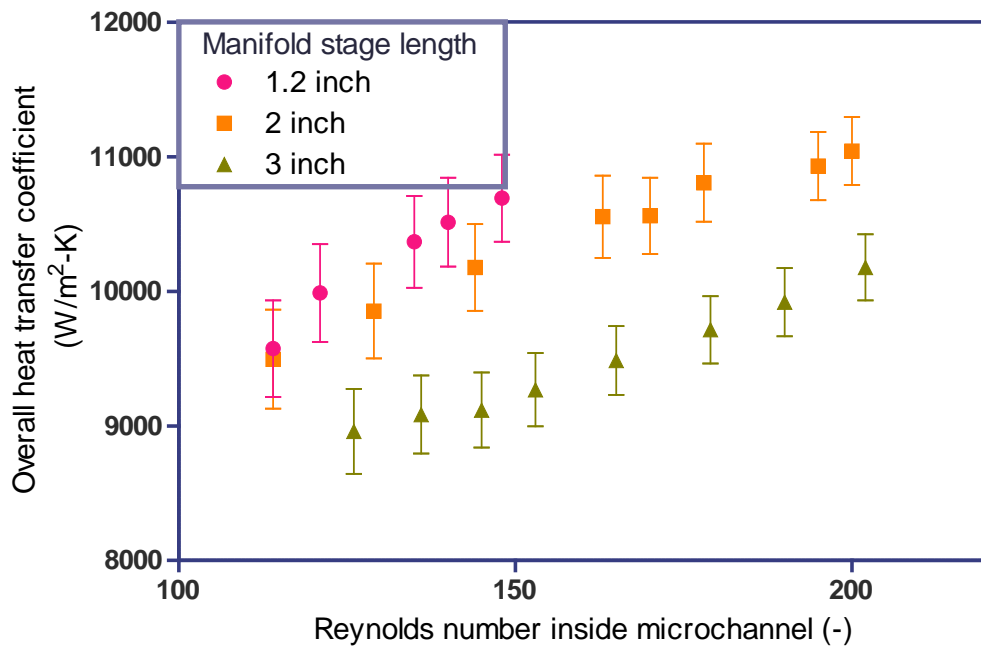


**Figure 5-6:** Effect of manifold stage length on the overall heat transfer coefficient
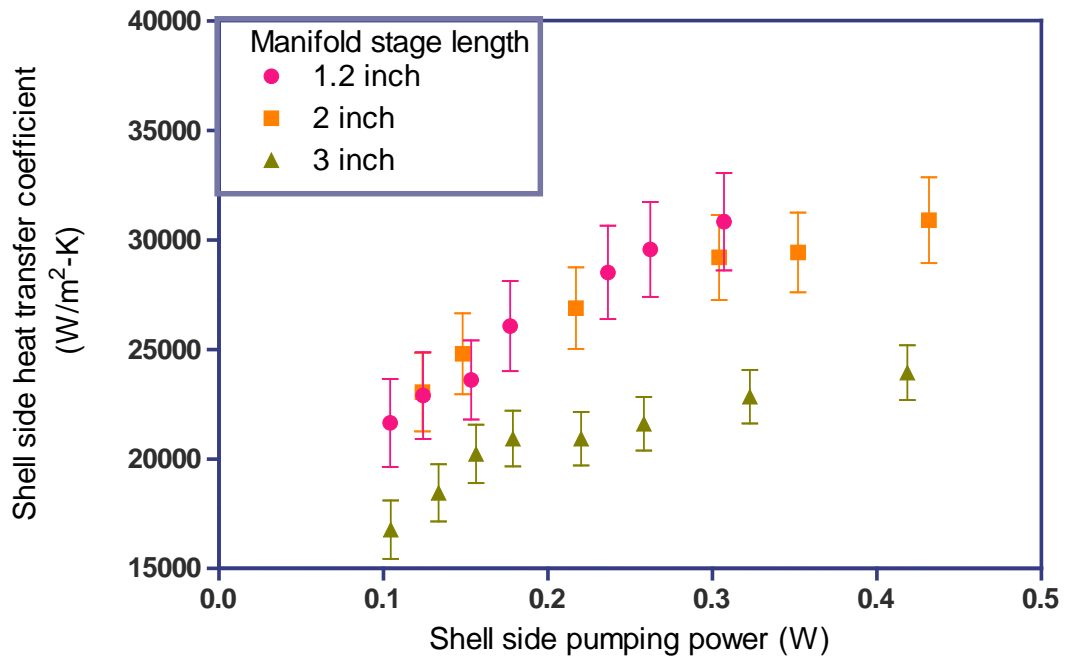
**Figure 5-7:** Effect of manifold stage length on the shell side heat transfer coefficient
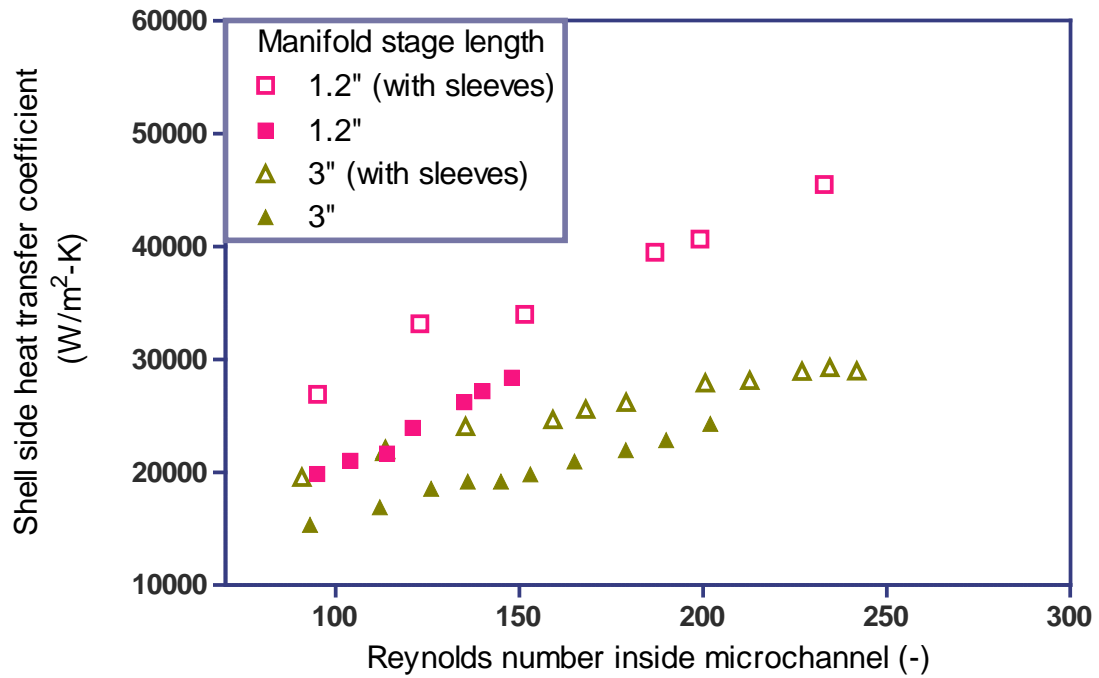


**Figure 5-8:** Effect of leakage on shell side heat transfer coefficient

### 5.4.2 Effect of flow leakage

Effect of flow leakage was studied by carrying out the experiment with the loose fit as well as tight fit manifolds by wrapping a plastic sleeve on the external surface of the manifold to avoid any leak through the gap between the manifold ribs and outer shell as discussed in flow visualization chapter. It was observed that the shell side heat transfer coefficient increased by 10-20% for the leak tight manifold (Figure 5-8). When the device is leak tight, otherwise leaking fluid is now forced into the microchannels which results in increase of mass flux (and hence the velocity) into the microchannels. The increase in the heat transfer is due to the increase of flow velocity in the microchannels as discussed in section 5.4.1.

Pressure drop of manifold with and without sleeves are given in the

Figure **5-9**. It should be noted that although there is no significant gain in the heat transfer in a leak tight device, there is substantial penalty on the pressure drop. This increase in the pressure drop is due to higher friction factor associated with the higher flow velocities in the microchannels, inlets and exits to the microchannels as well as inside the manifold plenum. When the plastic sheet is wrapped on the outer diameter of the manifold, the depth of the manifold plenum reduces by the thickness of the plastic sheet resulting in the volume reduction of the plenum. This causes the higher velocities and hence the higher pressure drop in the manifold plenum.

The graph of shell side heat transfer coefficient vs. pumping power shows that the heat transfer increased with the increase in the pumping power initially but the curve becomes asymptotic for higher pumping power numbers (Figure 5-10). Initial increase in the coefficient is related to the efficiency of the MMHX. For very low flow rates, the efficiency is almost 100% and the hot fluid outlet temperature becomes

almost equal to the inlet temperature of cold fluid. This results in almost no heat transfer in part of MMHX length. As the flow rate increases, this temperature difference increases and hence the heat transfer, resulting in rapid increase in heat transfer coefficient with increasing mass flow rate (and hence the pumping power). It was also noted that the pumping power to achieve the same heat transfer coefficient was almost similar for loose fit as well for the tight fit manifolds. Thus it was concluded that the flow leakage in the MMHX did not result in significant loss of heat transfer. For this reason, very tight fit of the manifold in the MMHX may be avoided to make the assembly/replacement of the manifold easier. This fact can be used to the advantage of the MMHX design as well. A typical heat exchanger has the heat capacities of the two fluid sides comparable. For this reason the flow rate in the single phase heat transfer experiments is comparable for both sides whereas the flow rate on the boiling or condensing side is much lower (due to high latent heat) to keep the balance in total heat transfer. Since the tube side flow rate is very high, MMHX is best suited for the use in boiling or condensation heat transfer on the microchannel side. It can be used for the single phase heat transfer applications if the flow rates on the two sides of the MMHX can be made comparable. The negligible effect of flow leakage on the heat transfer indicates that if the manifold can be designed in such a way that part of the fluid is bypassed without entering the microchannels, the pressure drop can be reduced significantly while maintaining the similar heat transfer coefficient. Typical issue with the microchannel heat exchangers is that due to very low flow rates in the microchannels, they achieve the high efficiency in a very short length of the heat exchanger. Thus scaling up for higher capacity may result in heat
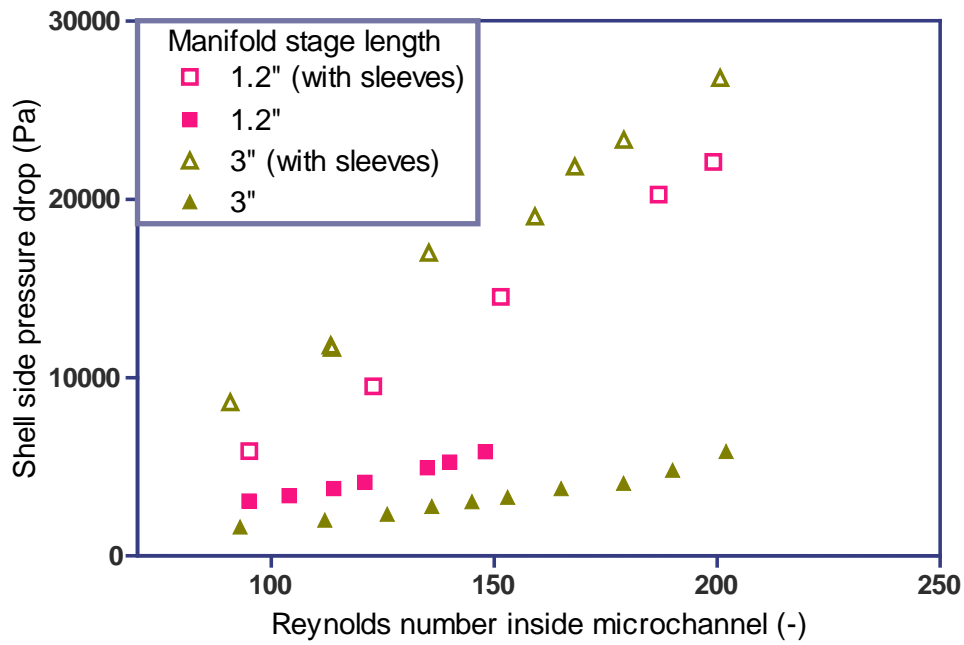
**Figure 5-9:** Effect of the leakage on the pressure drop in MMHX
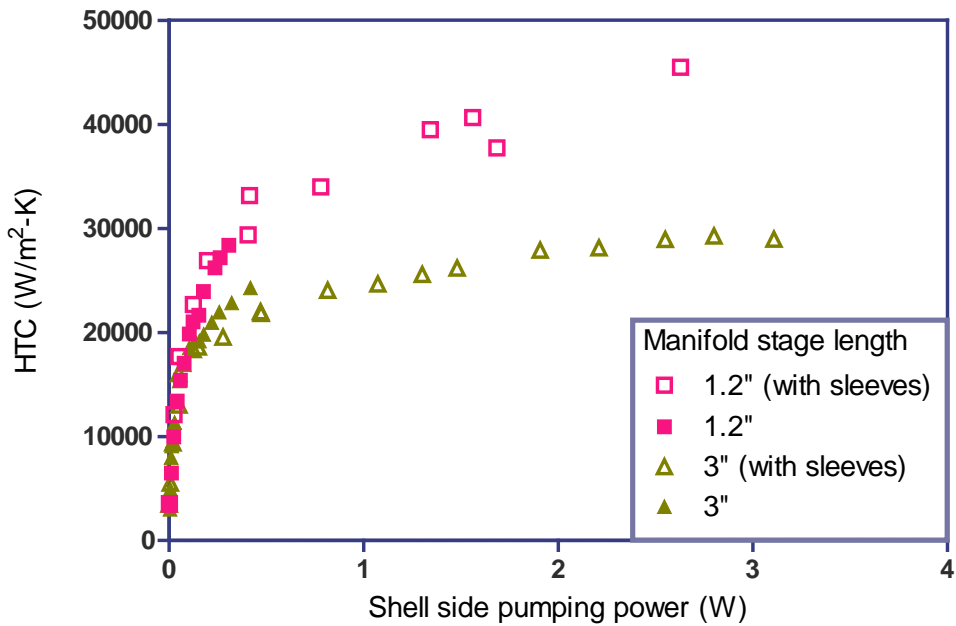


**Figure 5-10:** Comparison of different geometries with respect to the pumping power

exchangers which have one of their dimensions significantly larger than the other

dimension. This can be overcome in a MMHX design with bypass (flow leakage)

where the fluid coming out of a microchannel pass gets mixed with the bypass flow to reduce the efficiency of each stage and hence maintaining the higher LMTD and heat transfer. Proper use of liquid bypass can thus help designing the heat exchangers with any desired length without the concern of achieving high efficiency in the short microchannel lengths.

### 5.4.3 Comparison of MMHX with conventional double pipe heat exchangers

In order to compare the performance of MMHX with the conventional heat exchangers and the effect of manifold on the heat transfer, the following four different heat exchanger geometries were compared as discussed in experimental setup section:

1. MMHX-1 (Manifold:1.2 inch manifold stage length; Tube: Tube A (plain fin tube, 60 fin/inch)

2. MMHX-5 (Manifold:1.2 inch manifold stage length; Tube: Tube C (plain fin tube, 11 fin/inch)

3. MMHX-7 (Manifold: None; Tube: Tube A (plain fin tube, 60 fin/inch)

4. MMHX-8 or double pipe HX (Manifold: None; Tube: plain tube without any fins)

Figure 5-11 shows the shell side heat transfer coefficient comparison for these four test sections for varying shell side liquid mass flow rate. Shell side heat transfer coefficient in MMHX-1 is about an order of magnitude higher than that in double pipe MMHX-8 for the same liquid mass flow rate. Heat transfer coefficient in the MMHX is based on the base area of the tube and not fin surface. Higher heat transfer coefficient in MMHX is mainly due to the area enhancement of the tube. Also, due to

the smaller hydraulic diameter, the heat transfer coefficient for microchannels is higher than the larger channels for the same Nusselt numbers ($hD/k$) based on the channel diameter. A plot of Nusselt number based on the plain tube OD of double pipe as well as the fin tube OD for MMHX shows the similar trend (Figure 5-4). Comparison of MMHX-1 and MMHX-5 shows that the heat transfer for low fin density tube is lower than that for high density tube. This is again due to the two factors discussed above: 1) Area enhancement in the high fin density tube is higher and 2) Higher heat transfer coefficient in lower hydraulic diameter channels is higher for a fix Nusselt number.

Effect of the manifold was analyzed by studying the performance of MMHX with and without manifold for the same fin tube A. For no manifold case the heat transfer coefficient was almost equal to that of the plain tube MMHX-8. This indicates that although the same fin tube is used, there is no effect of the area enhancement on the heat transfer. This is due to the fact that the flow over the fin tube is parallel to the axis of the tube and hence the flow inside the fins becomes almost stagnant. This causes the heat transfer in MMHX-7 to be equal or even lower to that in the double pipe heat exchanger for given flow range. This scenario might change with the introduction of turbulence though which was not the interest of investigation for current study. Since the flow velocities in different test sections are different, pumping power has been used as a parameter for comparison rather than the pressure drop. It is clear from the Figure 5-13 that the overall heat transfer coefficient in the MMHX-1 is about an order or magnitude higher than that in MMHX-7 and MMHX-8 for the same pumping power requirement.
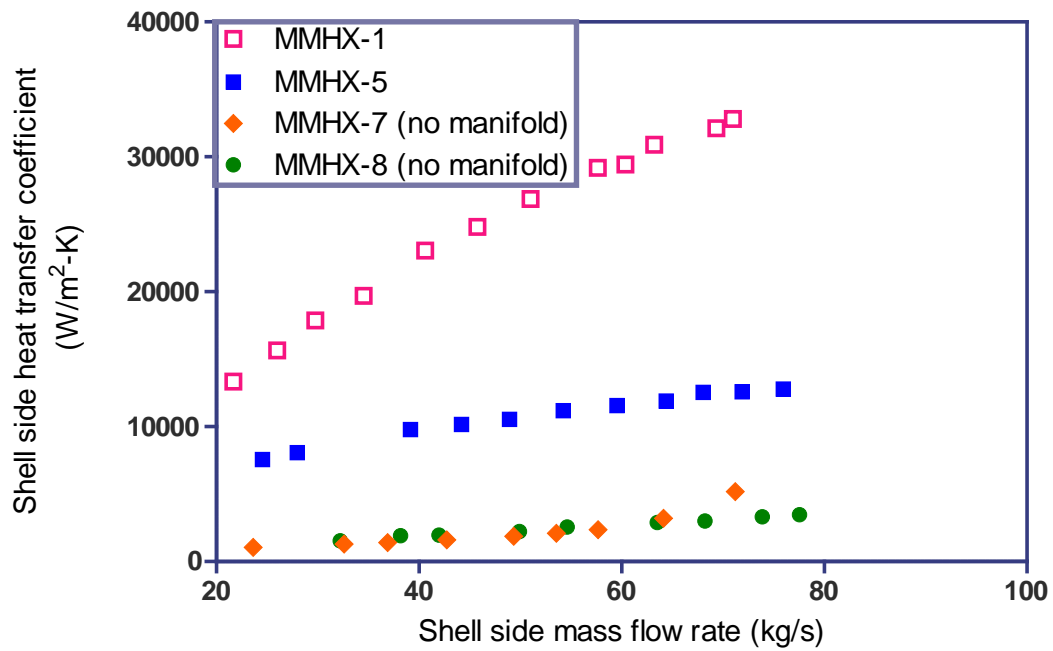
**Figure 5-11:** Comparison of heat transfer coefficient different heat exchanger geometries
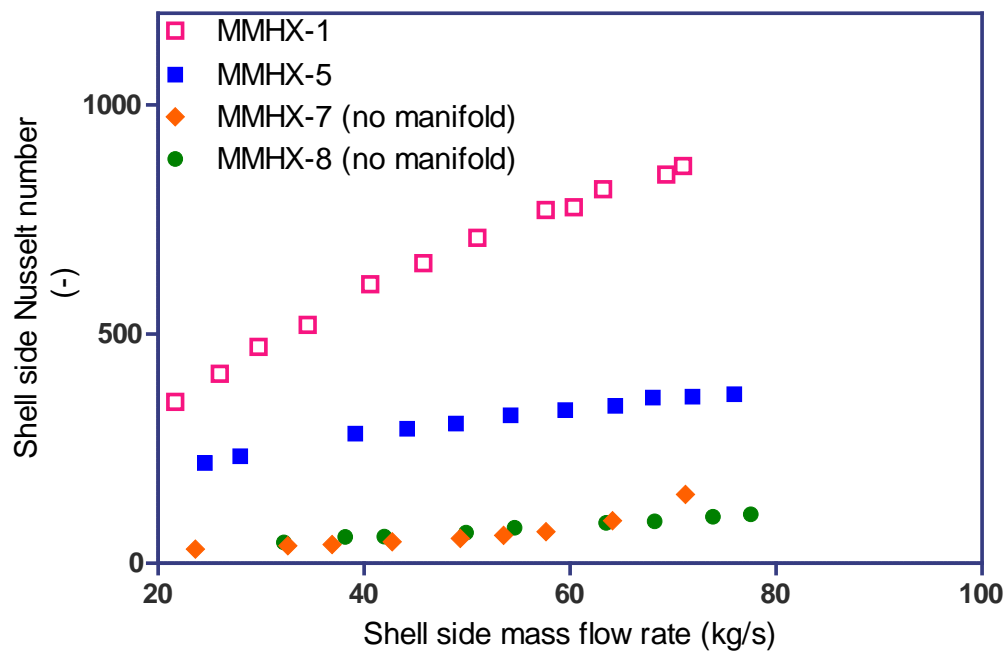


**Figure 5-12:** Comparison of Nusselt number (based on the fin tube diameter) for different heat exchanger geometries
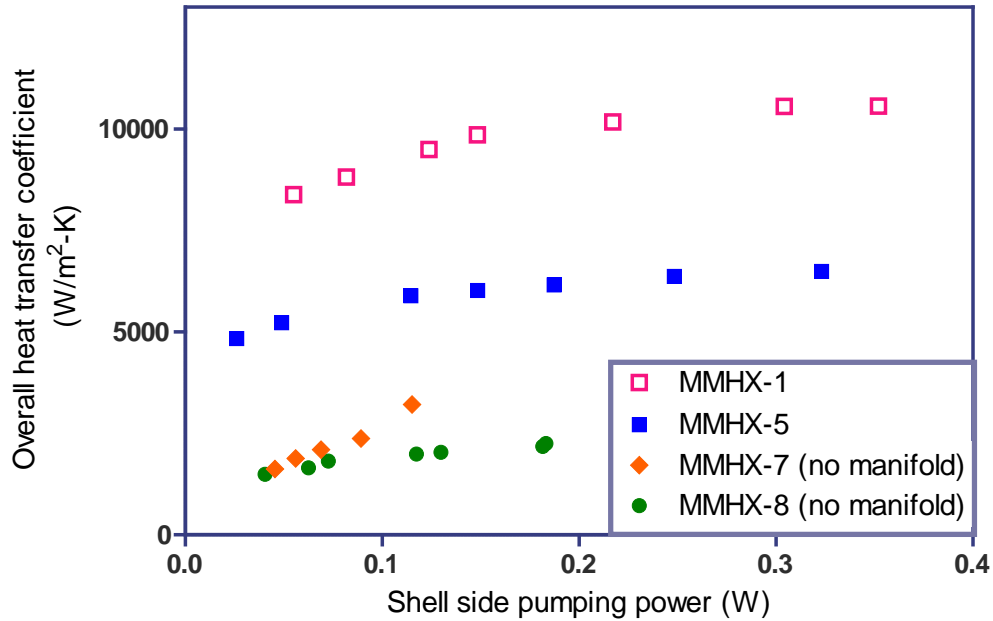
**Figure 5-13:** Comparison of overall heat transfer coefficient for different heat exchanger geometries

## 5.5 Comparison with the conventional heat exchangers

As shown in Table 5-3 Overall heat transfer coefficient in a typical shell and tube heat exchanger varies between 500-1200 $W/m^2$-K whereas the same for plate heat exchangers and spiral heat exchangers varies between 1000-4000 $W/m^2$-K and 700-2500 $W/m^2$-K respectively. From the results obtained from the experiments, it is clear that the heat transfer coefficients of 7000 to 11000 can be easily achieved using current MMHX design.

**Table 5-3:** Comparison of overall heat transfer coefficient of MMHX with conventional heat exchangers

| Heat exchanger type | Overall heat transfer coefficient ($W/m^2$-K) |
|---|---|
| Shell and tube heat exchanger | 500-1200 |
| Plate heat exchanger | 1000-4000 |
| Spiral heat exchanger | 700-2500 |
| MMHX | 7000-11000 |

## 5.6    Chapter conclusions

Single phase heat transfer and pressure drop was investigated in MMHX using water as the working fluid on both hot and cold sides. Effects of liquid flow rates, manifold size, and flow leakage on the heat transfer coefficient and pressure drops were studied in detail. Following conclusions were drawn from the single phase heat transfer study:

- Shell side heat transfer coefficient increased monotonically with the increase in manifold side liquid flow rate. However, the increase in heat transfer gets smaller at higher flow rates. Similarly, pressure drop was found to be monotonically increasing with increasing liquid flow rates.

- It was found that the shell side heat transfer coefficient increased with decreasing manifold stage length. This was due to the fact that reducing the stage length increased the mass flux and total flow length inside the microchannels causing increase in the heat transfer.

- Overall heat transfer in the MMHX was compared with that in double pipe heat exchanger. It was concluded that shell side heat transfer in the MMHX was almost an order of magnitude higher than the double pipe heat exchangers. HTC was plotted against the pumping power and the results show that there is significant improvement in HTC in MMHX-1 as compared to the double pipe geometry for the same pumping power.

- Pressure drop in the MMHX with shorter manifold stage lengths was found to be higher than that in longer stage length manifold. However, the differences were not significant. Pressure drop contribution from the manifold is typically low

(10% to 20% of the total) as compared to the overall pressure drop. However as the flow rate increases, the pressure drop in the manifold start becoming more significant.

# 6   Microchannel Evaporator

As discussed in the previous chapter, shell side heat transfer coefficient up to 45000 W/m$^2$-K can be achieved using single phase water experiments with MMHX. This chapter will discuss the utility of the MMHX for industrial evaporator applications. The experiments were carried out to evaluate the refrigerant side heat transfer and pressure drop for different MMHX designs using R134a refrigerant. The effect of the saturation pressure on the boiling heat transfer was also studied. These experiments were conducted for varying flow rates and saturation pressure. Two microchannel fin tube geometries were used in the study. It should also be noted that the terms 'evaporator' and 'MMHX' are used interchangeably in this chapter.

## 6.1   Introduction

Flow boiling inside the microchannels has been of great interest for electronics cooling in order to develop compact evaporators. This is mainly due to the fact that the flow boiling heat transfer coefficient is much higher than single phase heat transfer. Also the heat removal capacity for two phase is much higher due to the latent heat of vaporization.

Microchannel evaporation has been studied by several researchers using various fluids and microchannel geometries (Cetegen *et al.*; Kandlikar, 1990; Zhao *et al.*, 2000; Kandlikar, 2002b, a; Warrier *et al.*, 2002; Kandlikar & Steinke, 2003; Kandlikar, 2003; Qu & Mudawar, 2003; Yen *et al.*, 2003; Steinke & Kandlikar, 2004; Agostini *et al.*, 2008; Bertsch *et al.*, 2008; Grzybowski & Mosdorf, 2014). As discussed, most of these efforts were directed towards the high heat flux electronics

cooling applications. Lesser work has been reported for the evaporation in microchannels for industrial applications. Evaporators for the electronics applications are relatively small, resulting in shorter microchannel lengths. Scaling up of the microchannel evaporator presents the issues related to the longer microchannel lengths such as the two phase flow maldistribution, pressure instability and high pressure drops.

Current manifold microchannel heat exchanger design tries to address these issues. As shown in the flow visualization study, the manifold design helps in two phase flow distribution in the fin microchannels. Since the length of the flow inside the microchannels (pass length) is very small as compared to the manifold stage length, the flow instability problem can be reduced substantially. For the same reason, the pressure drop in the device can be kept much lower than the conventional parallel microchannel evaporators.

## 6.2  Selection of refrigerant

The experiments for evaporation were done using R134a as refrigerant. The refrigerant was chosen for various reasons.  R134a is a relatively higher pressure refrigerant commonly used in the refrigeration and auto industry. Since this work was part of an ammonia-water absorption refrigeration development project, it was an objective of this study to test the evaporator with Ammonia or similar refrigerant. Testing of MMHX with ammonia however was not possible due to hazardous nature which required a dedicated facility. Being a higher pressure system at room temperature, R134a simulates the conditions in the ammonia water absorption system.

However, Ammonia's latent heat is about six times higher and specific heat capacity about 2 times higher than that of R134a.

## 6.3 Experimental set-up and procedure

### 6.3.1 Experimental setup

MMHX-1 and MMHX-2 (as detailed in chapter 3) were investigated for the evaporator study. Figure 6-1 shows the experimental setup for the evaporator experiment. The refrigerant flowed into the evaporator in a close loop system as shown. A plate type condenser was connected into the loop to condense the refrigerant to make sure that the liquid refrigerant flowed inside the evaporator. Evaporator was kept in the vertical position during the experiment. Liquid refrigerant was fed to the bottom inlet of the evaporator with the help of a variable speed screw pump. Refrigerant vaporized inside the MMHX and flowed into the condenser before entering the pump.

There were two water loops which were connected to the MMHX and condenser. Hot water was circulated into the evaporator's tube side from a precisely temperature controlled Chiller (Neslab M72) and a heater of 3kW heating capacity. Cold side of the condenser (plate HX) was connected to another chiller (NESLAB HX150). Two thermocouples were connected at each inlet and outlet streams of the evaporator and condenser for temperature measurements. As discussed in the previous chapter, flow inside the MMHX tube was much higher in comparison to the flow in the shell side.
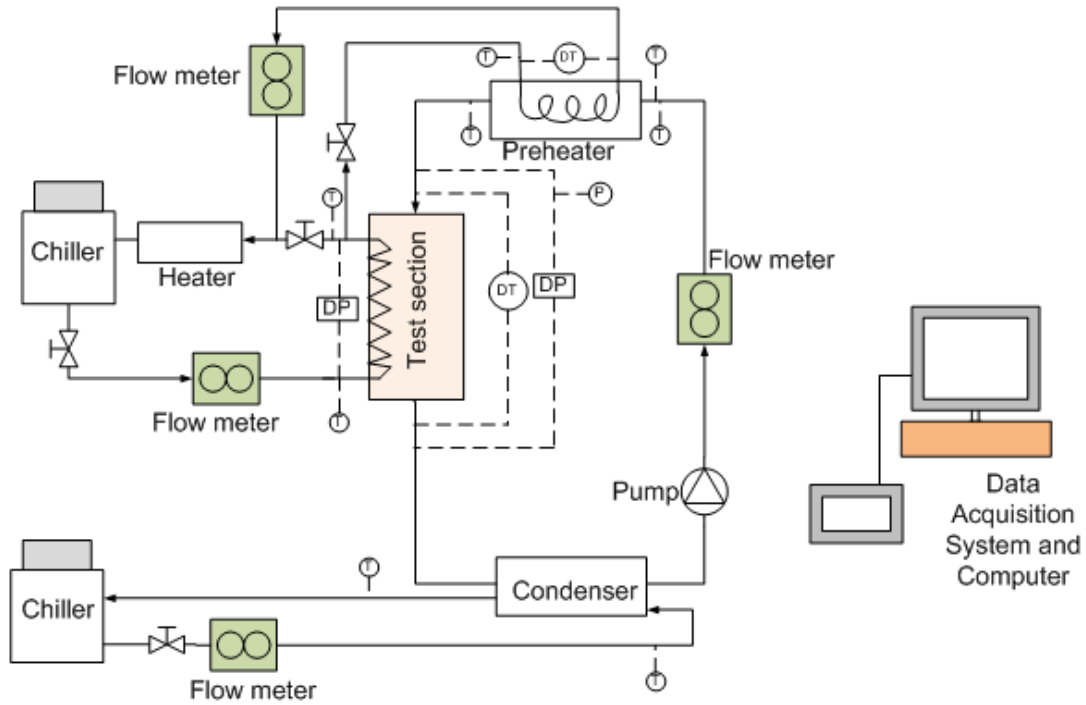
**Figure 6-1:** Schematic of the experimental setup

This caused very low temperature difference across the tube side which was not possible to measure accurately with the thermocouples. Thus to measure the temperature difference accurately, a differential thermopile was used. Similar to the single phase experiments, thermopile used in this evaporator had 4 and 6 thermocouples connected in series for shell side and tube side respectively.

Pressure difference across the inlet and outlet of evaporator´s refrigerant and water side is measured using differential pressure transducer (model Validyne-P55D). Refrigerant's absolute pressure at the inlet of the evaporator was measured with the help of an absolute pressure transducer (model: Setra 206). Refrigerant and water flow rates into the evaporator were measured using coriolis mass flow meters (models FCI and Endress Hausser 83F15 respectively) with accuracies of 0.1% of the flow.

Water flow rate into the plate condenser was measured using the magnetic flow meter integrated within the chiller itself.

All measurement data was recorded using an Agilent 36970A data acquisition system except the flow rate of the condenser chiller which was recorded manually. The steady state readings were used in the calculations. All the instruments along with their range and accuracies were given in the appendix A.

## 6.4 Experimental Procedure

### 6.4.1 Charging the system:

Upon completion of all the connections and leak tests, the system was put under vacuum using a vacuum pump to get rid of all the air from the loop. Then the system was charged with liquid refrigerant at room temperature. While charging the system, both the chillers were kept into the circulation to determine the exact amount of the charge needed to run the loop. To accomplish this, the refrigerant pump was kept running while the system was charged slowly until it became stable. Amount of charging was important as overcharging of the system leads to the flooding of the evaporator as well as the condenser and thus reducing the area for heat transfer. Undercharging the system leads to a low refrigerant level in the condenser resulting in vapor flow into the pump. It is desirable to charge the system in such a way that the plate heat exchanger (condenser) is about 20-30% filled with the liquid refrigerant (Jha, 2012). Experiments were performed by varying the following parameters:

1. Refrigerant flow rate

2. Hot water flow rate

3. Saturation pressure

4. Microchannel fin tube geometry

Refrigerant flow rate was varied while keeping the saturation pressure constant. The saturation pressure of the system was controlled by changing the mass flow rate into the condenser (PHX) as well as changing its inlet temperature. The above experiments were repeated for varying hot water flow rates into the evaporator. Effect of saturation pressure on the boiling was studied by changing the saturation pressure of the system from 8 bars to 10 bars while keeping the LMTD across evaporator constant. Saturation pressure was first reduced to the desired level and the evaporator inlet hot water temperature was changed to achieve the constant LMTD. Finally the water flow rate was varied from 0.05 kg/s to 0.41 kg/s to study its effect on the boiling heat transfer. The refrigerant flow rate, LMTD as well as saturation pressure were kept constant during these experiments. Similar experiments were repeated for two different microchannel tube types (smooth and enhanced fin microchannels tubes)

## 6.5 Data reduction and uncertainty analysis:

Evaporator duty $Q$ was calculated using the measured temperature difference between waterside inlet and outlet $T_{w,in}$ and $T_{w,out}$ respectively and water side mass flow rate $\dot{m}_w$ as:

$$Q = \dot{m}_w C_p \big( T_{w,out} - T_{w,in} \big) \tag{26}$$

Where Heat balance was checked at the superheated conditions and the error was within 7.5%. Majority of the error was due to the temperature difference

measurement on the water side. Overall heat transfer coefficient $U$ can be calculated

as

$$U = \frac{Q}{A \cdot LMTD}$$

(27)

**Table 6-1**: Parameters and range of experiments

| Parameters | Range |
|---|---|
| Refrigerant mass flow rate (g/s) | 10-60 |
| Tube side water mass flow rate (kg/s) | 0.15 -0.65 |
| Saturation pressure (bar) | 7.0-10.0 |
| Evaporator water temperature ($^\circ$C) | 25-35 |
| Condenser water inlet temperature ($^\circ$C) | 5-15 |
| Microchannel tube fin density (fin/in) | 60 and 43 |
| Fin type | Plain and enhanced fin |

Where LMTD is logarithmic mean temperature difference and is defined in terms of

water inlet and outlet temperatures and the saturation temperature of the refrigerant

$T_{sat}$ as

$$LMTD = \frac{\left(T_{w,in} - T_{sat}\right) - \left(T_{w,out} - T_{sat}\right)}{ln\frac{(T_{w,in} - T_{sat})}{(T_{w,out} - T_{sat})}}$$

(28)

Heat transfer coefficients are calculated based on the base area of the

microchannel tube. Water side heat transfer coefficient $h_i$ is calculated by the

correlation provided by the fin tube manufacturer as described in previous chapter.

Refrigerant side heat transfer coefficient $h_o$ can be obtained by the following

equation

$$\frac{1}{UA} = \frac{1}{h_i A_i} + \frac{ln\left(\frac{D_o}{D_i}\right)}{2\pi k l} + \frac{1}{h_o A_o} \qquad (29)$$

Where, $k$ is thermal conductivity of the tube material, $l$ is the length of the MMHX and $D_o$ is the outside diameter of the fin tube as shown in Figure 3-5. Heat transfer surface area for the inner and outer surfaces can be calculated as follows:

$$A_i = \pi D_i l \qquad (30)$$

$$A_o = \pi D_o l \qquad (31)$$

Reynolds number and mass flux into the microchannels are defined in the previous chapter (Section 5.3.2).

### 6.5.1 Uncertainty analysis

Uncertainty analysis was performed using law of propagation of uncertainty as described in the previous chapter. Estimated uncertainties for different measurements and calculations are presented in Table 6-2.

**Table 6-2:** Parameters and estimated uncertainties

| Parameters | Uncertainty |
|---|---|
| Temperature ($^\circ$C) | ±0.1 $^\circ$C |
| Water mass flow rate | ±0.1% |
| Refrigerant mass flow rate | ±0.1% |
| Log mean temperature difference | ±3.3% |
| Heat duty | ±6.3% |
| Overall heat transfer coefficient | ±8.1% |
| Refrigerant side heat transfer coefficient | ±9.4% |
| Vapor quality | ±5.9% |
| Pressure drop | ±0.25% |
| Absolute pressure | ±0.2% |

## 6.6   Results

### 6.6.1   Effect of refrigerant mass flux and heat flux

#### *6.6.1.1   Heat transfer*

Figure 6-2 shows shell side (refrigerant side) heat transfer coefficient based on the base area of the fin tube finished OD vs. refrigerant mass flux inside the microchannel with varying hot water flow rates. Heat transfer coefficient increases with the increase in refrigerant mass flux for a fixed hot water flow rate. To understand this behavior, understanding of boiling in microchannels is needed. The bubble growth phenomenon in the microchannels is similar to that in the pool boiling. However, the flow boiling in the microchannels is different in a way that the bubbles detach from the surface due to the flow and create bubbly flow. Also, due to high area to volume ratio, the liquid is quickly superheated which enhances the bubble growth after the nucleation process. To propose a comprehensive analytical model for the heat transfer inside the microchannels is difficult due to the complex nature of flow boiling inside the microchannels which includes the nucleation of bubbles, liquid-vapor interaction, presence of bubbles in the evaporating thin films, etc (Kandalikar et al.; 2005). The flow pattern of boiling in a microchannel has been discussed in chapter 2. As discussed in the section 2.4, experimental data in the literature show that the boiling heat transfer coefficient reduces with the increase in the vapor quality (Kandlikar *et al.*, 2005), which confirms the dominance of the nucleate boiling mechanism.

Increase in the refrigerant flow rate results in lower vapor fraction and hence the higher heat transfer coefficient.  Higher vapor fraction for the lower liquid flow

rates causes the partial dry out regions resulting in lower heat transfer. Base area shell side heat transfer coefficient varied from 20,000 to 45,000 W/m$^2$-K which is an order of magnitude higher than the conventional industrial evaporators. Refrigerant mass flux presented here ranges between 150 to 380 kg/m$^2$-s. Lower mass flux cases were not presented as almost 100% heat exchanger efficiency was achieved in the heat exchanger for mass flux lower than 150 kg/m$^2$-s.

Figure 6-2 shows that shell side heat transfer coefficient on the refrigerant side decreases with the increase in cooling water flow rate. Hot water flow rate represents the amount of heat flux to the evaporator, with higher hot water flow rates corresponding to higher heat fluxes due to higher water side heat transfer coefficients. With the increase in the water flow rate, heat transfer to the refrigerant increases. Increase in heat transfer increases the amount of vaporization in turn and hence the vapor fraction. As discussed earlier, the higher vapor fraction results in lower heat transfer coefficient. Increase of the water side heat transfer coefficient obtained from the correlation provided by the manufacturer is presented in Figure 6-3. The correlation was also validated experimentally using Wilson plot.
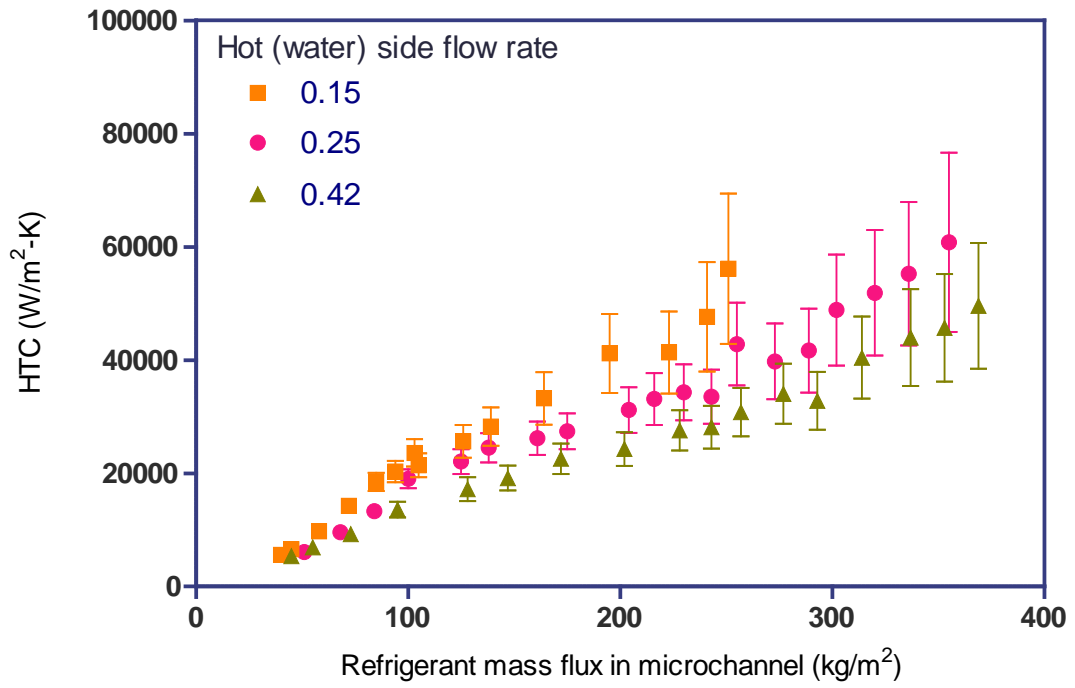
**Figure 6-2:** Effect of mass flux of refrigerant inside microchannels on heat transfer coefficient
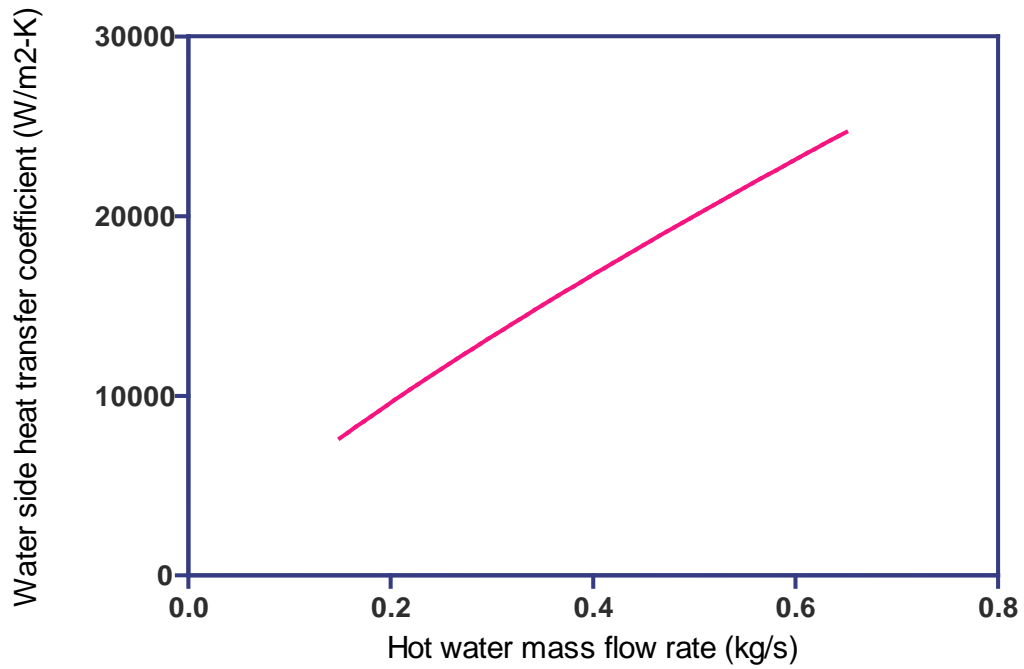


**Figure 6-3:** Tube side heat transfer coefficient vs. water flow rate

### 6.6.1.2 *Pressure drop*

As expected, refrigerant side pressure drop increases almost linearly as the flow rate increases (Figure 6-4). This is in line with the two phase pressure drop correlations proposed in the literature where the pressure drop is linearly proportional to the flow velocity (Steinke and Kandlikar; 2006). It was also noted that the hot water flow rate or increased heat flux did not have strong effect on shell side pressure drop. Experimental results presented in the literature have shown that the pressure drop is not a strong function of heat flux (Qu and Mudawar; 2003) or vapor quality (English and Kandlikar; 2006). This is in contrast with the flow boiling in the larger channels where the pressure drop increases rapidly with the heat flux. This is due to the difference between the flows in the micro and macro scale channels. Flow in the microchannels is typically combination of laminar liquid and laminar vapor while flow in larger channels is in the turbulent regime for both phases. Reynolds numbers in the current experiments were consistently lower than 100 for liquid and 600 for gas and hence the flow is always laminar for both the liquid and gas.

Waterside pressure drop is shown in the Figure 6-5 and was compared to the correlation provided by the microchannel tube manufacturer. As shown, the experimental data matched very closely with the correlations however; the experimental pressure drop was a bit higher than that from the correlation. This was due to the fact that the experimental pressure drop also included the fluid entry and exit losses as the pressure differential probes were connected before inlet and after the exit.
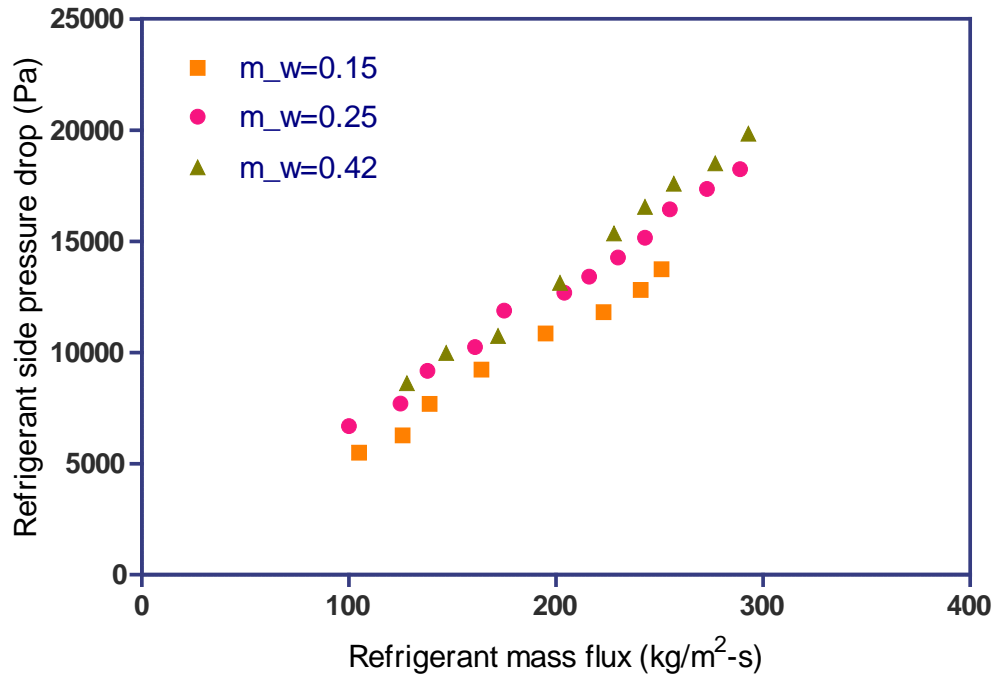
**Figure 6-4:** Refrigerant side pressure drop vs. mass flux of refrigerant for different tube side water flow rates
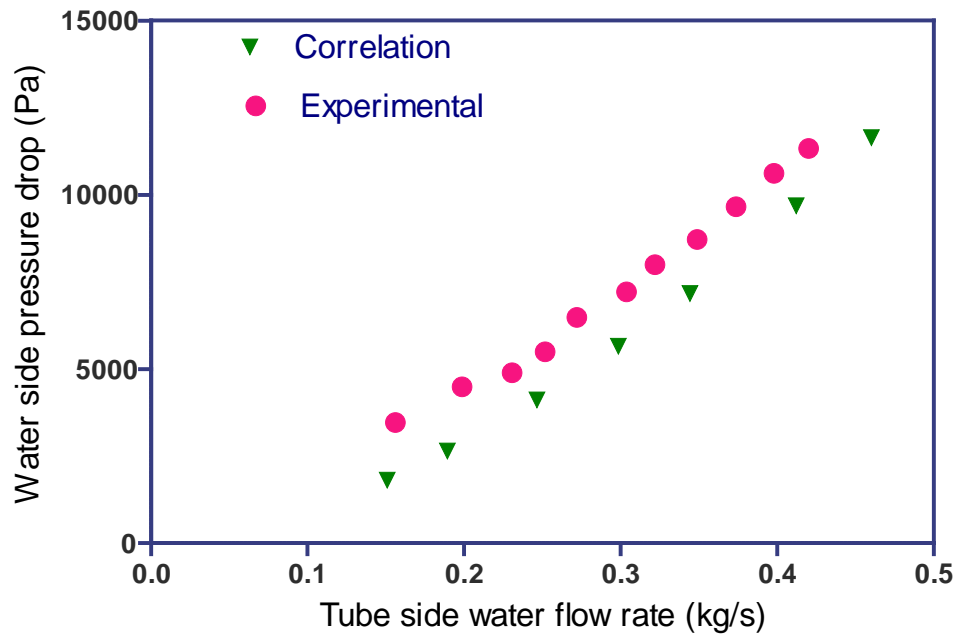


**Figure 6-5:** Water side (tube side) pressure drop vs. water flow rate

### 6.6.2    Effect of fin enhancement on the boiling heat transfer

Several methods of tube fin enhancements have been used in the industry to improve the boiling heat transfer. Since most of these designs are proprietary, different fin tube manufacturers use different enhancement methods such as fins with internal ribs, fin with wavy structures, fins with cross cut etc. To evaluate the effect of the fin enhancement comparison of performance of the MMHX with enhanced fin tube (MMHX-2) was made with plain fin tube (MMHX-1). Shell side heat transfer coefficient is plotted against the refrigerant mass flow rate for the two fin tubes (Figure 6-6). The mass flow rate instead of mass flux was chosen this case because the exact cross sectional area for the flow could not be determined due to the complex geometry of fins of the enhanced fin tube. Water side flow rate and saturation pressure are kept constant at 0.42 kg/s and 7.0 bars respectively. The shell side heat transfer coefficient for the plain tube is almost 40 to 50% higher than of the enhanced fin tube. Higher boiling heat transfer for the smooth fin tube was due to the two apparent reasons. First, the surface enhancement ratio for smooth fin tube was 36.7% higher than that in the enhanced fin tube. Since the heat transfer coefficient is calculated based on the base area of the fin tube (outer perimeter of the tube), any enhancement in the area results in the enhancement in the heat transfer coefficient because the surface area enhancement is integrated into the shell side heat transfer coefficient. It was also noticed that the enhanced tube was not as tight fit with the manifold as smooth fin tube. Thus some fluid leakage was expected between the tube OD and manifold internal diameter of the enhanced tube. These two factors are believed to be the reason for lower heat transfer coefficient for the enhanced fin tube.

Pressure drop in the smooth tube is plotted against the enhanced fin tube (Figure 6-7). Pressure drop increases linearly with the refrigerant mass flux for both tubes. As discussed in previous section, this behavior is due to laminar nature of flow for both the vapor and liquid. The Pressure drop in the smooth fin tube was found to be slightly higher than that in the enhanced fin tube. It should be noted that the fins in the enhanced fin tube are more irregular and hence should have caused higher pressure drop. However, due to the leak of the refrigerant through the gap between the tube OD and manifold ID of the enhanced fin tube MMHX, pressure drop for enhanced fin tube was lower.
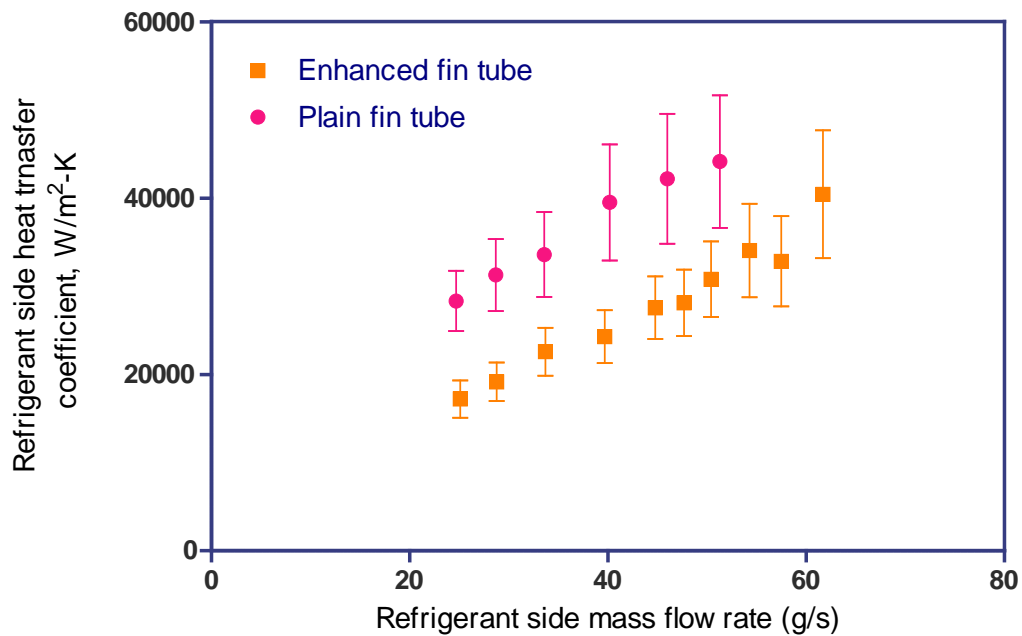


**Figure 6-6:** Comparison of refrigerant side heat transfer coefficient for two different tubes
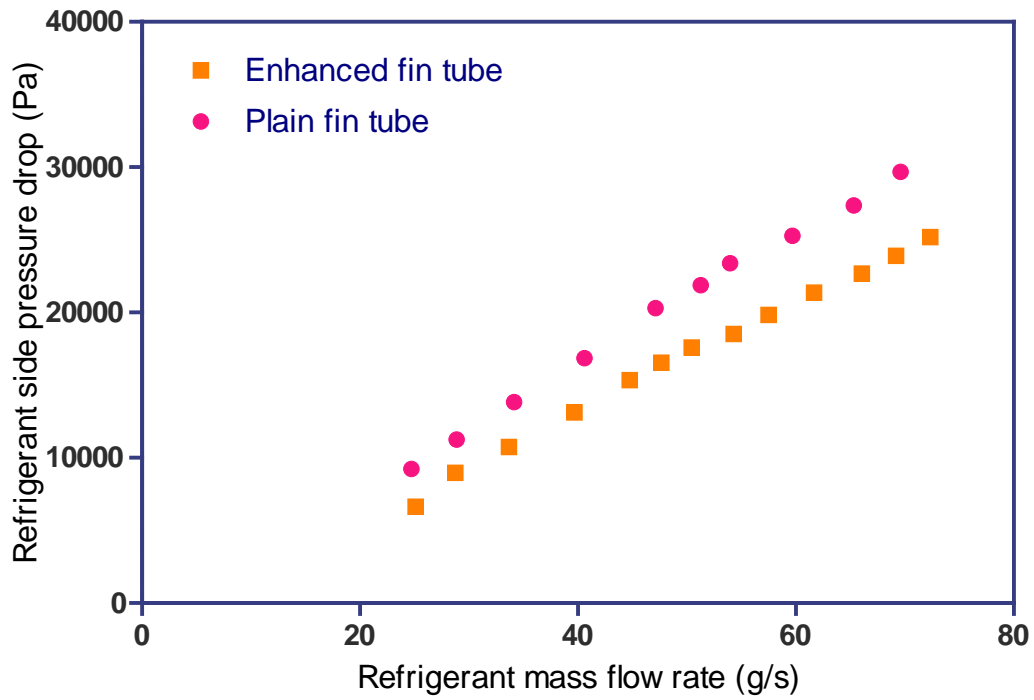
**Figure 6-7:** Comparison of refrigerant side pressure drop for two different tubes
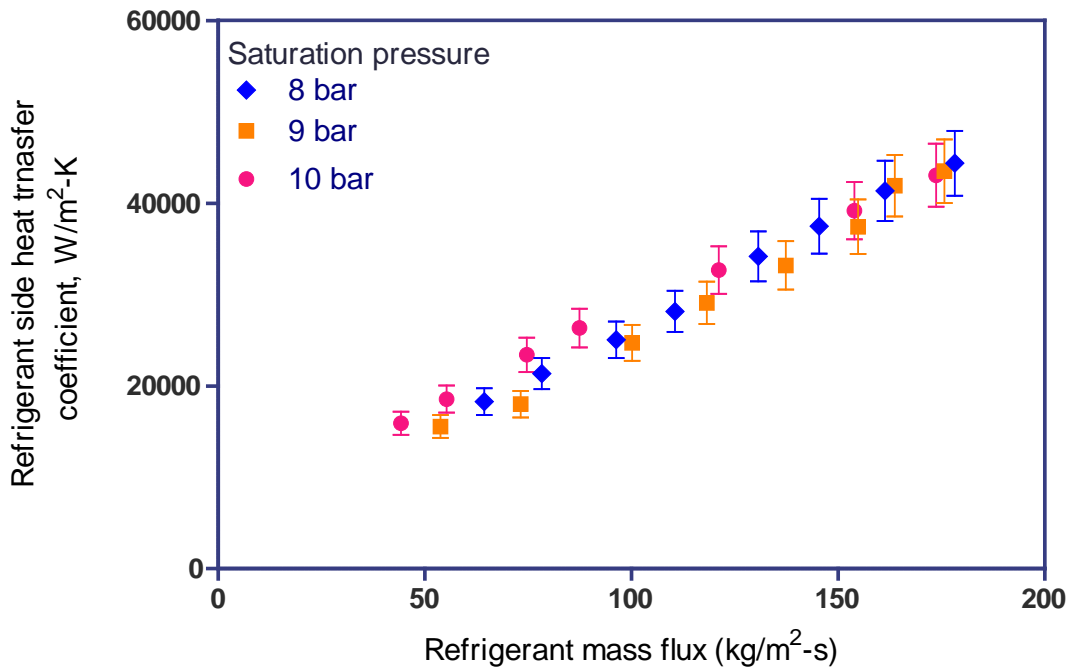


**Figure 6-8:** Effect of saturation pressure on refrigerant side heat transfer coefficient
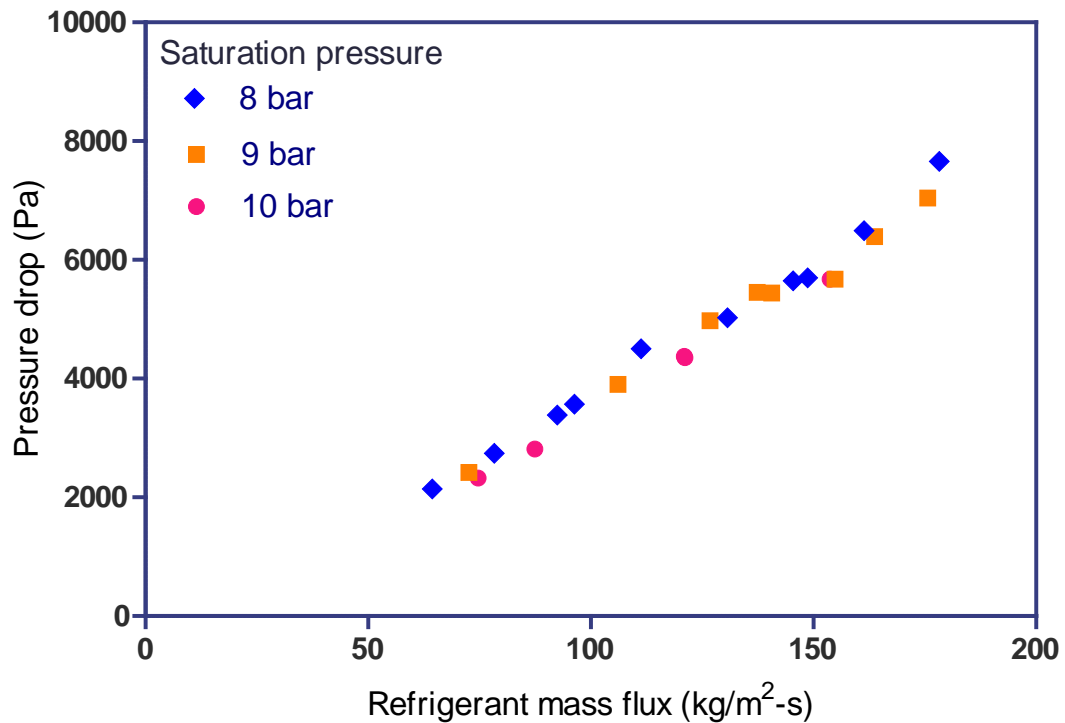
**Figure 6-9:** Effect of saturation pressure on refrigerant side pressure drop

### 6.6.3 Effect of saturation pressure on heat transfer and pressure drop

Saturation pressure of the system is dependent upon several factors such as water side flow rate, inlet temperature of hot water, as well as the temperature of the condenser, etc. Thus it is a challenging task to keep the saturation pressure constant for the experiments with varying parameters. For example; as the water side flow rate into the evaporator is increased, the saturation pressure of the system starts to increase and has to be brought down by other means such as reducing the condenser temperature. This has to be done for each data point recorded. However, due to the time constraint as well as the constraint with the chiller flow rate for the condenser, a variation of $\pm 0.2$ bars in the saturation pressure was accepted during the experiments. To evaluate the effect of this saturation pressure variation on the heat transfer coefficient and pressure drop, experiments were performed for three different

saturation pressures 8 bar, 9 bar and 10 bar while keeping the LMTD constant. From Figure 6-8 it is clear that the measurements of heat transfer coefficient could not be distinguished within the measured uncertainty. Similar results were reported by other authors (Wellsandt & Vamling, 2003; Saitoh et al., 2005; Bertsch et. al, 2009 ) where there was no definite distinction for the effect of saturation pressure on the heat transfer coefficient. It was found that the effect of saturation pressure on shell side pressure drop was not clearly distinguishable either (Figure 6-9). Increase in saturation pressure affects the flow pattern in a way that the volume of vapor and hence the quality reduce. However, this reduction in the vapor quality is marginal for the saturation pressures range investigated. Also, as discussed in section 6.6.1.2 the dependence of pressure drop on vapor quality is not significant.

## 6.7 Chapter conclusions

Experiments with two different types of microchannel evaporators were performed and compared with each other. Overall heat transfer coefficient during the evaporation was about an order of magnitude higher than those obtained in conventional evaporators such as shell and tube or plate type heat exchangers. Following were conclusions of the evaporator experiments:

1. MMHX was used in the evaporation mode by using R134a refrigerant at its saturation pressure of close to 7 bars. It was found that the shell side heat transfer performance of the MMHX was an order of magnitude higher than that of the conventional evaporators. Heat transfer coefficient increased monotonically with the increase in refrigerant mass flux. Base heat transfer coefficient was found to be as high as 45,000 W/m$^2$-K on the shell side.

2. Total amount of refrigerant charge in the MMHX was substantially lower (90 grams) as compared to 1000 grams for conventional plate type evaporators. Thus MMHX can reduce the use of greenhouse gases substantially. This will also lower the safety hazard for toxic refrigerants such as NH3 which is major refrigerant used in the industrial applications.

3. Comparison of the shell side heat transfer coefficient for two fin tube geometries, plain fin and enhanced fin showed 30-40% higher HTC for plain fin tube (MMHX-1). Major reason for this enhancement was due the higher surface enhancement in the smooth fin tube as the fin density in smooth fin tube was higher. Pressure drop in the smooth fin was 15-20% higher than the enhanced fin tube.

4. Experiments with varying the saturation pressure showed that the heat transfer coefficient did not vary much with saturation pressure.

# 7  Microchannel condenser experiments

## 7.1  Introduction

Single phase and two phase boiling heat transfer experiments presented in previous two chapters showed that the substantial enhancement in the heat transfer is possible in the MMHX. Condensing heat transfer is another area of interest for heat transfer equipments. It is one of the components in the absorption refrigeration as well as $CO_2$ separation units being studied at the $S^2TS$ Lab at University of Maryland. Due to these reasons, it was decided to evaluate the condensing heat transfer performance in the MMHX. This will enable us to design the condenser for the waste heat recovery system as well as for the $CO_2$ absorption systems.

Microchannel based condensers are being used in the refrigeration and automotive systems. As shown in the Figure 7-1, extruded aluminum microchannel arrays are manufactured to fabricate light weight and compact heat exchangers. Relatively lower number of researchers have looked into the condensation mass transfer in the microchannels (Chen & Cheng, 2005; Wang & Rose, 2005; Wu & Cheng, 2005; Bandhauer *et al.*, 2006) as compared to the evaporation in microchannels. Maldistribution, flow fluctuation and instability are concerns in two phase flow in the microchannels. Condensation in the microchannels is prone to relatively lower flow instabilities (Wu & Cheng, 2005).

MMHX design can be useful to minimize the issues of maldistribution, flow fluctuation and instabilities due to its short microchannel pass length. Optimum

design of a condenser should have varying cross section flow area along the length of the heat exchanger. A constant flow area will result in excessive velocities at the inlet for the condenser, causing high inlet pressure drop and hence the reduction in saturation pressure and thus reduction of temperature difference for heat transfer. Such design can easily be achieved in the MMHX simply by using the variable stage length manifolds. This chapter discusses the experimental investigation of condensation heat transfer in MMHX using R134a as refrigerant and water as cooling medium. Experiments were performed at the condensing temperature close to 35 $^\circ$C which is typical saturation in the condensers.
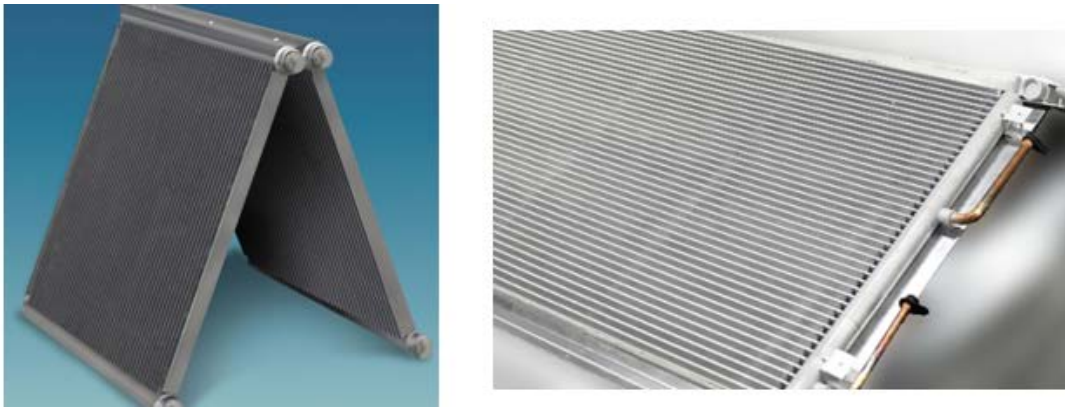


**Figure 7-1:** Extruded aluminum microchannel condensers
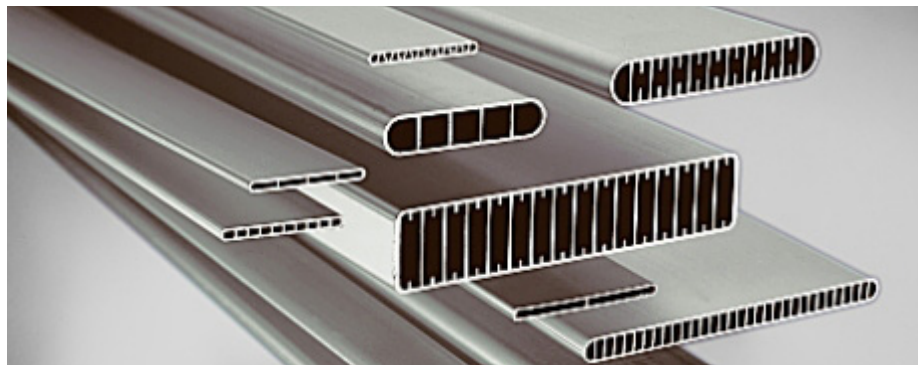


**Figure 7-2:** Extruded aluminum microchannels studied by several researchers (Yang & Webb, 1996a; Webb & Ermis, 2001; Agarwal *et al.*, 2010; Sakamatapan & Wongwises, 2014)

## 7.2 Experimental set-up and procedure

Experiments were carried out using the geometry MMHX-1 having smooth fin tube 'A' and manifold stage length of 1.2 inch as discussed in the chapter 3. The experimental setup was a close loop system having a refrigerant loop consisting the evaporator and MMXH as condenser. Two different water loops were used to provide the heating to the evaporator and cooling to the condenser.

### 7.2.1 Refrigerant loop

Figure 7-3 shows the schematic diagram of the condenser experimental set-up. Single phase vapor refrigerant coming out of the plate type evaporator entered the condenser where it was condensed by the cooling water flowing inside the microchannel tube. The refrigerant was pumped out of condenser and was fed back to the evaporator using a variable speed gear pump (Idec GD-M35). Liquid flow rate was measured using a coriolis flow meter (Model E+H 83A02). Evaporator was heated by the hot water coming from a 3.0 kW heater. A chiller (model NESLAB M72) was added to this water loop. The chiller's water bath was utilized as a thermal mass which helped maintaining a nearly constant temperature in the loop.

The evaporator was kept in the vertical orientation to make sure that only the superheated vapor leaves the evaporator. Appropriate amount of refrigerant charge in the system is important in order to maintain a certain refrigerant level in the evaporator. Overcharging the evaporator will result in the liquid entrainment while undercharging will not provide enough heat transfer.

Cooling water is circulated into the condenser from a high capacity Neslab chiller (model HX500) at the set temperature and flow rate. Waterside flow rate was varied using the flow regulating valves. A coriolis flow meter was installed in the loop to measure the mass flow rate of cooling water into the condenser.
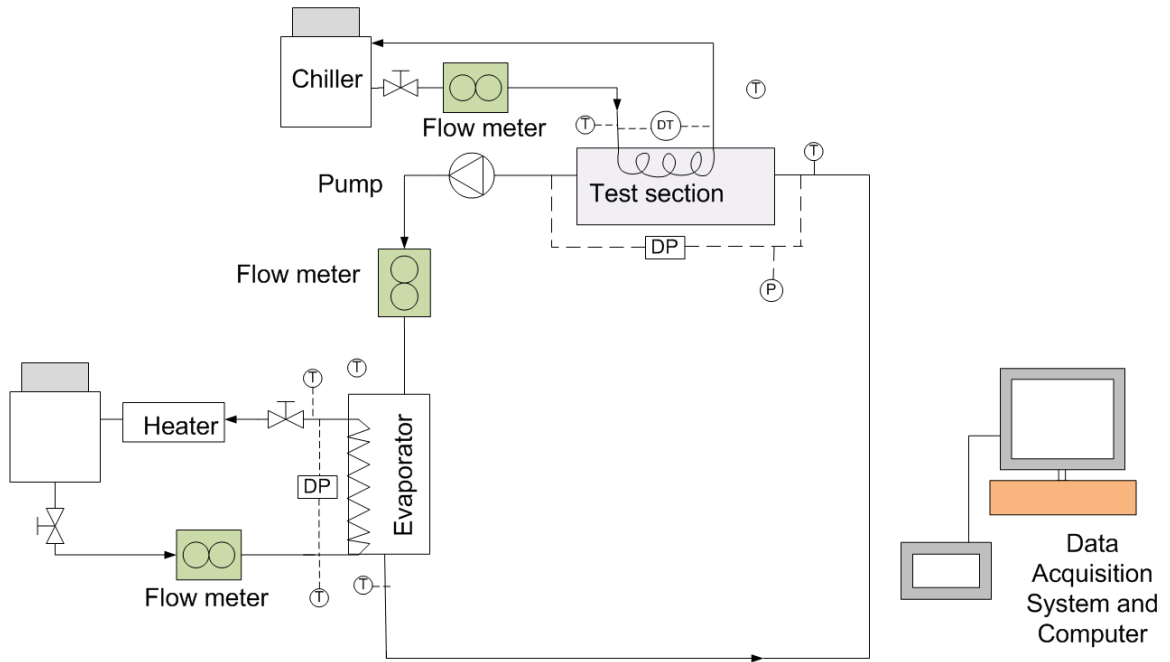


**Figure 7-3:** Experimental setup schematic
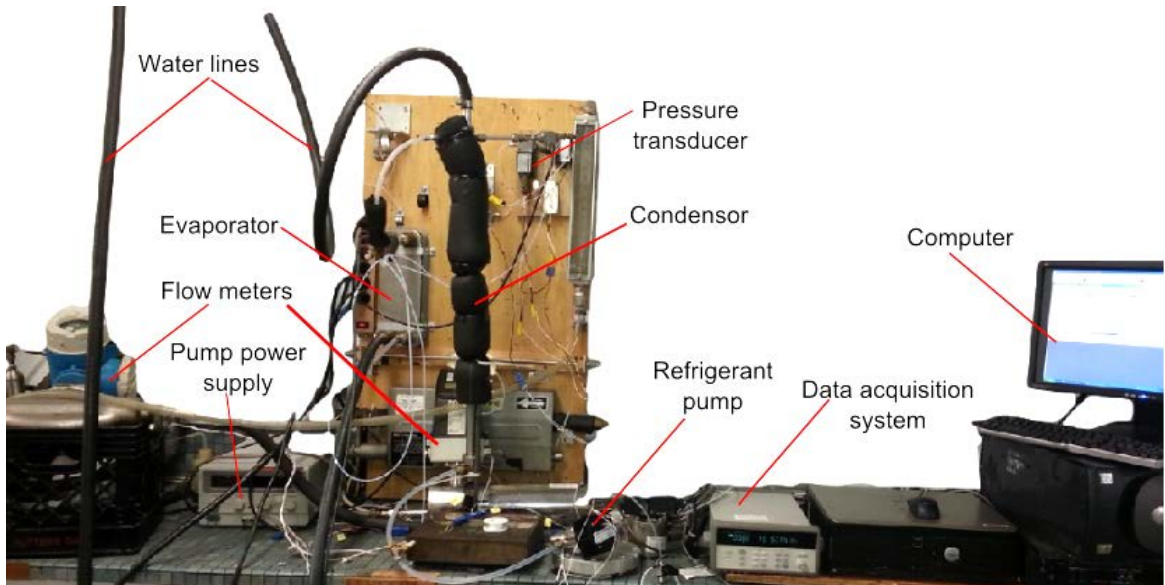


**Figure 7-4:** Photograph of condenser experiments

### 7.2.2 Charging of the refrigerant

Similar to the evaporator setup, the condenser refrigerant loop was charged in steps while keeping both the refrigerant and water loops running. Running the flow loops helps charging the system as the cold water flow in the condenser brings down the refrigerant pressure in the loop. Also, the adequate amount of refrigerant charge can be easily determined while the loop is running.

### 7.2.3 Experimental procedure

Although the pump was able to handle two phase flow, flow rates more than 33 g/s could not be achieved. Due to the capacity of the plate heat exchanger evaporator, there was a limitation on the maximum flow rate that could be achieved during the experiments. However, this flow rate is more than 20 g/s flow expected in the Ammonia absorption system of the similar capacity.

Once the system was properly charged, cooling water to the condenser was set to the desired temperature. Refrigerant inlet flow rate into the condenser can be controlled by the evaporator heat input. As the refrigerant flow rate to the condenser was increased, the system pressure started to fall due to the excess refrigerant cooling. In order to run the experiments at constant saturation pressure, evaporator water inlet temperature and flow rates were adjusted.

Refrigerant mass flux to the condenser was varied from 7 g/s to 33 g/s. Cooling water flow rate to the condenser was kept constant at its maximum of 0.65 kg/s to minimize the water side thermal resistance. Saturation pressure of the system was maintained at 9 bars. Corresponding saturation temperature is close to 35.5 $^{\circ}$C

which is typical for an air cooled condenser. Cooling water inlet temperature into the MMHX was kept close to the room temperature. Inlet water temperature into the evaporator was varied between 36 $^{\circ}$C to 42 $^{\circ}$C to control the amount of refrigerant evaporated. The vapor coming out of the evaporator was superheated and was up to 2 $^{\circ}$C higher than the saturation temperature. Ideally a pre-cooler is needed to make sure that the vapor entering into the condenser is saturated. However, since the refrigerant's specific heat capacity (~1.1 kJ/kg-K) is substantially lower than the latent heat of the condensation (~167.2 kJ/kg), sensible heat gain due to this superheat can be neglected. Due to this reason, no pre-cooler was installed between the evaporator and condenser.

## 7.3 Data acquisition and uncertainty

Similar to the previous experiments, temperature difference of the water in the two heat exchangers was measured with the help of two thermopiles. Refrigerant as well as water inlet and outlet temperatures at condenser and evaporator were measured using a pair of thermocouples at each location. Water and refrigerant side pressure drop across the condenser was measured using two differential pressure transducers (model Validyne P55D). Absolute pressure of the system is measured at the inlet of the evaporator with the help of a pressure transducer (model: Setra 206). Data was recorded by Agilent 36970A data acquisition system. The details of all the instruments used in the experiments are given in the appendix A.

Uncertainties in the experiments were calculated by the error propagation method described in the chapter 5. Major uncertainty in the heat transfer coefficient is related to the uncertainty in the measurement of the temperature difference of the

cooling water across the condenser. Table 7-1 shows the different measurement uncertainties.

**Table 7-1:** Parameters and estimated uncertainties

| Parameters | Uncertainty |
|---|---|
| Temperature ($^{\circ}$C) | ±0.1 |
| Water mass flow rate | ±0.1% |
| Refrigerant mass flow rate | ±0.1% |
| Log mean temperature difference | ±3.1% |
| Heat duty | ±7.4% |
| Overall heat transfer coefficient | ±9.3% |
| Refrigerant side heat transfer coefficient | ±10.7% |
| Pressure drop | ±0.25% |
| Absolute pressure | ±0.2% |

## 7.4  Data reduction

Total cooling heat duty can be calculated from the cooling water side mass flow rate and the temperature difference as follows:

$$Q = \dot{m}C_p\left(T_{w,out} - T_{w,in}\right) \tag{32}$$

Overall heat transfer coefficient based on the outer diameter of the tube is determined as

$$Q = UA_oLMTD \tag{33}$$

Heat transfer areas of the tube based on the inner and outer diameters are defined as

$$A_i = \pi D_i L \tag{34}$$

$$A_o = \pi D_o L \tag{35}$$

Since the refrigerant inside the MMHX is condensing, its temperature profile can be assumed as a constant line and equal to the saturation temperature. LMTD across the MMHX can be calculated as

$$LMTD = \frac{\left(T_{sat} - T_{w,out}\right) - \left(T_{sat} - T_{w,out}\right)}{LN \frac{\left(T_{sat} - T_{w,out}\right)}{\left(T_{sat} - T_{w,in}\right)}} \tag{36}$$

Similar to the single phase and evaporation experiments, water side heat transfer coefficient is then evaluated by the correlation provided by Wolverine Inc. Once the waterside heat transfer is known, refrigerant side heat transfer coefficient is evaluated as

$$\frac{1}{UA} = \frac{1}{h_i A_i} + \frac{ln\left(\frac{D_o}{D_i}\right)}{2\pi k l} + \frac{1}{h_o A_o} \tag{37}$$

## 7.5 Results and discussions

As discussed in chapter 2, condensation heat transfer inside the microchannels has not been investigated exhaustively in the literature. As opposite to the boiling heat transfer, condensation heat transfer did not have significant application in electronics cooling and hence the study on microchannel condensation is scarce. Most of the studies were performed in the channels larger than 1-3 mm diameters. Thus there is no definite general model for heat transfer and pressure drop is available in the literature.

Variation of shell side heat transfer coefficient with the refrigerant mass flux inside the microchannels is shown in the Figure 7-5 . Heat transfer coefficient increased with the increase in the mass flux. This result is consistent with the results presented by the other researchers ( Bandhauer et al., 2006; Yang and Webb, 1995; Park *et al.*, 2011). Depending upon the channel geometry and the mass flux, the flow pattern changes from mist flow to annular flow (for high vapor qualities) to intermittent flow (at lower vapor qualities) during the condensation in the

microchannels with the overlap of the flows (Bandhauer et al., 2006). Since the average vapor quality in MMHX was 50% and vapor quality variation along the condenser length was between 100 to 50%, it is expected to have annular flow pattern along most of its length. Heat transfer coefficient increases with the increase in vapor quality results in higher specific volume of the vapor phase and hence the higher vapor velocities. Apart from that, the annular film at the higher quality results in higher heat transfer due to lower film thickness (Agarwal et al., 2010). Thus, as the mass flux increases, heat transfer coefficient increases due to higher liquid and vapor velocities. Also, as we increase the mass flux, since there is no significant change in the heat flux in the condenser, amount of vapor condensed does not increase much and hence vapor quality and vapor velocities increase due to the increase in inlet vapor flow rate (or mass flux). This increase in vapor quality causes the mass transfer to increase.

To understand the effect of manifold on the condensation heat transfer, the results presented in the literature (Kumar *et al.*, 2005) for a double pipe condenser (similar to MMHX) was compared with the present results. Heat transfer coefficients for the commercial fin tubes vary from 3000 W/m$^2$-K to 6000 W/m$^2$-K for a 50% mean vapor quality. In comparison to that, the heat transfer coefficient for current MMHX condenser varied between 15,000 W/m$^2$-K and 40,000 W/m$^2$-K, which is almost 5-7 times higher. Thus the manifold has significant effect on the condensation heat transfer, similar to that of the single phase heat transfer experiments reported in chapter 5.
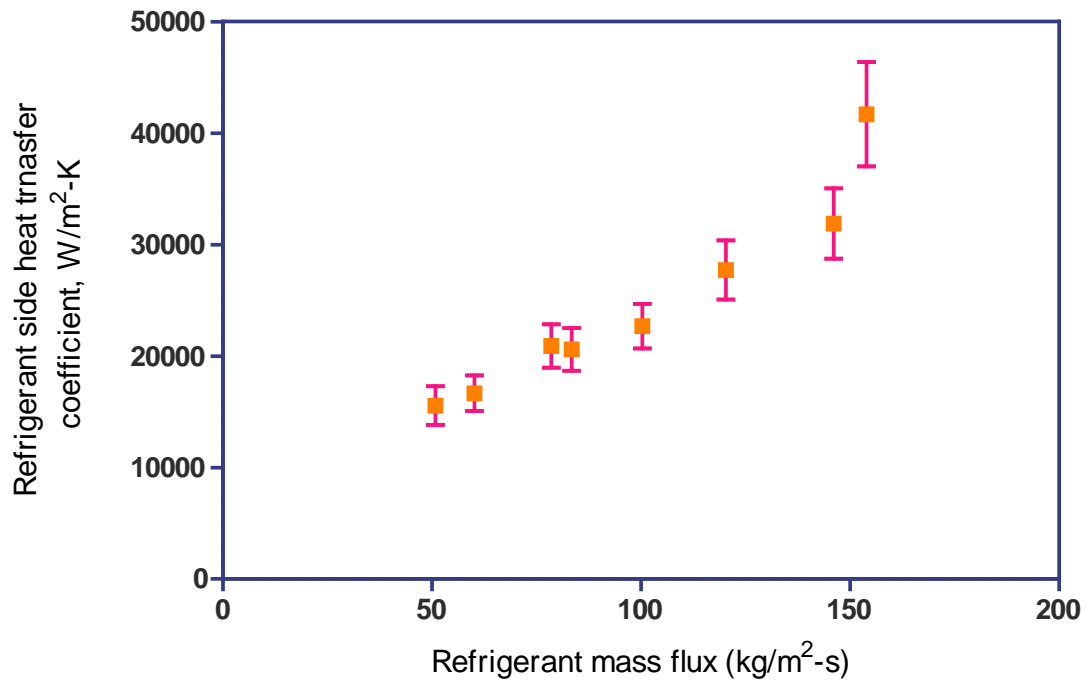
**Figure 7-5:** Refrigerant side heat transfer coefficient vs varying mass flux in microchannels
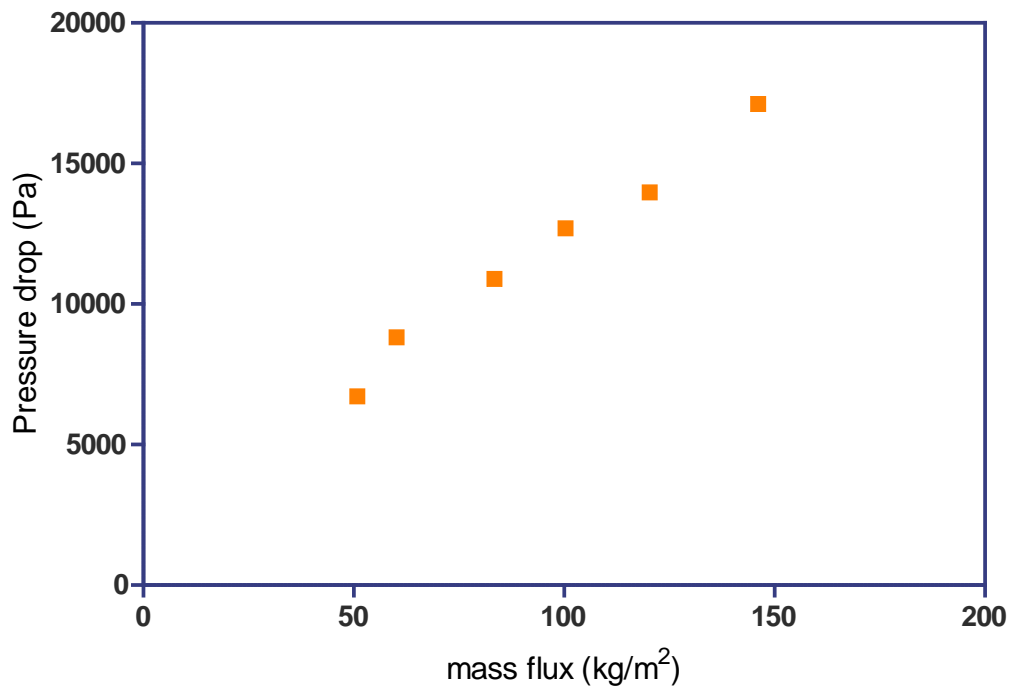


**Figure 7-6:** Effect of refrigerant mass flux in microchannels on pressure drop
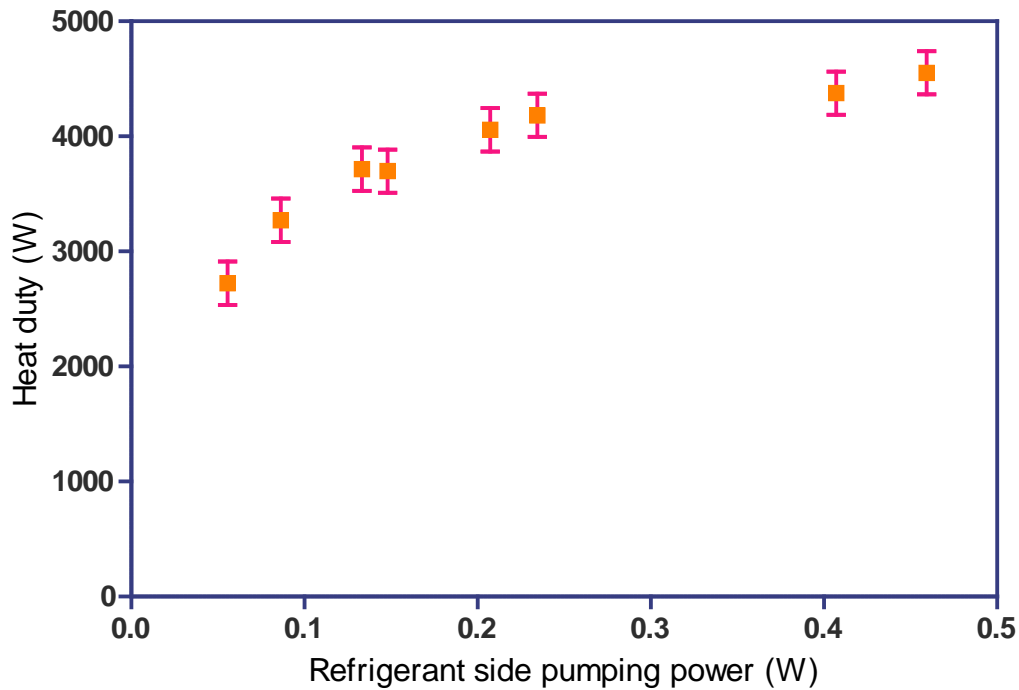
**Figure 7-7:** Heat duty vs. refrigerant side pumping power

Refrigerant side pressure drop increases almost linearly with the increase in the mass flux as shown in Figure 7-6. This increase in pressure drop is mainly due to the higher flow velocities at higher mass flux. Linear variation in pressure drop also confirms that the flow in the device is linear. Plot of heat duty vs. pumping power shows that the heat duty increases with pumping power almost linearly up to 4.0 kW (Figure 7-7). Beyond that the increase in the heat duty becomes very slow. This reduction in increase in heat duty at higher pumping power was mainly due to the high resistance offered by water side flow.

## 7.6   Chapter conclusions

Heat transfer and pressure drop inside the MMHX condenser was investigated for varying mass flux and a constant mean vapor quality of 50%. Heat transfer coefficient increased monotonically with the increase in mass flux. Heat transfer coefficient

based on the area of the fin tube is as high as ~ 40,000 W/m$^2$-K was achieved for refrigerant mass flux of 150kg/m$^2$. HTC increases with the mass flux linearly for the mass flow range investigated during this study. Pressure drop varied between 5kPa to 16 kPa and maximum heat duty was 4.5 kW. Since the flow rate to achieve this heat duty is low, overall pumping power requirement is low. Thus, MMHX experiments with condensation heat transfer have shown that high condensation heat transfer coefficients can be achieved in MMHX with low pumping power.

# 8 $CO_2$ absorption study in MMHX

This chapter presents the study of $CO_2$ absorption experiments in DEA solution in the MMHX. The experiments were performed using two different gases; 1) mixture of 10% $CO_2$ & 90% $N_2$ and 2) 100% $CO_2$ gas. The DEA concentration was varied from 20% to 40%. Effect of the different manifold sizes, leakage in the device was studied. Current study focuses on the gas sweetening process in MMHX microreactor. Experiments were performed to estimate mass transfer in microchannel absorber.

## 8.1 Introduction

Gas liquid reactions have large number of industrial applications such as hydrogenation, chlorination, oxidation, gas sweetening, etc. Conventional systems have poor heat/mass transfer, non-homogeneous flow distribution, and low two phase interfacial area. Since microreactors have very high interfacial area to volume ratio, they achieve high heat/mass transfer rates and thus can benefit such gas-liquid processes.

Current study was focused to estimate the mass transfer in MMHX for applications in natural gas sweetening, carbon capture and absorption refrigeration systems. For the gas sweetening or carbon capture applications, the mole fraction of the absorbed gas is typically 5% to 30% (Ganapathy, 2014). Keeping that in mind, the experiments were performed using 10% (molar) $CO_2$ gas and DEA solution with varying concentration. On the other hand, pure gas is absorbed in the absorption refrigeration systems and complete absorption occurs in the absorber. For example, in

Ammonia water absorbers, pure ammonia gets absorbed into the ammonia water solution. As discussed in chapter 6, ammonia experiments require dedicated facilities due to the safety regulations, and hence 100% $CO_2$ gas and DEA solution pair was used to get an estimate of the mass transfer process by using much safer $CO_2$ gas. Experiments performed with 100% $CO_2$ cannot be mapped for NH3-water application straight forward because NH3 absorption in water is highly exothermic reaction. However, with the 100% $CO_2$ experiments and separate heat transfer experiments, the order of magnitude of improvement in combined mass and heat transfer can be predicted.

## 8.2  Experimental setup

As shown in Figure 8-1, the experimental set-up is an open loop type. DEA solution is fed to the test section with the help of a variable speed liquid feed pump (model Idec GD-M35) from the solution container. The flow is measured using a coriolis flow meter. Gas is fed from the gas cylinder with the help of regulating valves. The flow is measured by coriolis flow meter (FCI). Fluid from the test section outlet is then sent to a gas-liquid separator to separate gas from the liquid. The size of the separator was kept small to avoid absorption in the separator itself. Length of the connecting piping between the separator and the test section was also kept to minimum possible value for the same reason. Liquid from the separator was then collected to another solution container.  A regulation valve was used in the liquid outlet line of the separator to maintain a fixed level of the liquid in the separator. Very low liquid level in the separator would result in gas passing to the liquid

container and a high liquid level will result in the bubbling of gas into the liquid, turning it into a small bubble absorber.

For 10% $CO_2$ experiments, the gas coming out of the separator was sent to a $CO_2$ gas analyzer to measure the percentage of $CO_2$ after absorption. Gas analyzer could handle only a certain amount of gas flow rate and hence the incoming gas from the separator was partly vented directly to the atmosphere and a steady flow of the gas was maintained to the analyzer with help of a rotameter. For 100% $CO_2$ cases, the gas mass flow from the separator gas outlet is measured using the coriolis flow meter (model E+H 83A01).

The data was recorded using an Agilent data Acquisition system every two seconds. However, only steady state data was taken for the calculation purposes. The gas sensor had a slow response and took about 3-4 minutes to stabilize at a constant number. A single run was typically done for about 5 minutes to make sure that the steady state was reached during the experiment. Inlet and outlet temperatures to the test section were measured using thermocouples (three thermocouples at each location). The inlet pressure was measured using a pressure transducer (model Setra 206) while the differential pressure across the test section was measured using the diaphragm type pressure transducers (Validyne P55D). The details of all the instrumentation used are provided in the appendix A.
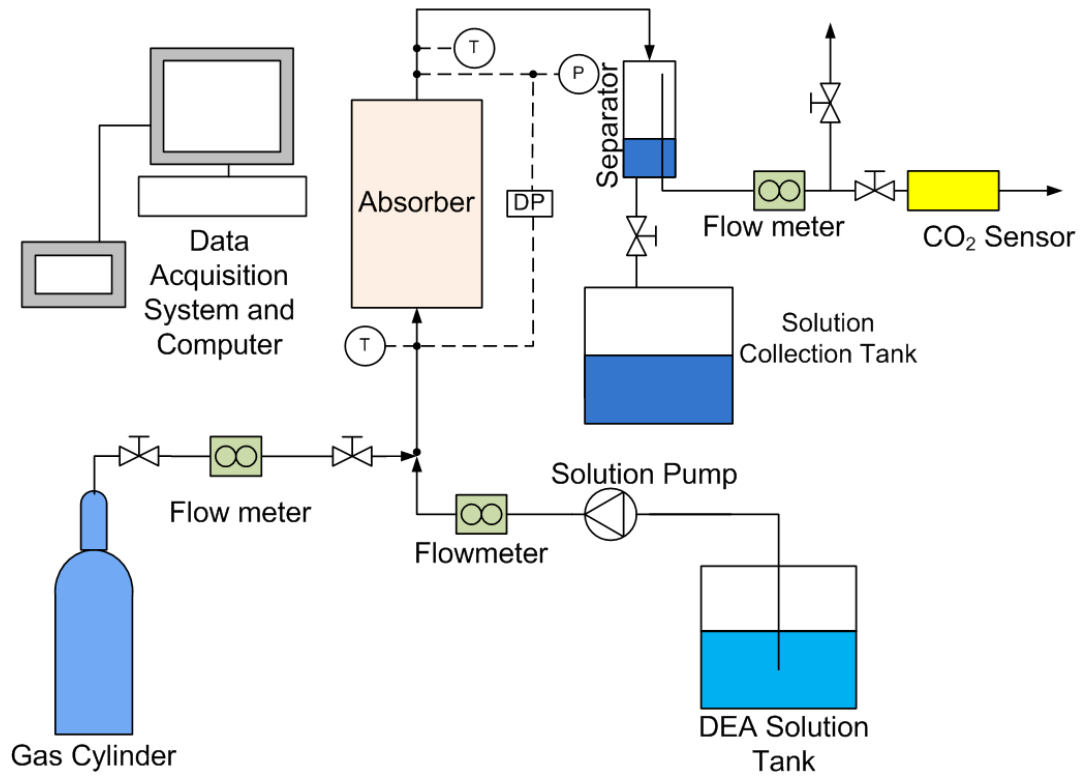
**Figure 8-1:** Schematic of the experimental setup for the absorption experiments
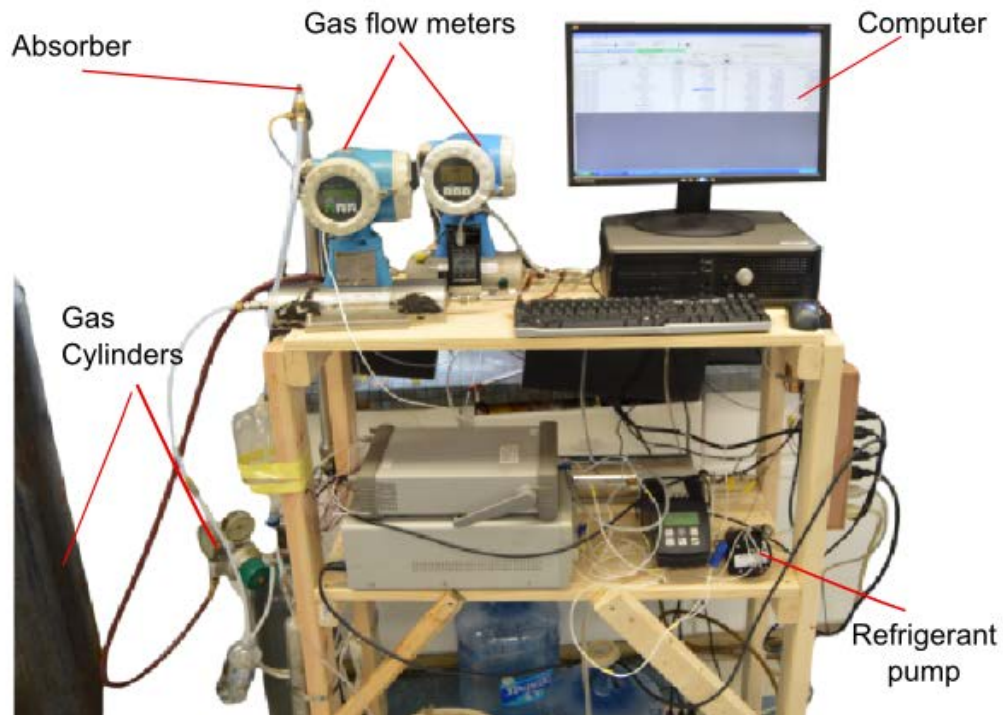


**Figure 8-2:** Absorption experimental setup photograph (1)
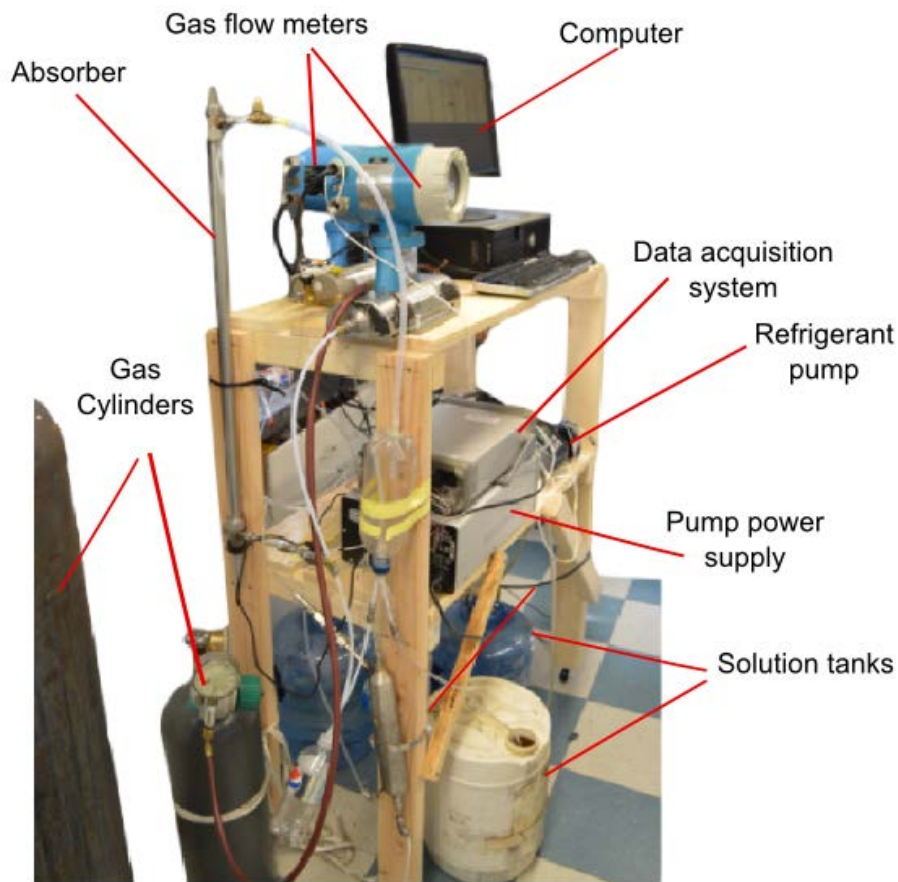
**Figure 8-3:** Absorption experimental setup photograph (2)

### 8.2.1 Experimental Procedure

***Open loop experiment:*** Typical $CO_2$ removal unit consists of amine absorber and a re-generator unit equipped with a reboiler, overhead condenser and a reflux drum as shown in the Figure 8-1 for the regeneration of the amine. Due to the high flow rates involved in the experiments, heating and cooling capacity needed for the in-line regeneration was high (more than 5 kW). This would also require a bigger regenerator as well as condenser to insure a good regeneration.

To avoid the high capacity heater and chillers, absorber experiment was made open loop. This process, however, required higher amount of DEA solution as well as extra time for regeneration in between the set of experiments. Once all the DEA solution was used up, it was regenerated by boiling it to get rid of any absorbed $CO_2$ in the solution. Any water lost during the regeneration was added to keep the DEA concentration in the solution constant.

All the experiments were performed at the room temperature of about 25 $^\circ$C. DEA solution was prepared using laboratory grade, 99% purity DEA by mixing it with distilled water in desired proportion. Operating conditions and the parameters used in the absorption experiments are presented in Table 8-1.

**Table 8-1:** Operating conditions and experimental parameters used in the experiments

| Parameters | Range |
|---|---|
| Gas flow rate (g/min) | 5-70 |
| Liquid flow rate (g/s) | 7-40 |
| DEA concentration (mass %) | 10-40 |
| Manifold stage length (inch) | 1.2 and 3 |
| Total number of absorber geometries | Three |
| $CO_2$ concentration (mol %) | 10 and 100 |
| Temperature (K) | 298 |
| Pressure (bar) | 1 |
| Liquid Reynold's number | 30-220 |

The experiments were performed by varying the gas flow rate for fixed liquid flow rates. 20% and 40% DEA solutions were used. Experiments were also done using a tight fit 1.2 inch manifold as well as loose fitted manifold. To study the complete absorption phenomena into the absorber, 100% $CO_2$ was used for varying

DEA concentration of 20% and 40% for 1.2 inch and 3.0 inch manifolds (MMHX-1 and MMHX-4). Experimental procedure was similar to that of 10% $CO_2$ case the amount of absorbed gas was measured differently. In this case, the gas coming out of the test section is sent to another Coriolis mass flow meter after the separator. The difference between inlet and outlet gas flows is the amount of the gas absorbed.

## 8.3 Data reduction

Since the diffusivity of $CO_2$ in the gas phase is very high, resistance to the mass transfer in the gas phase can be neglected and the liquid side resistance is prominent. Absorption flux can be obtained from the following reaction:

$$N_{CO_2} = \frac{n_{CO_2,in} - n_{CO_2,out}}{aV}$$

(38)

Where $n_{CO_2,in}$ and $n_{CO_2,out}$ are the molar flow rates at the inlet and outlet of the absorber. '$a$' is specific interfacial area and V is the volume of the reactor. Liquid side mass transfer coefficient, $k_L$ can be determined as

$$k_L = \frac{N_{CO_2}}{\Delta C_{CO_2,m}}$$

(39)

Where $\Delta C_{CO_2,m}$ is log mean concentration difference and is given by

$$\Delta C_{CO_2,m} = \frac{C^*_{CO_2,in} - C^*_{CO_2,out}}{\ln\left(C^*_{CO_2,in}/C^*_{CO_2,out}\right)}$$

(40)

Where $C^*_{CO_2}$ is the interfacial concentration of the $CO_2$. When the interfacial area cannot be determined, a volumetric mass transfer coefficient, $k_L a$ is used instead

$$k_L a = \frac{n_{CO_2,in} - n_{CO_2,out}}{V \cdot \Delta C_{CO_2,m}}$$

(41)

Log mean concentration different can be calculated in terms of the $CO_2$ partial pressure by using Henery's law.

$$p_{CO_2} = H C_{CO_2}^*$$ 
(42)

$$\Delta C_{CO_2,m} = \frac{1}{H}\left[\frac{p_{CO_2,in} - p_{CO_2,out}}{\ln\left(p_{CO_2,in}/p_{CO_2,out}\right)}\right]$$
(43)

Absorber efficiency, $\eta_{abs}$, is defined as

$$\eta_{abs} = \frac{C_{CO_2,in} - C_{CO_2,out}}{C_{CO_2,in}} \times 100\%$$
(51)

Where $C_{CO_2,in}$ and $C_{CO_2,out}$ are the concentrations of $CO_2$ gas at inlet and outlet. Acid loading is defined as number of moles of $CO_2$ absorber per mole of DEA. Properties of DEA solution of different concentrations are presented in the table as presented by (Ganapathy, 2014).

**Table 8-2:** Properties of aqueous DEA at various concentrations

| Mass fraction (%) | Concentration (mol/m3) | Density (kg/m3) | Viscosity (mPa s) | Density ratio (-) | Viscosity ratio (-) | $CO_2$ diffusivity (m$^2$/s) (x10-9) | Henry's constant (Pa m3/mol) |
|---|---|---|---|---|---|---|---|
| 0 | 0 | 997.10 | 0.89 | 1 | 1 | 1.91 | 3090.70 |
| 5 | 474.76 | 1001.31 | 1.09 | 1.004 | 1.224 | 1.64 | 3268.61 |
| 10 | 949.52 | 1005.56 | 1.23 | 1.008 | 1.381 | 1.46 | 3320.19 |
| 15 | 1424.29 | 1009.85 | 1.38 | 1.013 | 1.550 | 1.27 | 3371.76 |
| 20 | 1899.05 | 1014.17 | 1.53 | 1.017 | 1.718 | 1.08 | 3423.34 |

Heat of reaction for $CO_2$ absorption in DEA is 68.8 kJ/mol (Kohl & Nielsen, 1997). This exothermic reaction causes the temperature of the system to increase. Maximum measured values for the temperature increase for partial $CO_2$ absorption (10%) was within 2 $^\circ$C whereas this rise in the temperature for pure $CO_2$ was as high as 12 $^\circ$C.

## 8.4 Uncertainty analysis:

Uncertainty analysis was performed using law of propagation of uncertainty as discussed in the single phase heat transfer chapter (chapter 5). Estimated uncertainties are given in the following table.

**Table 8-3:** Parameters and estimated uncertainties

| Parameters | Uncertainty |
|---|---|
| Temperature ($^{\circ}$C) | $\pm 0.5$ |
| Solution mass flow rate | $\pm 0.1\%$ |
| Gas mass flow rate | $\pm 0.5\%$ |
| $CO_2$ gas concentration measurement | $\pm 3.0\%$ ($\pm 1.5\%$ FS) |
| Mass transfer coefficient (for 10% $CO_2$) | $\pm 14.2\%$ |
| Mass transfer coefficient (for 100% $CO_2$) | $\pm 3.1\%$ |
| Absorption efficiency (for 10% $CO_2$) | $\pm 9.4\%$ |
| Absorption efficiency (for 100% $CO_2$) | $\pm 2.9\%$ |
| Pressure drop | $\pm 0.25\%$ |
| Absolute pressure | $\pm 0.2\%$ |

### 8.4.1 Error due to connecting piping and the separator

The estimation of the absorption in the test section was performed based on the total interfacial area available in the connecting piping from test section to the separator and the maximum possible interfacial area in the separator itself. Considering the worst possible case, amount of absorption in piping and in the separator amounted to a maximum of 6% of that in the test section. This amount was subtracted from the final results to avoid the errors due to the use of separator.

## 8.5 Results and discussions

### 8.5.1 100% CO₂ experiments

#### 8.5.1.1 Effect of liquid and gas Reynolds numbers

Figure **8-4** shows that volumetric mass transfer coefficient for fixed liquid Reynolds number increases with the increase in the gas Reynolds number, achieves a maximum value before starting to decrease. Also, it is observed that $k_L a$ is higher for higher liquid Reynolds numbers. Two major reasons for this behavior in mass transfer are the 1) flow pattern and 2) acid loading. As discussed in flow visualization chapter (section 4.2.3), bubble size reduces with the increase in the liquid and gas flow rates causing interfacial to increase. This increase in the interfacial area results in higher $k_L a$ when the liquid or gas flow rates are increased. Second major factor affecting the overall mass transfer is the acid loading of the solution. Absorption of $CO_2$ in DEA involves both physical absorption as well as chemical reaction. As $CO_2$ chemically reacts with the DEA to form carbonates, carbamates and bicarbonates (Benamor and Aroua, 2005), amount of DEA available for further reaction reduces as the absorption process progresses. In other words, higher acid loading results in lower mass transfer. Limit of the $CO_2$ or acid loading is 0.5 mol/mol. However, depending upon the partial pressure of the $CO_2$, higher acid loadings can be achieved. Due to the complexity in determining the exact mechanism and hence the limit of acid loading, it is difficult to accurately estimate the effect of acid loading on the mass transfer. Hence for the simplification purposes the effect of acid loading has been integrated with the volumetric mass transfer coefficient itself. As the acid loading increases, mass

transfer coefficient decreases. As seen in Figure 8-7, acid loading increases with the increase in gas flow rate but decreases with the increase in liquid flow rate as the total amount of DEA in the solution is higher for higher liquid flow rates. Thus, the mass transfer increases due to increase in interfacial area at the beginning with the increase in gas Reynolds number. However, further increase in the gas Reynolds number causes the acid loading to increase which in turn decreases $k_L a$. These two competing factors cause the maxima in the graph of $k_L a$ vs. gas Reynolds number as seen in Figure **8-4**. Effect of liquid flow rate may be understood by the similar reasoning. $k_L a$ increases with the increasing liquid flow rates due to the increase in the interfacial area (because of decrease in bubble size). $k_L a$ also increases due to reduction in acid loading resulting from higher liquid flow rates. However, the difference in $k_L a$ values for different liquid flow rates at lower gas Reynolds numbers is not as significant. It appears that the acid loading becomes more dominant factor at elevated acid loadings.

Similar to the increase in liquid flow rate, increase in gas flow rate also causes the reduction of bubble size and hence increase of interfacial area to volume ratio. However, as discussed in section 4.2.3, the effect of the gas flow rate on the bubble size is not as significant as that of the liquid flow rate. Initial increase in the mass transfer coefficient with the increase in gas Re is attributed to this increase in the interfacial area to volume ratio. However, as the gas flow increases further, $CO_2$ loading in DEA solution starts becoming significant (Figure 8-7), reducing further mass transfer. Hence at the higher gas flow rates the mass transfer starts to decrease. Similar trends have been noticed in the literature for the absorption of pure $CO_2$ in

hydroxide solution both in rectangular (Yue et al., 2007) or circular microchannels ((Tortopidis and Bontozoglou, 1997; Vandu et al., 2005).

Increase in the gas Reynolds number for constant liquid Reynolds number causes to reduce the absorption efficiency monotonically (Figure 8-5). Higher gas flow rate at a constant liquid flow rate increases the absorption rate and hence the acid loading which in turn reduces the mean concentration difference. Since the mass transfer is proportional to the mean concentration difference (equation 43), lower mean concentration difference results in lower mass transfer and hence lower absorption efficiency. It was also observed that the absorption efficiency is higher for the higher liquid Reynolds number. This is due to the higher mean concentration difference and hence higher mass transfer resulting from lower acid loading for the higher liquid flow rate for fixed gas flow rates (Figure 8-7). Increase in the liquid flow rates causes higher interfacial and hence the absorption efficiency for higher liquid flow rates is found to be higher. Pressure drop increases with the increase in the gas flow rate for a fixed liquid flow, which is consistent with the classical theories of two phase pressure drop as shown in Figure 8-6.
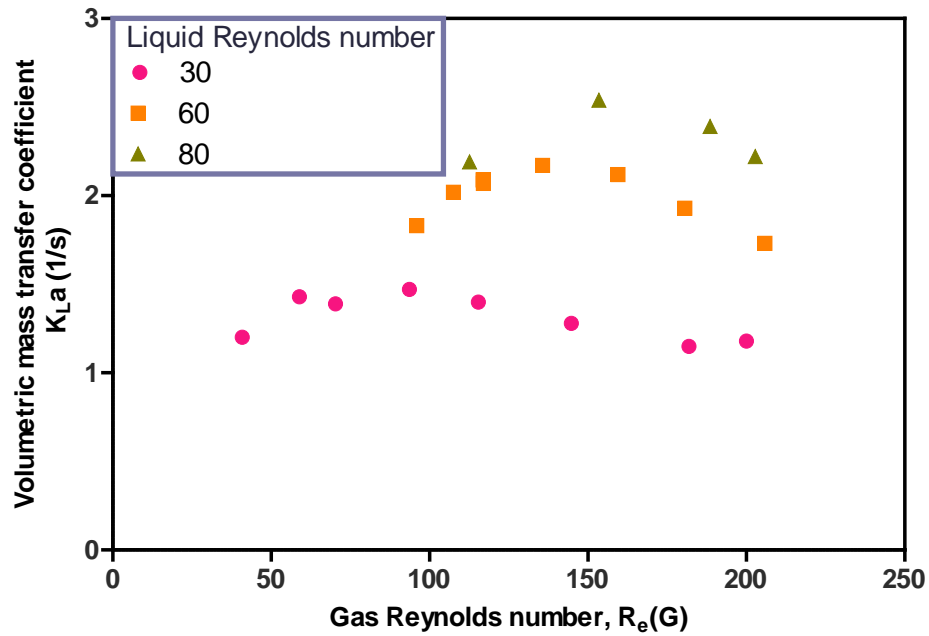
**Figure 8-4:** Effect of fluid flow on the mass transfer coefficient efficiency ($C_{CO2}$: 100% by mass of $CO_2$, $C_{DEA}$: 20% by mass of DEA in water)
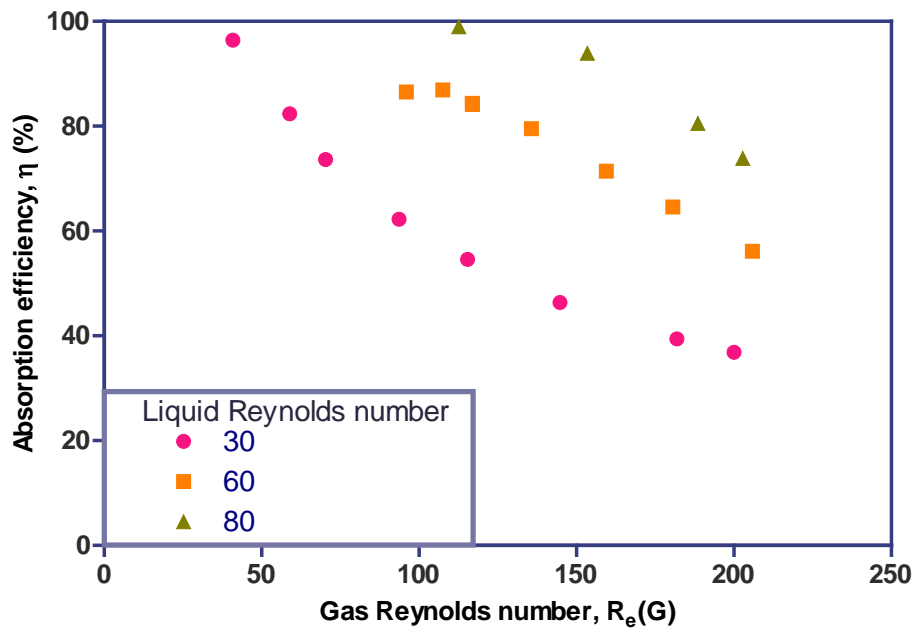


**Figure 8-5:** Effect of fluid flow on the absorption efficiency ($C_{CO2}$: 100% by mass of $CO_2$, $C_{DEA}$: 20% by mass of DEA in water)
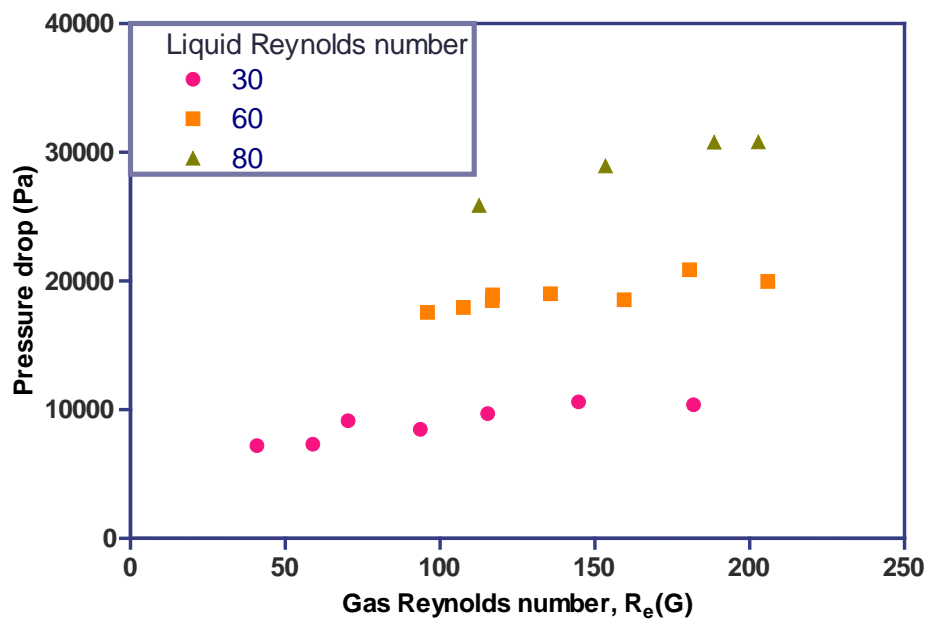
**Figure 8-6:** Effect of fluid flow on pressure drop ($C_{CO2}$: 100% by mass of $CO_2$, $C_{DEA}$: 20% by mass of DEA in water)
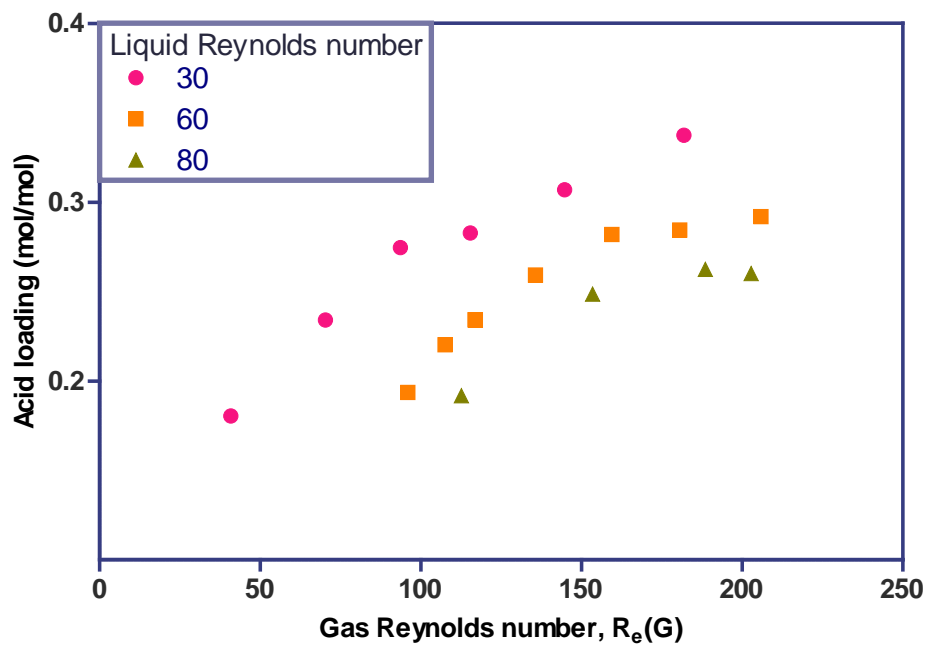


**Figure 8-7:** $CO_2$ loading vs. liquid and gas flow ($C_{CO2}$: 100% by mass of $CO_2$, $C_{DEA}$: 20% by mass of DEA in water)

## 8.6 Partial absorption of the Gas (10% $CO_2$)

The results of the experiments for partial absorption of $CO_2$ are discussed in this section.

### 8.6.1 Effect of liquid and gas flow rate

As shown in Figure 8-8 $k_L a$ increases with the gas Reynolds number monotonically, however the effect of liquid flow rate is not significant. The reason for increase in $k_L a$ is similar to the one discussed in the previous 100% $CO_2$ absorption section. In comparison to the pure $CO_2$ absorption it is observed that partial $CO_2$ cases did not show a maximum but the increasing trend in the $k_L a$ values with gas flow velocities. This is attributed to the fact that the $CO_2$ loadings for partial $CO_2$ experiments are significantly lower (0.02 to 0.04 mol/mol) as compared to that for 100% CO2 (0.2 to 0.3 mol/mol). Hence the acid loading doesn't play significant role in the variation of $k_L a$. Also, due to this reason, the difference between the $k_L a$ for two different liquid Reynolds numbers is not significant.

As expected, pressure drop increases with the increase in the gas velocity for a fixed liquid flow (Figure 8-9). Similarly, the DP increases as the liquid velocity is increased. It is observed that the mass transfer coefficient for higher solution concentration is higher for the same liquid and gas flow velocity. Absorption efficiency decreases with the increase in the gas Reynolds number (Figure 8-10). Absorption efficiency in MMHX increases with the increase in mass transfer coefficient, interfacial area to gas flow rate ratio and liquid to gas flow rate ratio. Although the overall mass transfer increase due to the higher gas flow rate tends to increase the efficiency, efficiency decreases with increase in gas flow rate due to

133

increased gas to liquid flow ratio for a fixed liquid Reynolds number and reduced interfacial area to gas flow rate ratio. Efficiency for the higher liquid Reynolds number cases for a fixed gas Reynolds number is higher due to the higher mass transfer coefficient and liquid to gas flow rate ratio. As expected, the mass transfer increases with the increase in the gas Reynolds number, increasing the acid loading of the solution for a fixed liquid Reynolds number Figure 8-11. Although the mass transfer for higher liquid Reynolds number cases (for fixed gas Reynolds numbers) is higher, the acid loading is lower due to the dominant effect of the liquid to gas mass flow rate ratio on the acid loading.

### 8.6.2 Effect of DEA concentration

As shown in the Figure 8-12, difference between $k_L a$ for 20% and 40% DEA solutions increases as the gas Reynolds number increases. At lower gas flows, the concentration difference has not much effect on $k_L a$ due to very low $CO_2$ loading. However, as the $CO_2$ loading increases with the increase in the gas flow, the higher concentration of solution increases the absorption. It should also be noted that the properties of the liquid at different DEA concentrations are different which may affect the flow pattern in the absorber and hence the mass transfer. Further study is needed to understand this effect of liquid properties.

Pressure drop for the higher DEA concentration is slightly higher for higher concentration (Figure 8-13). The difference in the pressure drop for various cases varied between 5 to 11%. There are two competing factors which play role in pressure drop change. Higher viscosity of the 40% concentration liquid leads to the
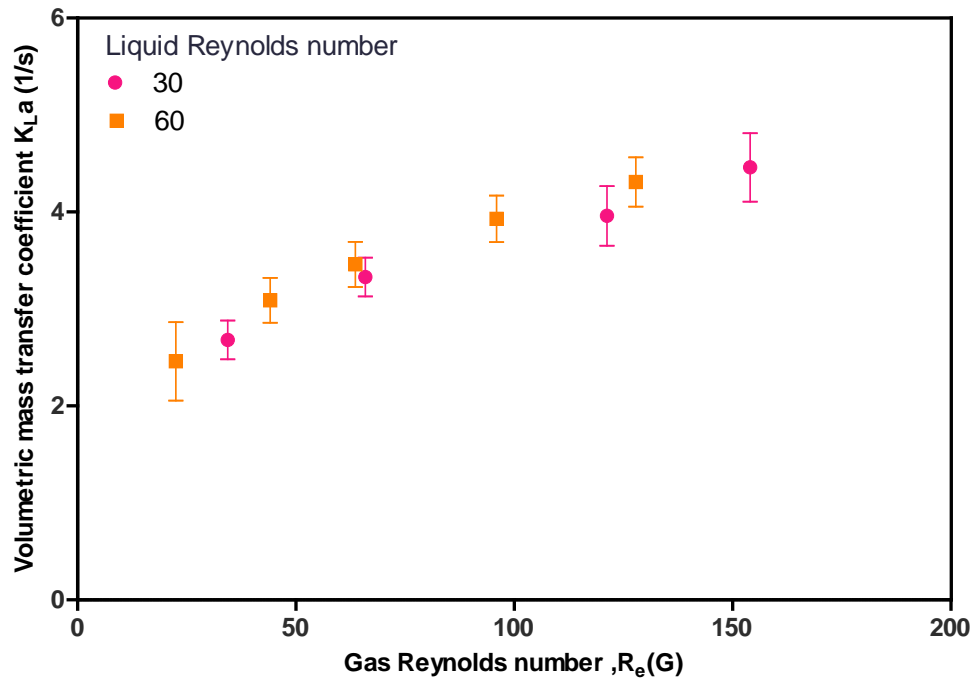
**Figure 8-8:** Effect of gas and liquid flow rate on the absorption mass transfer coefficient ($C_{CO2}$: 10% by mass of $CO_2$ in $N_2$; $C_{DEA}$: 20% by mass of DEA in water).
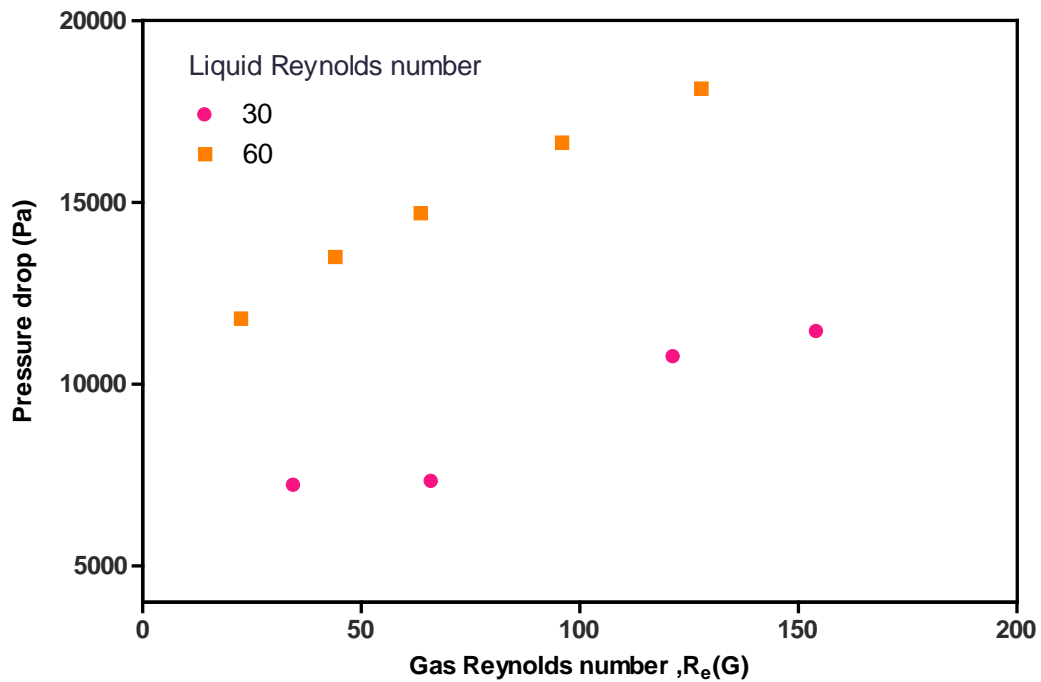


**Figure 8-9:** Effect of gas and liquid flow rate on the pressure drop ($C_{CO2}$: 10% by mass of $CO_2$ in $N_2$; $C_{DEA}$: 20% by mass of DEA in water).
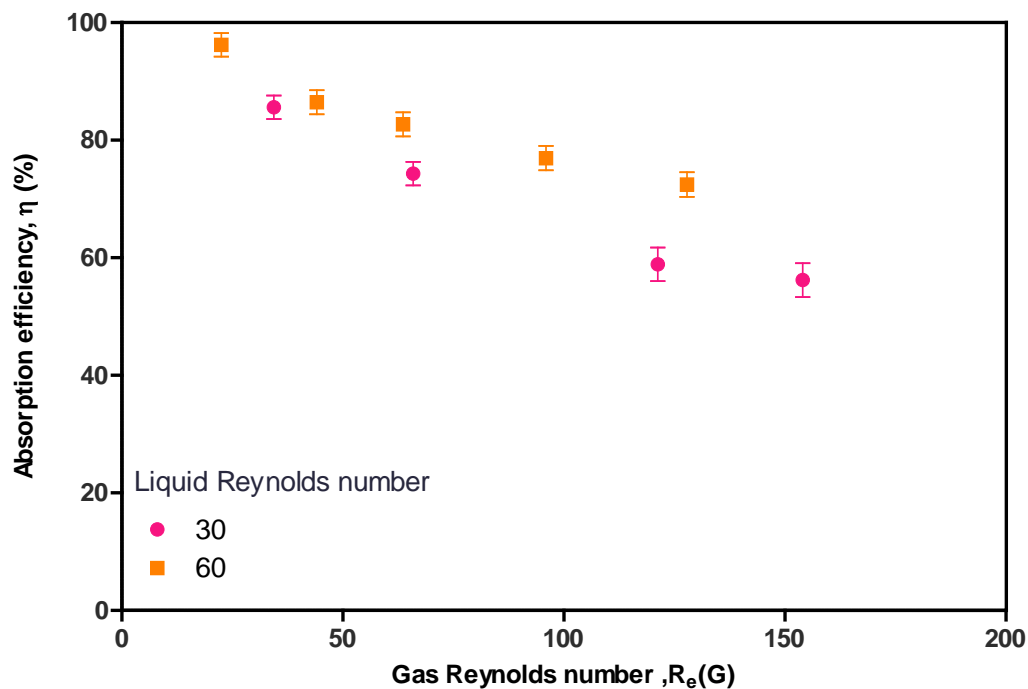
**Figure 8-10:** Effect of gas and liquid flow rate on the absorption efficiency ($C_{CO2}$: 10% by mass of $CO_2$ in $N_2$; $C_{DEA}$: 20% by mass of DEA in water).
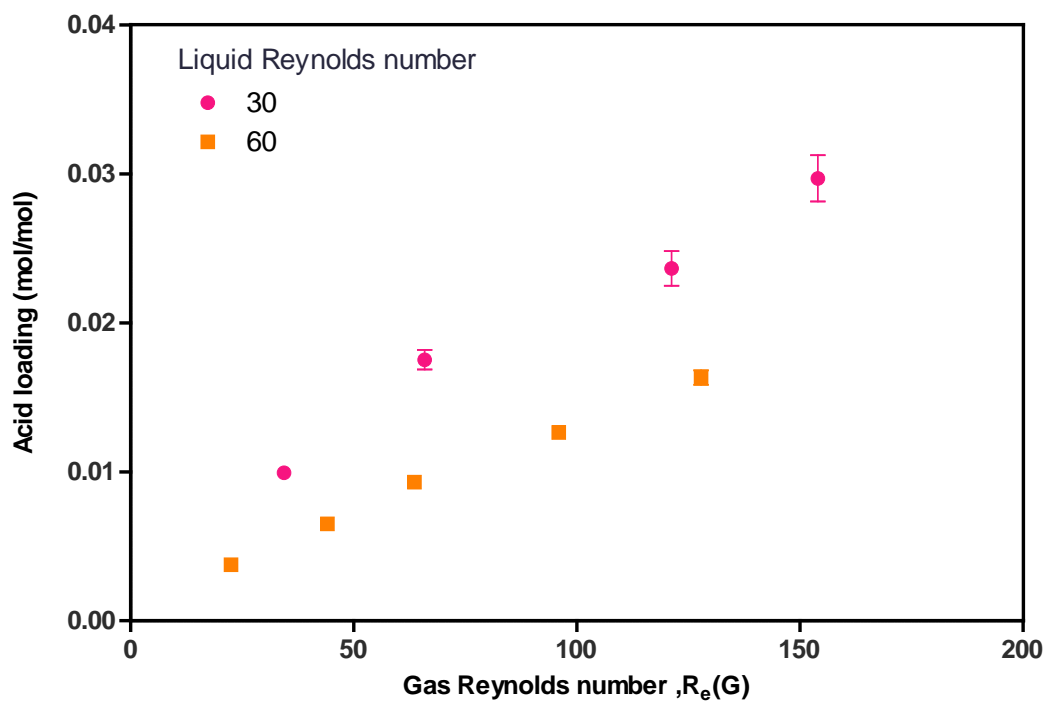


**Figure 8-11:** Effect of gas and liquid flow rate on the acid loading ($C_{CO2}$: 10% by mass of $CO_2$ in $N_2$; $C_{DEA}$: 20% by mass of DEA in water).
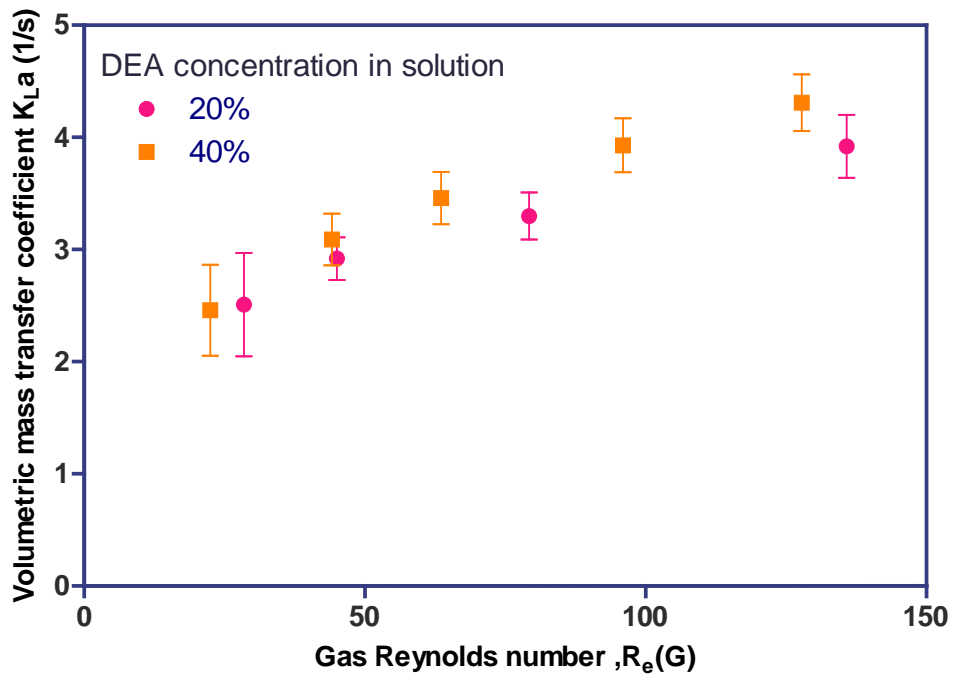
**Figure 8-12:** Effect of DEA concentration on mass transfer coefficient ($C_{CO2}$: 10% by mass of $CO_2$ in $N_2$)
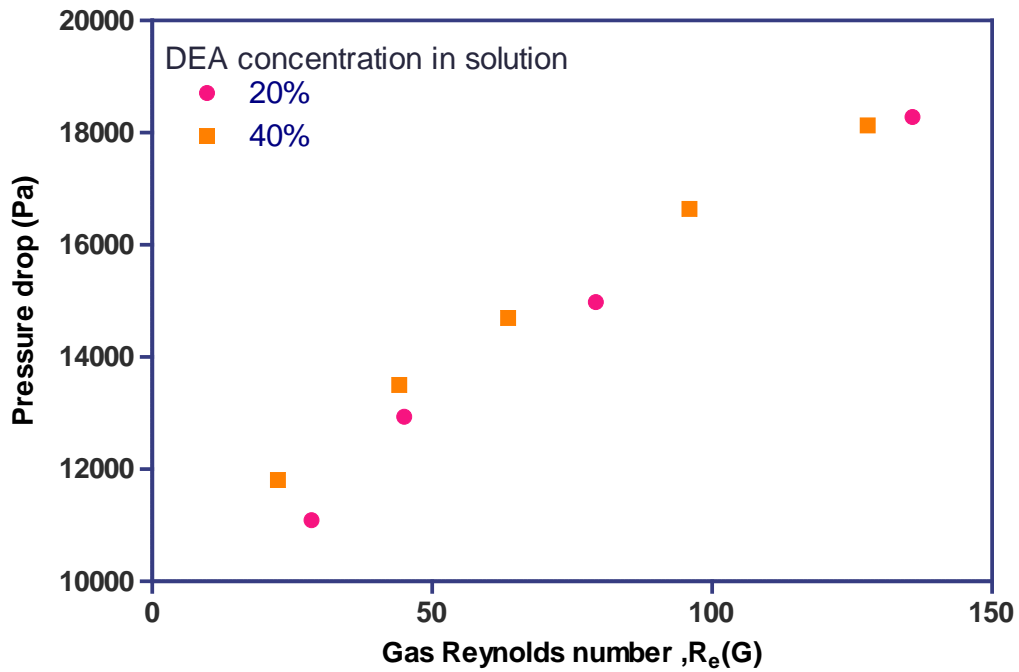


**Figure 8-13:** Effect of DEA concentration on pressure drop ($C_{CO2}$: 10% by mass of $CO_2$ in $N_2$)

**Figure 8-14:** Effect of DEA concentration on absorption efficiency ($C_{CO2}$: 10% by mass of $CO_2$ in $N_2$)
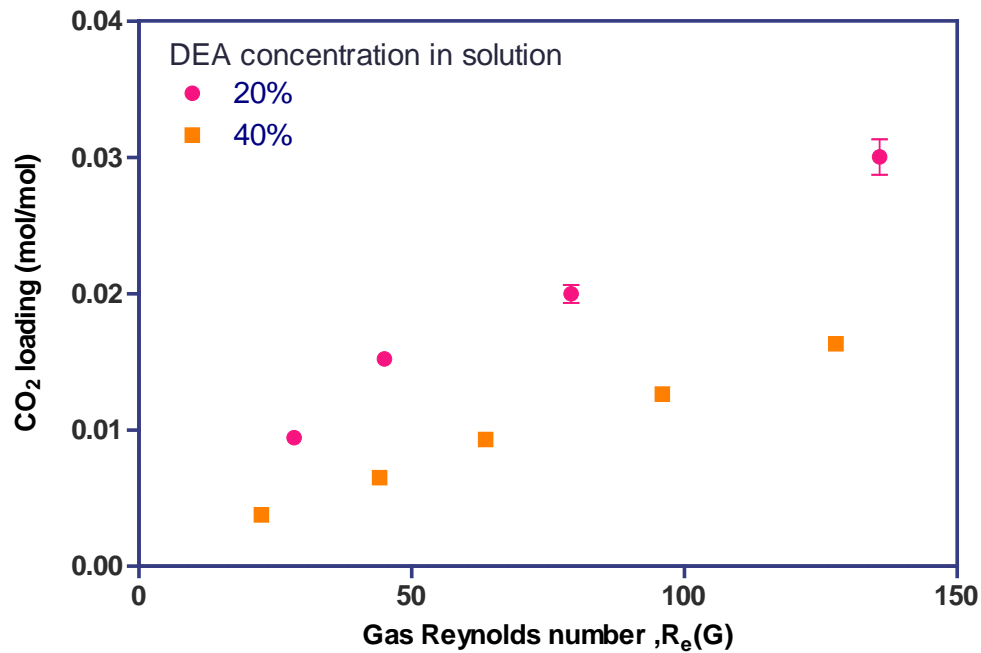


**Figure 8-15:** Effect of DEA concentration on $CO_2$ loading ($C_{CO2}$: 10% by mass of $CO_2$ in $N_2$)

higher friction factors and hence higher pressure drops. Second factor is the reduction of the gas fraction for higher concentration of the DEA which caused the reduction of pressure drop. From the experimental results it is clear that the effect of the viscosity is dominant for the investigated operating conditions.

Absorption efficiency for the higher DEA concentration is higher as expected (Figure 8-14). Decrease in the absorption efficiency with increasing gas flow rate is explained in section 8.5.1    The higher absorption efficiency for 40% DEA concentration is related to the higher mass transfer coefficient as shown in Figure 8-12.

### 8.6.3    Effect of leakage

As discussed in the flow visualization chapter, flow leakage seems to have considerable effect on the flow pattern. This causes significant reduction in the interfacial area reduction and hence the reduction in the mass transfer. To study the effect of leakage inside the MMHX, two different test sections were tested. First test section was regular MMHX-1 with a loose fit manifold. The second test section was made leak tight by wrapping a thin plastic sheet over the manifold of MMHX-1 to make it leak tight (similar to the one described in the visualization experiment). It should be noted that the amount of leakage from the loose fit manifold was not determined and hence the study here is mainly qualitative.

Experimental results for the absorber with and without sleeve were compared for two different liquid Reynolds numbers to investigate the effect of leakage on $k_L a$ (Figure 8-16), pressure drop (Figure 8-17), absorption efficiency (Figure 8-18) and

acid loading (Figure 8-19). It was found that the mass transfer in the absorber with sleeves was significantly higher than that in loose fit absorber. Two phase flow visualization study showed that a large amount of gas leaks through the gap between the manifold and the outer shell in the loose fit MMHX and thus the gas flow in the microchannels is reduced, causing lower interfacial area inside the microchannels. Opposite to the loose fit manifolds, gas in the sleeved manifolds did not leak through the gap between manifold and outer shell but passed though the microchannels. This resulted in the bubbly flow pattern and apparently higher interfacial area and hence higher values of $k_L a$. It can be noticed that the slope of $k_L a$ vs. gas Reynolds number curve is higher for the loose fit manifolds. Thus the difference between the $k_L a$ values reduces at higher values of gas Reynolds number. As the absorption in the MMHX increases, the acid loading increases. This acid loading is higher for the tight fit manifolds due to the higher absorption rate. The higher loading, however, reduces the further absorption process and hence the difference between the loose fit manifolds reduces as the gas velocity increases. The difference between the interfacial area for the loose fit and tight fit manifolds may be different at different flow rates which may affect the mass transfer coefficient.

Pressure drop for the loose fit MMHX was found to be lower than that for the manifold with sleeves (Figure 8-17). Leakage causes the fluid to take the lowest resistance route causing a good portion of liquid and gas not entering the microchannels and hence reducing the pressure drop. The reduction in the pressure drop will depend upon the extent of the gap between the sealing surfaces.
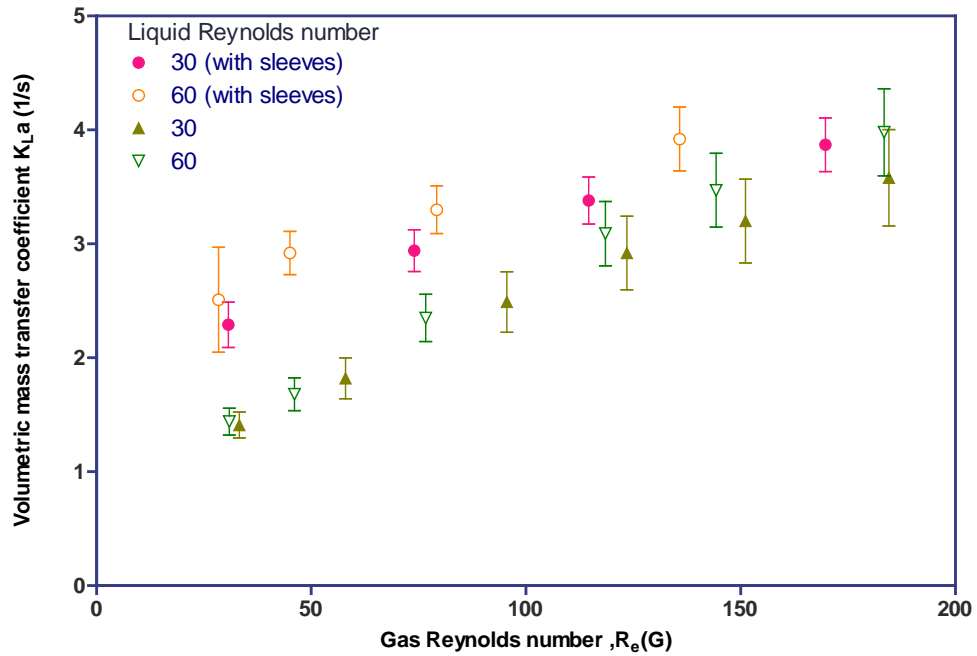
**Figure 8-16:** Effect of leakage on mass transfer coefficient ($C_{CO2}$: 10% by mass of $CO_2$ in $N_2$)
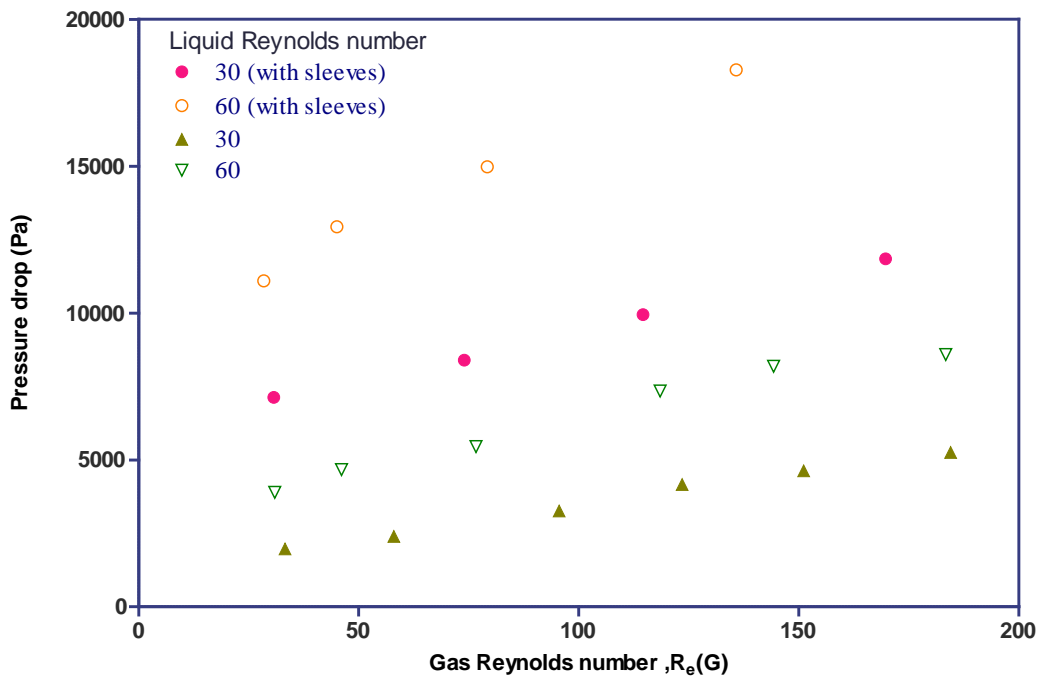


**Figure 8-17:** Effect of leakage on pressure drop ($C_{CO2}$: 10% by mass of $CO_2$ in $N_2$)
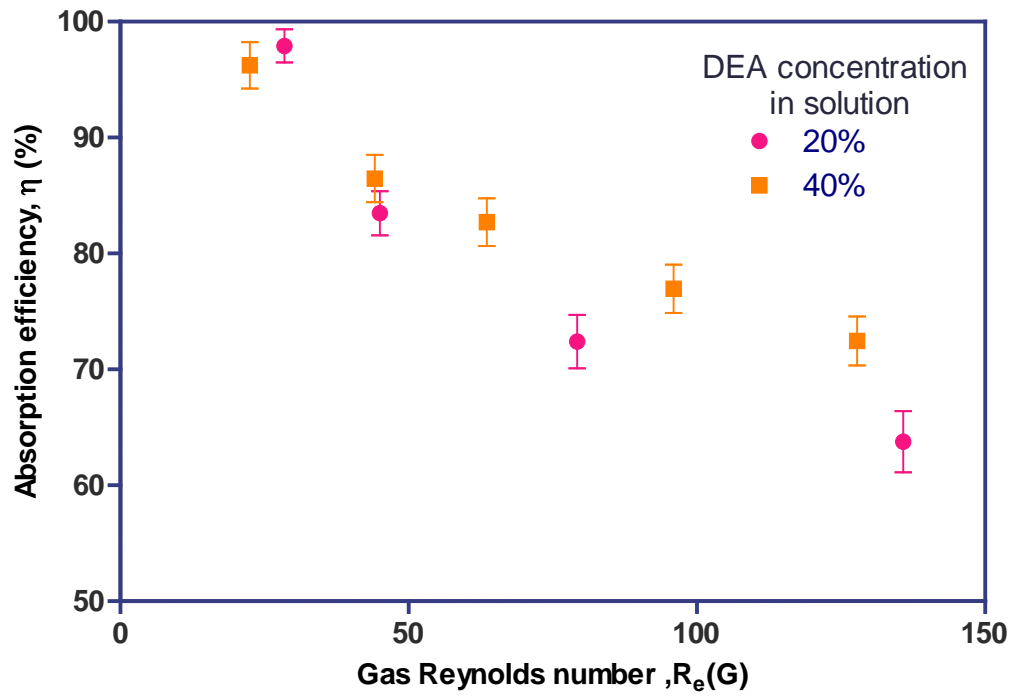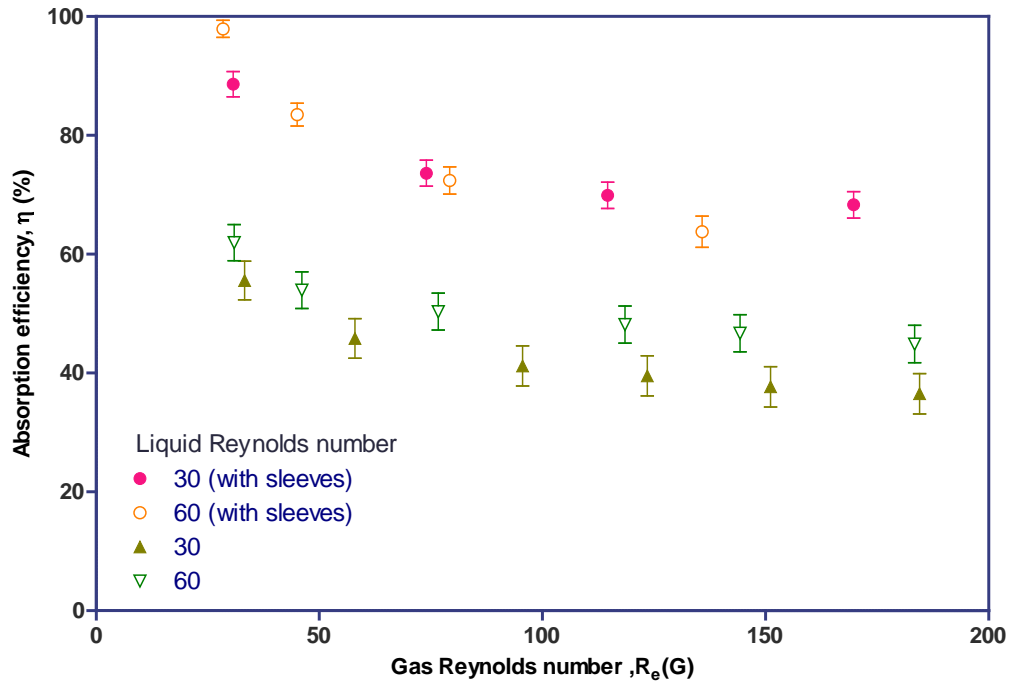
**Figure 8-18:** Effect of leakage on absorption efficiency ($C_{CO2}$: 10% by mass of $CO_2$ in $N_2$)
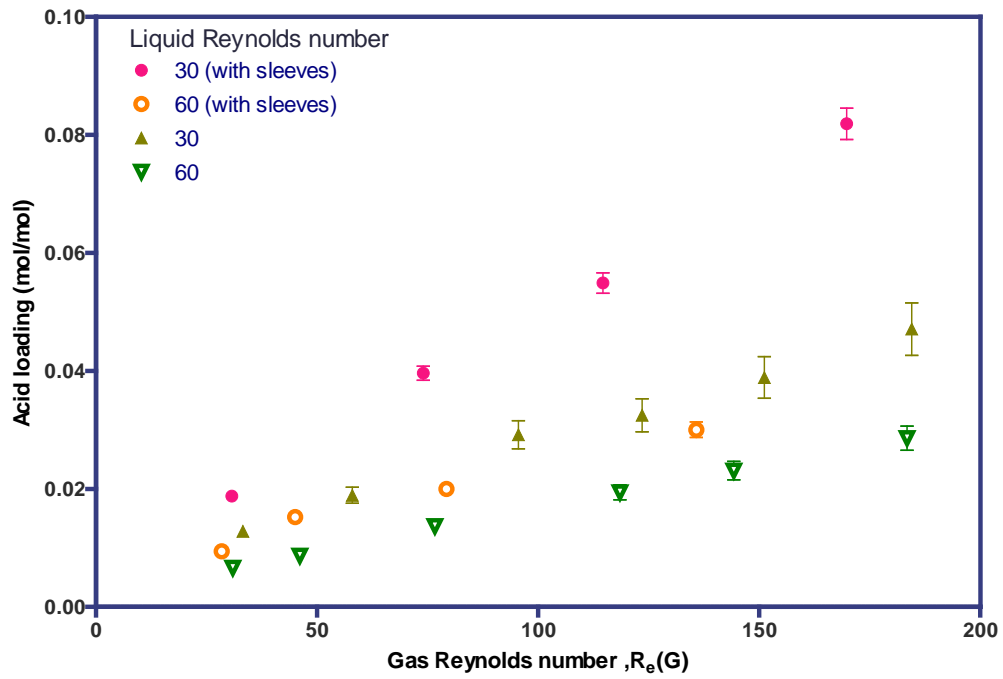


**Figure 8-19:** Effect of leakage on acid loading ($C_{CO2}$: 10% by mass of $CO_2$ in $N_2$)

Absorption efficiency decreases with the increase in gas Reynolds number for both the loose fit and tight fit manifolds (

Figure **8-18**). As discussed earlier, increase in gas Reynolds number increases the $k_L a$ and thus the total absorption, however, the ratio of the absorbed $CO_2$ to inlet $CO_2$ reduces with increase in gas flow rate. Thus the overall efficiency reduces with increase in gas Re for a fixed volume reactor. Depending upon the gas Reynolds number, absorption efficiency for the loose fit reactors is about 30%-40% lower than that for tight fit absorbers. Effect of gas Reynolds number on the acid loading are reported in Figure 8-19. As per the definition, acid loading is expected to be the highest for the low liquid flow rates and high gas flow rates. Since the extent of absorption in the manifolds with the sleeves is higher, the acid loading is also higher for the tight fit absorbers.

## 8.7 Comparison with the conventional systems

The performance comparison of the MMHX was done with the conventional absorbers as shown in the table 3. It is to be noted that the volumetric mass transfer coefficient presented by the author includes various solvents. However, it is argued that the mass transfer coefficient for $CO_2$-DEA shall fall within the range provided by the author. $k_l a$ for MMHX is about one to two order of magnitude higher than those in the conventional technologies. This indicates that the micro-reactor is capable of significant intensification of mass transfer. Apart from the reduction of the size, microchannel device will also significantly reduce the total charge of the overall $CO_2$ scrubbing unit (especially inside the heat exchanger components).

**Table 8-4:** Comparison of mass transfer coefficient achieved in the conventional reactors and the current MMHX (Ganapathy, 2014)

| Type of system | $k_L$ (x$10^{-5}$) (m/s) | $a$ (m$^2$/m$^3$) | $k_La$ (x$10^{-2}$) (1/s) |
| --- | --- | --- | --- |
| Countercurrent packed columns | 4-20 | 10-350 | 0.04-7 |
| Co-current packed columns | 4-60 | 10-1700 | 0.04-102 |
| Bubble cap plate columns | 10-50 | 100-400 | 1-20 |
| Sieve plate columns | 10-200 | 100-200 | 1-40 |
| Bubble columns | 10-40 | 50-600 | 0.5-24 |
| Packed bubble columns | 10-40 | 50-300 | 0.5-12 |
| Horizontal and coiled tube reactors | 10-100 | 100-2000 | 0.5-70 |
| Vertical tube reactors | 20-50 | 10-100 | 2-100 |
| Spray columns | 7-15 | 100-2000 | 0.07-1.5 |
| Mechanically agitated bubble reactors | 3-40 | 20-120 | 0.3-80 |
| Submerged and plunging jet reactors | 1.5-5 | 20-50 | 0.03-0.6 |
| Hydro cyclone reactors | 100-300 | 100-2000 | 2-15 |
| Venturi reactors | 50-100 | 160-2500 | 8-25 |
| Microchannel reactor (Yue et al., 2007) | 40-160 | 3400-9000 | 30-2100 |
| MMHX used in the present study | - | - | 120-423 |

## 8.8 Chapter conclusions

Gas liquid absorption of $CO_2$-DEA pair inside the MMHX was studied in this chapter using pure $CO_2$ gas and 10% $CO_2$ gas mixture. Effects of the gas and liquid flow rates, manifold size, flow leakage, DEA concentration on the mass transfer coefficient, pressure drop and absorption efficiency were studied in detail. Following were the conclusions from the study:

1.  Mass transfer coefficient increases with the increase in gas and liquid flow rates for partial has absorption. However, for 100% $CO_2$ case, the mass transfer increases, reaches to a maximum and then starts to decrease with the increase in gas flow rate. Pressure drop was found to be monotonically increasing with increasing gas and liquid flow rates.

2.  The flow leakage plays a significant role in the absorption process. It was observed that if the manifold to the microchannel tube and the outer shell tube joint was not tight fit, there was significant amount of leakage which reduced the mass transfer significantly. The experiments with leak tight device showed almost 80%-100% improvements in absorption performance.

3.  Change of the manifold stage length affects the mass transfer and the pressure drop. Results indicated that the lower stage length of the manifold increases the absorption efficiency. This was due to the increased number of passes for the same length of the absorber. Decrease in the manifold length also resulted in increased pressure drop.

4.  Increasing the DEA concentration inside the solution increased the absorption efficiency as well as the pressure drop in the absorber.

# 9   Conclusions and future work

Current work proposes a novel design concept for the multipass manifold microchannel heat and mass exchanger for single and two phase heat transfer and gas liquid absorption applications. An extensive experimental study was performed using manifold microchannel heat exchangers (MMHX) for industrial heat and mass transfer applications. Experiments were performed for two phase visualization study, heat transfer in single phase liquid, evaporation and condensation as well as gas liquid absorption in the MMHX. A number of conclusions can be drawn from the study conducted which is listed as following:

- Tubular design of the MMHX uses mass produced fin tubes as microchannels. It's simple geometry and easy assembly makes the device cost effective. The weight and size of the of MMHX is substantially lower when compared to the conventional heat exchangers such as plate heat exchanger or shell and tube heat exchanger of similar capacity. This reduction was due to almost an order of magnitude higher heat transfer and achieved in the device.

- Visual study of the flow pattern was performed in the MMHX using nitrogen gas and water for different gas and liquid flow rates and manifold designs. Lower liquid flow rates in the MMHX resulted in the coalesced bubbles flow in the manifold. For higher liquid flow rates, the flow distribution was much more uniform in the manifold and the microchannels. It was observed that the MMHX design also works as a good flow distributer. A non uniform inlet flow was observed to be uniformly distributed in the device within 3 to 4 inches from the inlet. Two different manifold shapes were compared for flow

pattern and pressure drop. Diamond shape manifold showed better flow distribution and lower pressure drop. MMHX with loose fit manifolds showed significant amount of leakage from the space between the manifold and outer shell. It was also concluded that the horizontal or vertical orientation of the MMHX does not affect the flow pattern except for very lower liquid flows.

- Single phase heat transfer and pressure drop was investigated in MMHX using water as working fluid on both hot and cold side. Heat transfer coefficient increases with the increase in manifold side liquid flow rate. Heat transfer coefficient in the MMHX was compared with the double pipe heat exchanger. Shell side heat transfer coefficient was almost an order of magnitude higher than the double pipe heat exchangers. Shell side base heat transfer coefficients up to 30,000 $W/m^2$-K were achieved. Pumping power required for the MMHX was also significantly lower than that for the double pipe heat exchanger.

- Pressure drop contribution from the manifold for single phase was numerically calculated and compared with experimental results. It was within 10% to 20% of the total pressure drop in the device. However, at very high flow rates, the pressure drop in the manifold starts becoming more significant.

- MMHX was used in the evaporation mode by using R134a refrigerant at its saturation pressure of close to 7 bars. It was found that the shell side boiling heat transfer coefficient of the MMHX was an order of magnitude higher than that in the conventional evaporators. HTC increased monotonically with the increase in refrigerant mass flux. Base boiling heat transfer coefficient was found to be as high as 45,000 $W/m^2$-K on shell side. Refrigerant charge

required in the MMHX was substantially low (90g) as compared to conventional plate type evaporator (1000g). Comparison of heat transfer for two tube geometries, plain fin and enhanced fin, showed 30-40% higher shell side HTC for plain fin tube (MMHX-1). Pressure drop in the plain fin was 15-20% higher than that for enhanced fin tube geometry. Experiments with varying saturation pressure showed that the heat transfer coefficient did not strongly depend upon the saturation pressure.

- MMHX experiments with condensation heat transfer have shown that high heat transfer coefficients can be achieved with low pumping power. Shell side heat transfer coefficient is as high as 30,000 $W/m^2$-K based on base area was achieved for refrigerant mass flux of 150$kg/m^2$. HTC increases with the mass flux linearly for the mass flow range investigated during this study. Pressure drop in the MMHX was between 5kPa to 16kPa and maximum heat duty found was 4.5kW. Since the shell side flow rate corresponding to this heat duty is low, overall pumping power requirement is lower as compared to the conventional condensers.

- Gas liquid absorption of $CO_2$-DEA pair inside the MMHX was studied using pure $CO_2$ gas and 10% $CO_2$ gas mixture. The effect of the gas and liquid flow rates, manifold size, flow leakage, DEA concentration on the mass transfer coefficient, pressure drop and absorption efficiency was studied in detail. Mass transfer coefficient was found to be increasing with the increase in gas and liquid flow rate for partial has absorption. The flow leakage plays a significant role in the absorption process. It was observed that if the manifold

to the microchannel tube and the outer shell tube joint was not tightly fit, there was significant amount of leakage which reduced the mass transfer significantly. The experiments with leak tight device showed almost 80%-100% improvements in absorption performance. Higher absorption efficiency as well as the pressure drop was found in the shorter manifold stage lengths MMHX.

## 9.1 Future work

Current study on multipass manifold microchannel heat exchanger has demonstrated that MMHX can achieve significantly higher heat and mass transfer which shall enable the device to be compact and low cost for industrial applications. The next step would be to scale up the design for higher capacity. The current design uses single fin tube, however, a multi-tube design is needed to scale up the device.

It should be noted that the tube side flow in MMHX is significantly higher than that in the shell side. Thus the current MMHX design is well suited for two phase heat transfer applications where the shell side is represented by phase changing fluid and tube side as single phase and thus the heat capacities of the two sides are comparable.

However, for the single phase heat transfer applications, the heat capacity of the tube side fluid is much higher than shell side fluid due to its higher flow rate. Lower shell side flow rate and high overall heat transfer coefficient result in shell side fluid quickly approaching the temperature of the tube side fluid. This in turn results in very high efficiency in a short distance of the MMHX. For single phase heat transfer, it is

desirable to redesign the MMHX to handle higher flow rates on shell side. Hence the next set of development should be focused on developing the heat exchanger whose shell side as well as tube sides has the similar flow.

# Appendix 1

| Equipment | Manufacturer | Model No. | Range | Accuracy |
|-----------|--------------|-----------|-------|----------|
| Condenser chiller | NESLAB | HX500 | +5 $^\circ$C to 35 $^\circ$C | +/- 0.1 $^\circ$C |
| Evaporator chiller | NESLAB | M72 | +5 $^\circ$C to 55 $^\circ$C | +/- 0.15 $^\circ$C |
| Water flow meter | E+H | 63F15 | 0-2200 kg/h | +/- 0.1% FS |
| Coriolis flow meter | FCI | | | |
| Absolute Pressure | Setra | 206 | 0-250PSI | +/- 0.2% FS |
| DP1 | Validyne | P55D | 0-32 PSI | +/- 0.25% FS |
| DP2 | Sensotech | A5/882-12 | 0-5PSI | +/- 0.25% FS |
| Variable speed pump | Idec | GD-M35 | 0-90 g/s | - |
| Plate HX | Alfa Laval | CB26-24H | - | - |
| Power supply for pump | | | 0-35V | +/- 0.5% FS |
| Thermocouples | Omega | T-Type | -200$^0$ to 350 $^\circ$C | +/-0.5 $^\circ$C |
| Data Acq. system | Agilent | 34970A | 60 analogue inputs | - |
| Water heater | - | - | 3 kW | - |

# 10 References

Agarwal, A. & Garimella, S. (2009) Modeling of pressure drop during condensation in circular and noncircular microchannels. *Journal of Fluids Engineering*, **131**, 011302.

Agarwal, A., Bandhauer, T.M. & Garimella, S. (2010) Measurement and modeling of condensation heat transfer in non-circular microchannels. *International Journal of Refrigeration-Revue Internationale Du Froid*, **33**, 1169-1179.

Agostini, B., Thome, J.R., Fabbri, M., Michel, B., Calmi, D. & Kloter, U. (2008) High heat flux flow boiling in silicon multi-microchannels–Part I: heat transfer characteristics of refrigerant R236fa. *International Journal of Heat and Mass Transfer*, **51**, 5400-5414.

Akars W. W., D.H.A.a.C.O.K. (1959) Condensation heat transfer within horizontal tube. *Chem. Eng. Prog. Symp. Ser. 55*, 171-176.

Andhare, R.S. (2013) Charecterization of heat transfer and pressure drop of normal flow heat exchangers in counter flow configuration. *Master's Thesis*,

Arie, M., Shooshtari, A., Dessiatoun, S., Al-Hajri, E. & Ohadi, M. (2015) Numerical modeling and thermal optimization of a single-phase flow manifold-microchannel plate heat exchanger. *International Journal of Heat and Mass Transfer*, **81**, 478-489.

Arie, M.A., Shooshtari, A., Dessiatoun, S. & Ohadi, M. (2014) Thermal optimization of an air-cooling heat exchanger utilizing manifold-microchannels. *Thermal and Thermomechanical Phenomena in Electronic Systems (ITherm), 2014 IEEE Intersociety Conference on* (ed by, pp. 807-815.

Baird, J., Fletcher, D. & Haynes, B. (2003) Local condensation heat transfer rates in fine passages. *International Journal of Heat and Mass Transfer*, **46**, 4453-4466.

Bandhauer, T.M., Agarwal, A. & Garimella, S. (2006) Measurement and modeling of condensation heat transfer coefficients in circular microchannels. *Journal of heat transfer*, **128**, 1050-1059.

Baummer, T., Cetegen, E., Ohadi, M. & Dessiatoun, S. (2008) Force-fed evaporation and condensation utilizing advanced micro-structured surfaces and micro-channels. *Microelectronics Journal*, 39, 975-980.

Benamor, A., and M. K. Aroua. "Modeling of CO 2 solubility and carbamate concentration in DEA, MDEA and their mixtures using the Deshmukh–Mather model." Fluid Phase Equilibria 231, no. 2 (2005): 150-162.

Bertsch, S.S., Groll, E.A. & Garimella, S.V. (2008) Refrigerant flow boiling heat transfer in parallel microchannels as a function of local vapor quality. *International Journal of Heat and Mass Transfer*, **51**, 4775-4787.

Bertsch, Stefan S., Eckhard A. Groll, and Suresh V. Garimella. "Effects of heat flux, mass flux, vapor quality, and saturation temperature on flow boiling heat transfer in microchannels." *International Journal of Multiphase Flow* 35, no. 2 (2009): 142-154.

Boyea, D., Shooshtari, A., Dessiatoun, S.V. & Ohadi, M.M. (2013) Heat Transfer and Pressure Drop Characteristics of a Liquid Cooled Manifold-Microgroove Condenser. *ASME 2013 Heat Transfer Summer Conference collocated with the ASME 2013 7th International Conference on Energy Sustainability and the ASME 2013 11th International Conference on Fuel Cell Science, Engineering and Technology* (ed by, pp. V003T23A003-V003T23A003.

Boyea, D.L. (2013) *Heat Transfer and Pressure Drop Characteristics of a Manifold Microgroove Aerospace Condenser.* University of Maryland (College Park, Md.),

Brophy, J. (2005) The microchannel revolution. *Focus on Catalysts*, 1-2.

Caplow, M. (1968) Kinetics of carbamate formation and breakdown. *Journal of the American Chemical Society*, **90**, 6795-6803.

Cavallini, A., Del Col, D., Doretti, L., Matkovic, M., Rossetto, L. & Zilio, C. (2005) Condensation heat transfer and pressure gradient inside multiport minichannels. *Heat transfer engineering*, **26**, 45-55.

Cetegen, E. (2008) Heat Transfer Analysis in Force Fed Evaporation on Microgrooved Surfaces. In: (ed. S. Dessiatoun). Proceedings of the Sixth International ASME Conference on Nanochannels, Microchannels and Minichannels, Germany.

Cetegen, E., Dessiatoun, S. & Ohadi, M. Force Fed Boiling and Condensation for High Heat Flux Applications. *power*, **1**, x10-3.

Cetegen, E., Baummer, T., Dessiatoun, S., Ohadi, M. & Asme (2007) Heat transfer analysis of
microgrooved evaporator and condenser surfaces utilized in a high heat flux two-phase flow
loop. *ASME International Mechanical Engineering Congress and Exposition* (ed by, pp.
1031-1037. Seattle, WA.

Chai, L., Xia, G., Zhou, M., Li, J. & Qi, J. (2013) Optimum thermal design of interrupted
microchannel heat sink with rectangular ribs in the transverse microchambers. *Applied
Thermal Engineering*, **51**, 880-889.

Chakraborty, A., Astarita, G. & Bischoff, K. (1986) $CO_2$ absorption in aqueous solutions of hindered
amines. *Chemical Engineering Science*, **41**, 997-1003.

Charpentier, J.-C. (2007) In the frame of globalization and sustainability, process intensification, a path
to the future of chemical and process engineering (molecules into money). *Chemical
Engineering Journal*, **134**, 84-92.

Chen, J.F., Chen, G.Z., Wang, J.X., Shao, L. & Li, P.F. (2011) High-throughput microporous
tube-in-tube microreactor as novel gas–liquid contactor: Mass transfer study. *AIChE journal*,
**57**, 239-249.

Chen, S., Yang, Z., Duan, Y., Chen, Y. & Wu, D. (2014) Simulation of condensation flow in a
rectangular microchannel. *Chemical Engineering and Processing*, **76**, 60-69.

Chen, Y. & Cheng, P. (2005) Condensation of steam in silicon microchannels. *International
Communications in Heat and Mass Transfer*, **32**, 175-183.

Cheng, H.-H. & Tan, C.-S. (2011) Removal of CO2 from indoor air by alkanolamine in a rotating
packed bed. *Separation and Purification Technology*, **82**, 156-166.

Cheng, Y. (2007) Numerical simulation of stacked microchannel heat sink with mixing-enhanced
passive structure. *International communications in heat and mass transfer*, **34**, 295-303.

Chung, P.-Y. & Kawaji, M. (2004) The effect of channel diameter on adiabatic two-phase flow
characteristics in microchannels. *International Journal of Multiphase Flow*, **30**, 735-761.

Coleman, J.W. & Garimella, S. (2003) Two-phase flow regimes in round, square and rectangular tubes
during condensation of refrigerant R134a. *International Journal of Refrigeration-Revue
Internationale Du Froid*, **26**, 117-128.

Constantinou, A. & Gavriilidis, A. (2009) CO2 absorption in a microstructured mesh reactor. *Industrial & Engineering Chemistry Research*, **49**, 1041-1049.

Constantinou, A., Barrass, S., Pronk, F., Bril, T., Wenn, D.A., Shaw, J.E.A. & Gavriilidis, A. (2012) CO2 absorption in a high efficiency silicon nitride mesh contactor. *Chemical Engineering Journal*, **207–208**, 766-771.

Copeland, D. (1995) Manifold microchannel heat sinks: Analysis and optimization. (ed by, p. 169.

Copeland, D., Behnia, M. & Nakayama, W. (1997) Manifold microchannel heat sinks: isothermal analysis. *Components, Packaging, and Manufacturing Technology, Part A, IEEE Transactions on*, **20**, 96-102.

Copeland, D., TAKAHIRA, H., NAKAYAMA, W. & Bock-Choon, P. (1995) Manifold microchannel heat sinks: Theory and experiment. *伝熱研究– News of HTSJ*, **34**, 9-15.

Cunningham, J.L. & Campbell, B.J. (1977) Method of making heat transfer tube. In. Google Patents

Danckwerts, P. (1979) The reaction of $CO_2$ with ethanolamines. *Chemical Engineering Science*, **34**, 443-446.

Danckwerts, P.V., Sharma, M.M., Danckwerts, P.V. & Danckwerts, P.V. (1966) *The Absorption of Carbon Dioxide Into Solutions of Alkalis and Amines:(with Some Notes on Hydrogen Sulphide and Carbonyl Sulphide)*. Institution of Chemical Engineers.

Dang, M., Yue, J., Chen, G. & Yuan, Q. (2013) Formation characteristics of Taylor bubbles in a microchannel with a converging shape mixing junction. *Chemical Engineering Journal*, **223**, 99-109.

Edvin, C. (2010) *Forced Fed Microchannel High Heat Flux Cooling Utilizing Microgrooved Surfaces*. University of Maryland

English, Nathan J., and Satish G. Kandlikar. "An experimental investigation into the effect of surfactants on air-water two-phase flow in minichannels." *Heat Transfer Engineering* 27, no. 4 (2006): 99-109.

Escher, W., Brunschwiler, T., Michel, B. & Poulikakos, D. (2010) Experimental investigation of an ultrathin manifold microchannel heat sink for liquid-cooled chips. *Journal of Heat Transfer*, **132**, 081402.

Freemantle, M. & LONDON, C. (2004) Pilot Plant Velocys' facility in Plain City, Ohio, has several automated enclosures for testing microchannel devices. VELOCYS PHOTO. *Science & Technology*, **82**, 39-43.

Freemantle, M. & London, C. (2004) Pilot plant: Velocys' facility in Plain City, Ohio, has several automated enclosures for testing microchannel devices. *Science & Technology*, **82**, 39-43.

Ganapathy, H. (2014) *Enhanced Gas-Liquid Absorption Utilizing Micro-Structured Surfaces and Fluid Delivery Systems*. University of Maryland, College Park,

ganapathy, H. (2014) *Enhanced Gas-Liquid Absorption Utilizing Micro-Structured Surfaces*. University Of Maryland,

Ganapathy, H., Shooshtari, A., Dessiatoun, S., Alshehhi, M. & Ohadi, M.M. (2013) Experimental Investigation of Enhanced Absorption of Carbon Dioxide in Diethanolamine in a Microreactor. *ASME 2013 11th International Conference on Nanochannels, Microchannels, and Minichannels* (ed by, pp. V001T03A013-V001T03A013.

Gao, N.-N., Wang, J.-X., Shao, L. & Chen, J.-F. (2011) Removal of carbon dioxide by absorption in microporous tube-in-tube microchannel reactor. *Industrial & Engineering Chemistry Research*, **50**, 6369-6374.

Garimella, S. (2004) Condensation flow mechanisms in microchannels: Basis for pressure drop and heat transfer models. *Heat Transfer Engineering*, **25**, 104-116.

Garimella, S. & Wicht, A. (1995) Air-cooled condensation of ammonia in flat-tube, multi-louver fin heat exchangers. *ASME-PUBLICATIONS-HTD*, **320**, 47-58.

Garimella, S., Agarwal, A. & Killion, J.D. (2005) Condensation pressure drop in circular microchannels. *Heat Transfer Engineering*, **26**, 28-35.

Ghiaasiaan, S.M. (2008) *Two-phase flow, boiling, and condensation: in conventional and miniature systems*. Cambridge University Press.

Grzybowski, H. & Mosdorf, R. (2014) Dynamics of pressure oscillations in flow boiling and condensation in the minichannel. *International Journal of Heat and Mass Transfer*, **73**, 500-510.

Haji-Sulaiman, M.Z., Aroua, M.K. & Benamor, A. (1998) Analysis of Equilibrium Data of CO2 in Aqueous Solutions of Diethanolamine (DEA), Methyldiethanolamine (MDEA) and Their Mixtures Using the Modified Kent Eisenberg Model. *Chemical Engineering Research and Design*, **76**, 961-968.

Haller, D., Woias, P. & Kockmann, N. (2009) Simulation and experimental investigation of pressure loss and heat transfer in microchannel networks containing bends and T-junctions. *International Journal of Heat and Mass Transfer*, **52**, 2678-2689.

Harpole, G.M. & Eninger, J.E. (1991) Micro-channel heat exchanger optimization. *Semiconductor Thermal Measurement and Management Symposium, 1991. SEMI-THERM VII. Proceedings., Seventh Annual IEEE* (ed by, pp. 59-63.

Hüther, A., Geißelmann, A. & Hahn, H. (2005) Prozessintensivierung – Eine strategische Option für die chemische Industrie. *Chemie Ingenieur Technik*, **77**, 1829-1837.

Jang, S.P. & Kim, S.J. (2005) Fluid flow and thermal characteristics of a microchannel heat sink subject to an impinging air jet. *Journal of heat transfer*, **127**, 770-779.

Jankowski, N.R., Everhart, L., Morgan, B., Geil, B. & McCluskey, P. (2007) Comparing microchannel technologies to minimize the thermal stack and improve thermal performance in hybrid electric vehicles. *Vehicle Power and Propulsion Conference, 2007. VPPC 2007. IEEE* (ed by, pp. 124-130.

Jha, V. (2012) *High-performance tubular evaporator utilizing high aspect ratio manifold microchannels*. PhD Thesis, University of Maryland,

Jha, V., Dessiatoun, S., Ohadi, M., Shooshtari, A. & Al-Hajri, E. (2011) High Performance Micro-Grooved Evaporative Heat Transfer Surface for Low Grade Waste Heat Recovery Applications. *ASME 2011 Pacific Rim Technical Conference and Exhibition on Packaging and Integration of Electronic and Photonic Systems* (ed by, pp. 277-283.

Johnston, A. & Haynes, B. (2002) Heatric steam reforming technology. *2nd Topical Conference on Natural Gas Utilisation* (ed by.

Kandlikar, S. (1990) A general correlation for saturated two-phase flow boiling heat transfer inside horizontal and vertical tubes. *J. Heat Transfer*, **112**, 219–228.

Kandlikar, S. & Steinke, M. (2003) Predicting heat transfer during flow boiling in minichannels and Microchannels. *Transactions-american society of heating refrigerating and air conditioning engineers*, **109**, 667-676.

Kandlikar, S., Garimella, S., Li, D., Colin, S. & King, M.R. (2005) *Heat transfer and fluid flow in minichannels and microchannels*. Elsevier.

Kandlikar, S.G. (2002a) Two-phase flow patterns, pressure drop, and heat transfer during boiling in minichannel flow passages of compact evaporators. *Heat Transfer Engineering*, **23**, 5-23.

Kandlikar, S.G. (2002b) Fundamental issues related to flow boiling in minichannels and microchannels. *Experimental Thermal and Fluid Science*, **26**, 389-407.

Kandlikar, S.G. (2003) Heat transfer mechanisms during flow boiling in microchannels. *ASME 2003 1st International Conference on Microchannels and Minichannels* (ed by, pp. 33-46.

Keil, F. (2007) *Modeling of process intensification*. John Wiley & Sons.

Kendall, G.E., Griffith, P., Bergles, A.E. & Lienhard V, J. (2001) Small diameter effects on internal flow boiling. *ASME-publications-htd*, **369**, 153-170.

Kermani, E., Dessiatoun, S., Shooshtari, A. & Ohadi, M.M. (2009) Experimental investigation of heat transfer performance of a manifold microchannel heat sink for cooling of concentrated solar cells. *Electronic Components and Technology Conference, 2009. ECTC 2009. 59th* (ed by, pp. 453-459.

Keshavarz, P., Fathikalajahi, J. & Ayatollahi, S. (2008) Analysis of CO2 separation and simulation of a partially wetted hollow fiber membrane contactor. *Journal of Hazardous Materials*, **152**, 1237-1247.

Kew, P.A. & Cornwell, K. (1997) Correlations for the prediction of boiling heat transfer in small-diameter channels. *Applied Thermal Engineering*, **17**, 705-715.

Kim, N.H., Cho, J.P., Kim, J.O. & Youn, B. (2003) Condensation heat transfer of R-22 and R-410A in flat aluminum multi-channel tubes with or without micro-fins. *International Journal of Refrigeration-Revue Internationale Du Froid*, **26**, 830-839.

Kim, Y.H., Chun, W.C., Kim, J.T., Pak, B.C. & Baek, B.J. (1998) Forced air cooling by using manifold microchannel heat sinks. *KSME International Journal*, **12**, 709-718.

Kletz, T.A., Kletz, T.A., Kletz, T.A. & Chemist, G.B. (1991) *Plant design for safety: a user-friendly approach*. Hemisphere Publishing Corporation.

Kohl, A.L. & Nielsen, R. (1997) *Gas purification*. Gulf Professional Publishing.

Koşar, A., Kuo, C.-J. & Peles, Y. (2006) Suppression of boiling flow oscillations in parallel microchannels by inlet restrictors. *Journal of Heat Transfer*, **128**, 251-260.

Kumar, R., Gupta, A. & Vishvakarma, S. (2005) Condensation of R-134a vapour over single horizontal integral-fin tubes: effect of fin height. *International Journal of Refrigeration*, **28**, 428-435.

Kundu, A., Basu, J. & Das, G. (2012) A novel gas–liquid contactor for chemisorption of CO< sub>2</sub>. *Separation and Purification Technology*, **94**, 115-123.

Kuo, C.-J. & Peles, Y. (2008) Flow boiling instabilities in microchannels and means for mitigation by reentrant cavities. *Journal of Heat Transfer*, **130**, 072402.

Laddha, S. & Danckwerts, P. (1981) Reaction of $CO_2$ with ethanolamines: kinetics from gas-absorption. *Chemical Engineering Science*, **36**, 479-482.

Lee, H.J. & Lee, S.Y. (2001) Heat transfer correlation for boiling flows in small rectangular horizontal channels with low aspect ratios. *International Journal of Multiphase Flow*, **27**, 2043-2062.

Lin, S.-H., Tung, K.-L., Chen, W.-J. & Chang, H.-W. (2009) Absorption of carbon dioxide by mixed piperazine–alkanolamine absorbent in a plasma-modified polypropylene hollow fiber contactor. *Journal of Membrane Science*, **333**, 30-37.

Lu, C.T. & Pan, C. (2008) Stabilization of flow boiling in microchannel heat sinks with a diverging cross-section design. *Journal of Micromechanics and microengineering*, **18**, 075035.

Mazanec, T.J., Silva, L.J., VanderWiel, D.P. & Wang, Y. (2008) Catalysts, in microchannel apparatus, and reactions using same. In. Google Patents

Mohseni, S.G., Akhavan-Behabadi, M.A. & Saeedinia, M. (2013) Flow pattern visualization and heat transfer characteristics of R-134a during condensation inside a smooth tube with different tube inclinations. *International Journal of Heat and Mass Transfer*, **60**, 598-602.

Moore, G.E. (1965) Cramming more components onto integrated circuits. In. McGraw-Hill New York, NY, USA

Nellis, G. & Klein, S. *Heat Transfer*. Cambridge University Press.

Niu, H., Pan, L., Su, H. & Wang, S. (2009) Effects of Design and Operating Parameters on CO2 Absorption in Microchannel Contactors. *Industrial & Engineering Chemistry Research*, **48**, 8629-8634.

Ohadi, M., Choo, K., Dessiatoun, S. & Cetegen, E. (2013) *Next Generation Microchannel Heat Exchangers*. Springer.

Oxley, P., Brechtelsbauer, C., Ricard, F., Lewis, N. & Ramshaw, C. (2000) Evaluation of spinning disk reactor technology for the manufacture of pharmaceuticals. *Industrial & engineering chemistry research*, **39**, 2175-2182.

Pan, M.-Y., Qian, Z., Shao, L., Arowo, M., Chen, J.-F. & Wang, J.-X. (2014) Absorption of carbon dioxide into N-methyldiethanolamine in a high-throughput microchannel reactor. *Separation and Purification Technology*, **125**, 52-58.

Park, J.E., Vakili-Farahani, F., Consolini, L. & Thome, J.R. (2011) Experimental study on condensation heat transfer in vertical minichannels for new refrigerant R1234ze(E) versus R134a and R236fa. *Experimental Thermal and Fluid Science*, **35**, 442-454.

Poh, S. & Ng, E. (1998) Heat transfer and flow issues in manifold microchannel heat sinks: a CFD approach. *Electronics Packaging Technology Conference, 1998. Proceedings of 2nd* (ed by, pp. 246-250.

Qu, W. & Mudawar, I. (2002) Prediction and measurement of incipient boiling heat flux in micro-channel heat sinks. *International Journal of heat and mass transfer*, **45**, 3933-3945.

Qu, W. & Mudawar, I. (2003) Flow boiling heat transfer in two-phase micro-channel heat sinks—I. Experimental investigation and assessment of correlation methods. *International Journal of Heat and Mass Transfer*, **46**, 2755-2771.

Qu, Weilin, and Issam Mudawar. "Measurement and prediction of pressure drop in two-phase micro-channel heat sinks." *International Journal of Heat and Mass Transfer* 46, no. 15 (2003): 2737-2753.

Qu, W. & Mudawar, I. (2004) Transport phenomena in two-phase micro-channel heat sinks. *Journal of Electronic Packaging*, **126**, 213-224.

Ramshaw, C. (2001) Process Intensification: potential impact on the chemical industry. *Special Publications of the Royal Society of Chemistry*, **260**, 32-36.

Reay, D., Ramshaw, C. & Harvey, A. (2013) *Process Intensification: Engineering for efficiency, sustainability and flexibility*. Butterworth-Heinemann.

Rieger, K.K. (1997a) Evaporator tube. In. Google Patents

Rieger, K.K. (1997b) For use in a heat exchanger or a refrigerator evaporator. In. Google Patents

Rieger, K.K. (1999) Method of manufacturing an evaporator tube. In. Google Patents

Ryu, J., Choi, D. & Kim, S. (2003) Three-dimensional numerical optimization of a manifold microchannel heat sink. *International Journal of Heat and Mass Transfer*, **46**, 1553-1562.

Saha, A.K., Bandyopadhyay, S.S. & Biswas, A.K. (1995) Kinetics of absorption of CO< sub> 2</sub> into aqueous solutions of 2-amino-2-methyl-1-propanol. *Chemical Engineering Science*, **50**, 3587-3598.

Saitoh, Shizuo, Hirofumi Daiguji, and Eiji Hihara. "Effect of tube diameter on boiling heat transfer of R-134a in horizontal small-diameter tubes." *International Journal of Heat and Mass Transfer* 48, no. 23 (2005): 4973-4984.

Sakamatapan, K. & Wongwises, S. (2014) Pressure drop during condensation of R134a flowing inside a multiport minichannel. *International Journal of Heat and Mass Transfer*, **75**, 31-39.

Sanchez, C., Couvert, A., Laplanche, A. & Renner, C. (2007) Hydrodynamic and mass transfer in a new co-current two-phase flow gas–liquid contactor. *Chemical Engineering Journal*, **131**, 49-58.

Sartori, G. & Savage, D.W. (1983) Sterically hindered amines for carbon dioxide removal from gases. *Industrial & Engineering Chemistry Fundamentals*, **22**, 239-249.

Shah, M. (1979) A general correlation for heat transfer during film condensation inside pipes. *International Journal of Heat and Mass Transfer*, **22**, 547-556.

Shao, N., Gavriilidis, A. & Angeli, P. (2010) Mass transfer during Taylor flow in microchannels with and without chemical reaction. *Chemical Engineering Journal*, **160**, 873-881.

Sharar, D.J., Jankowski, N.R. & Morgan, B. (2010) Thermal performance of a Direct-Bond-Copper Aluminum Nitride manifold-microchannel cooler. *Semiconductor Thermal Measurement and Management Symposium, 2010. SEMI-THERM 2010. 26th Annual IEEE* (ed by, pp. 68-73.

Stankiewicz, A. & Moulijn, J.A. (2003) *Re-engineering the chemical processing plant: process intensification*. CRC Press.

Stankiewicz, A.I. & Moulijn, J.A. (2000) Process intensification: transforming chemical engineering. *Chemical Engineering Progress*, **96**, 22-34.

Steinke, M.E. & Kandlikar, S.G. (2004) An experimental investigation of flow boiling characteristics of water in parallel microchannels. *Journal of Heat Transfer*, **126**, 518-526.

Steinke M.E., Kandlikar S.G., Single-phase liquid friction factors in microchannels, Int. J. Therm. Sci. 45 (2006) 1073–1083.

Sung, M.K. & Mudawar, I. (2009) CHF determination for high-heat flux phase change cooling system incorporating both micro-channel flow and jet impingement. *International Journal of Heat and Mass Transfer*, **52**, 610-619.

Tan, J., Lu, Y., Xu, J. & Luo, G. (2012) Mass transfer characteristic in the formation stage of gas–liquid segmented flow in microchannel. *Chemical Engineering Journal*, **185**, 314-320.

Tan, J., Lu, Y.C., Xu, J.H. & Luo, G.S. (2013) Modeling investigation of mass transfer of gas-liquid concurrent flow processes. *Separation and Purification Technology*, **109**, 77-86.

Triplett, K., Ghiaasiaan, S., Abdel-Khalik, S. & Sadowski, D. (1999) Gas–liquid two-phase flow in microchannels Part I: two-phase flow patterns. *International Journal of Multiphase Flow*, **25**, 377-394.

Tortopidis, P., Bontozoglou, V., 1997. Mass transfer in gas–liquid flow in small-diameter tubes. Chemical Engineering Science 52, 2231–2237.

Tube, H.P. *http://www.highperformancetube.com/index.html*. Available at: (accessed

Tuckerman, D.B. & Pease, R. (1981) High-performance heat sinking for VLSI. *Electron Device Letters, IEEE*, **2**, 126-129.

Vandu, C.O., Liu, H., Krishna, R., 2005. Mass transfer from Taylor bubbles rising in single capillaries. Chemical Engineering Science 60, 6430–6437.

Vardan, A. & Dunn, W. (1997) Heat transfer and pressure drop characteristics of R-22, R-134a and R-407C in microchannel tubes. In. Air Conditioning and Refrigeration Center. College of Engineering. University of Illinois at Urbana-Champaign.

Versteeg, G. & Van Swaaij, W. (1988) On the kinetics between $CO_2$ and alkanolamines both in aqueous and non-aqueous solutions—I. Primary and secondary amines. *Chemical engineering science*, **43**, 573-585.

Visaria, M. & Mudawar, I. (2008) Theoretical and experimental study of the effects of spray inclination on two-phase spray cooling and critical heat flux. *International journal of heat and mass transfer*, **51**, 2398-2410.

Wang, H. & Rose, J.W. (2005) Film condensation in horizontal microchannels: effect of channel shape. *ASME 3rd International Conference on Microchannels and Minichannels* (ed by, pp. 729-735.

Wang, Y. & Ding, G.-F. (2008) Numerical analysis of heat transfer in a manifold microchannel heat sink with high efficient copper heat spreader. *Microsystem Technologies*, **14**, 389-395.

Wang, Y., Ding, G.-F. & Fu, S. (2007) Highly efficient manifold microchannel heatsink. *Electronics Letters*, **43**, 978-980.

Warrier, G.R., Dhir, V.K. & Momoda, L.A. (2002) Heat transfer and pressure drop in narrow rectangular channels. *Experimental Thermal and Fluid Science*, **26**, 53-64.

Webb, R.L. & Kim, N.-H. (1994) *Principl of enhanced heat transfer*. New York, Wiley.

Webb, R.L. & Ermis, K. (2001) Effect of hydraulic diameter on condensation of R-134A in flat, extruded aluminum tubes. *Journal of Enhanced Heat Transfer*, **8**, 77-90.

Wellsandt, S. & Vamling, L. (2003) Heat transfer and pressure drop in a plate-type evaporator. *International journal of refrigeration*, **26**, 180-188.

William Wang, W.-W., Radcliff, T.D. & Christensen, R.N. (2002) A condensation heat transfer correlation for millimeter-scale tubing with flow regime transition. *Experimental Thermal and Fluid Science*, **26**, 473-485.

Wu, H. & Cheng, P. (2003) Visualization and measurements of periodic boiling in silicon microchannels. *International Journal of Heat and Mass Transfer*, **46**, 2603-2614.

Wu, H. & Cheng, P. (2004) Boiling instability in parallel silicon microchannels at different heat flux. *International Journal of Heat and Mass Transfer*, **47**, 3631-3641.

Wu, H. & Cheng, P. (2005) Condensation flow patterns in silicon microchannels. *International Journal of Heat and Mass Transfer*, **48**, 2186-2197.

Xia, G., Liu, Q., Qi, J. & Xu, J. (2008) Influence of surfactant on friction pressure drop in a manifold microchannel. *International Journal of Thermal Sciences*, **47**, 1658-1664.

Xia, G., Chai, L., Wang, H., Zhou, M. & Cui, Z. (2011) Optimum thermal design of microchannel heat sink with triangular reentrant cavities. *Applied Thermal Engineering*, **31**, 1208-1219.

Xu, J., Gan, Y., Zhang, D. & Li, X. (2005) Microscale heat transfer enhancement using thermal boundary layer redeveloping concept. *International Journal of Heat and Mass Transfer*, **48**, 1662-1674.

Xu, J., Song, Y., Zhang, W., Zhang, H. & Gan, Y. (2008a) Numerical simulations of interrupted and conventional microchannel heat sinks. *International Journal of Heat and Mass Transfer*, **51**, 5906-5917.

Xu, J., Song, Y., Zhang, W., Zhang, H. & Gan, Y. (2008b) Numerical simulations of interrupted and conventional microchannel heat sinks. *International Journal of Heat and Mass Transfer*, **51**, 5906-5917.

Yan, S.-p., Fang, M.-X., Zhang, W.-F., Wang, S.-Y., Xu, Z.-K., Luo, Z.-Y. & Cen, K.-F. (2007) Experimental study on the separation of CO2 from flue gas using hollow fiber membrane contactors without wetting. *Fuel Processing Technology*, **88**, 501-511.

Yan, Y.-Y. & Lin, T.-F. (1999) Condensation heat transfer and pressure drop of refrigerant R-134a in a small pipe. *International Journal of Heat and Mass Transfer*, **42**, 697-708.

Yang, C.Y. & Webb, R.L. (1996a) Condensation of R-12 in small hydraulic diameter extruded aluminum tubes with and without micro-fins. *International Journal of Heat and Mass Transfer*, **39**, 791-800.

Yang, C.Y. & Webb, R.L. (1996b) Friction pressure drop of R-12 in small hydraulic diameter extruded aluminum tubes with and without micro-fins. *International Journal of Heat and Mass Transfer*, **39**, 801-809.

Ye, C., Dang, M., Yao, C., Chen, G. & Yuan, Q. (2013) Process analysis on $CO_2$ absorption by monoethanolamine solutions in microchannel reactors. *Chemical Engineering Journal*, **225**, 120-127.

Yen, T.-H., Kasagi, N. & Suzuki, Y. (2003) Forced convective boiling heat transfer in microtubes at low mass and heat fluxes. *International Journal of Multiphase Flow*, **29**, 1771-1792.

Yue, J., Chen, G., Yuan, Q., Luo, L. & Gonthier, Y. (2007) Hydrodynamics and mass transfer characteristics in gas-liquid flow through a rectangular microchannel. *Chemical Engineering Science*, **62**, 2096-2108.

Yue, J., Luo, L., Gonthier, Y., Chen, G. & Yuan, Q. (2008) An experimental investigation of gas-liquid two-phase flow in single microchannel contactors. *Chemical Engineering Science*, **63**, 4189-4202.

Yue, J., Boichot, R., Luo, L., Gonthier, Y., Chen, G. & Yuan, Q. (2010) Flow distribution and mass transfer in a parallel microchannel contactor integrated with constructal distributors. *AIChE journal*, **56**, 298-317.

Zanfir, M., Gavriilidis, A., Wille, C. & Hessel, V. (2005) Carbon dioxide absorption in a falling film microstructured reactor: Experiments and modeling. *Industrial & Engineering Chemistry Research*, **44**, 1742-1751.

Zhang, L., Wang, E.N., Goodson, K.E. & Kenny, T.W. (2005) Phase change phenomena in silicon microchannels. *International journal of heat and mass transfer*, **48**, 1572-1582.

Zhang, M. & Webb, R.L. (2001) Correlation of two-phase friction for refrigerants in small-diameter tubes. *Experimental Thermal and Fluid Science*, **25**, 131-139.

Zhang, Y., Faghri, A. & Shafii, M.B. (2001) Capillary blocking in forced convective condensation in horizontal miniature channels. *Journal of Heat Transfer*, **123**, 501-511.

Zhao, Y., Molki, M., Ohadi, M. & Dessiatoun, S. (2000) Flow Boiling of $CO_2$ in Microchannels. *Transactions-american society of heating refrigerating and air conditioning engineers*, **106**, 437-445.

Zohler, S.R. (1993) Method of manufacture an enhanced heat transfer surface and apparatus for carrying out the method. In. Google Patents